AD/A-004 767

PARTICLE CONCENTRATIONS IN HIGH MACH NUMBER, TWO-PHASE FLOWS

K. D. Korkan, et al

Ohio State University

Prepared for:

Aerospace Research Laboratories

July 1974

UNCLASSIFIED

REPORT DOCUMENTATION PAGE — BEFORE COMPLETING FORM

1. REPORT NUMBER: ARL 74-0102	2. GOVT ACCESSION NO.
3. RECIPIENT'S CATALOG NUMBER: AD/A-004 767	
4. TITLE (and Subtitle): PARTICLE CONCENTRATIONS IN HIGH MACH NUMBER TWO-PHASE FLOWS	5. TYPE OF REPORT & PERIOD COVERED: Final, 1 Jan 1973 - 1 Jan 1974
	6. PERFORMING ORG. REPORT NUMBER: 3606-F
7. AUTHOR(s): K. D. Korkan, S. L. Petrie and R. J. Bodonyi	8. CONTRACT OR GRANT NUMBER(s): F33615-73-C-4012
9. PERFORMING ORGANIZATION NAME AND ADDRESS: The Aeronautical & Astronautical Research Laboratory, The Ohio State University, 3300 Case Road, Columbus, Ohio 43210	10. PROGRAM ELEMENT, PROJECT, TASK AREA & WORK UNIT NUMBERS: Project 7065
11. CONTROLLING OFFICE NAME AND ADDRESS: Aerospace Research Laboratories (LF), Wright-Patterson Air Force Base, Ohio 45433	12. REPORT DATE: July 1974
	13. NUMBER OF PAGES: 127
14. MONITORING AGENCY NAME & ADDRESS(if different from Controlling Office)	15. SECURITY CLASS. (of this report): Unclassified
	15a. DECLASSIFICATION/DOWNGRADING SCHEDULE

16. DISTRIBUTION STATEMENT (of this Report)

Approved for public release; distribution unlimited.

17. DISTRIBUTION STATEMENT (of the abstract entered in Block 20, if different from Report)

18. SUPPLEMENTARY NOTES

19. KEY WORDS (Continue on reverse side if necessary and identify by block number)

Sphere drag coefficient	Hypersonic
Two-phase flow	Oblique shock
Particle concentration	Prandtl-Meyer expansion
Laser scattering	Wedge
Test facility	

20. ABSTRACT (Continue on reverse side if necessary and identify by block number)

An experimental and theoretical study of the behavior of solid particles in high speed flow systems has been conducted. A new drag coefficient correlation which allows greater accuracy in the prediction of particle trajectories over a wide range of slip Mach number and slip Reynolds number was formulated. A variety of basic two-phase flow situations, i.e., uniform flow, Prandtl-Meyer expansion, and oblique shock, was investigated by varying the initial particle

DD FORM 1 JAN 73 1473

velocity and particle radius. In addition, the effect of different gases and different particles on the two-phase flow characteristics was investigated, and significant differences were noted. The exploratory experimental studies conducted in this investigation substantiate that a test facility suitable for the study of particle trajectories has been developed and that accurate particle concentration profiles can be obtained with the laser scattering technique.

PREFACE

This technical report, submitted in January 1974, covers work performed under Contract No. F33615-73-C-4012, for the Department of the Air Force, Air Force Systems Command, Aerospace Research Laboratories, Wright-Patterson Air Force Base, Ohio. The work was performed by the Aeronautical and Astronautical Research Laboratory of The Ohio State University in Columbus, Ohio. Work described herein covers the period from 1 January 1973 to 1 January 1974. The program was under the direction of Mr. Elmer G. Johnson of the Fluid Dynamics Facilities Research Laboratory, ARL/LF.

TABLE OF CONTENTS

SECTION		PAGE
List of Symbols		xi
I	INTRODUCTION	1
II	TWO-PHASE FLOW THEORETICAL ANALYSIS	3
	A. TWO-PHASE FLOW CONSERVATION EQUATIONS/ COMPUTER PROGRAM	3
	1. Theoretical Two-Phase Flow Assumptions	3
	B. SPHERE DRAG COEFFICIENT CORRELATIONS	8
	C. INFLUENCE OF SPHERE DRAG COEFFICIENT CORRELATION ON TWO-PHASE FLOW CHARACTERISTICS	13
	1. Uniform Flow	13
	2. Prandtl-Meyer Expansion Fan	20
	3. Two-Dimensional Wedge/Oblique Shock	33
	D. COMPOSITE SOLUTION TO DESCRIBE THE PARTICLE FLOW ABOUT A TWO-DIMENSIONAL WEDGE	33
	E. EFFECT OF DIFFERENT GASES ON TWO-PHASE FLOW CHARACTERISTICS	42
	F. EFFECT OF DIFFERENT PARTICLES IN TWO-PHASE FLOW CHARACTERISTICS	47
III	TWO-PHASE FLOW EXPERIMENTAL STUDIES	55
	A. TEST FACILITIES	55
	B. MODELS	60
	C. INSTRUMENTATION	60
	D. RESULTS AND DISCUSSION	62
	1. Basic Particle Concentration Profile	62
	2. Particle Concentration Profiles Behind Wedges	62
IV	SUMMARY AND CONCLUSIONS	75

CONTENTS (continued)

SECTION	PAGE
REFERENCES	76
APPENDIX A - UNIFORM FLOW	79
APPENDIX B - PRANDTL-MEYER EXPANSION FAN	95
APPENDIX C - TWO-DIMENSIONAL WEDGE/OBLIQUE SHOCK	105
LIST OF SYMBOLS	116

LIST OF ILLUSTRATIONS

FI		PAGE
1	Two-Phase Flow Computer Program - Block Diagram . . .	6
2	Comparison of Existing Sphere Drag Correlations with Experimental Data	9
3	Comparison of Existing Sphere Drag Correlations with Experimental Data	12
4	The Comparison of Temperature Dependent Sphere Drag Data with the Present Correlation (M_∞ = 2.0)	15
5	The Comparison of Temperature Dependent Sphere Drag Data with the Present Correlation (M_∞ = 4.0)	16
6	The Comparison of Temperature Dependent Sphere Drag Data with the Present Correlation (M_∞ = 6.0)	17
7	The Comparison of Temperature Dependent Sphere Drag Data with the Present Correlation (M_∞ = 10.4)	18
8	Trajectory of Particle in Air for Uniform Flow Case for Different Drag Coefficient Correlations (r_p = 0.5 μm, u_{p_i} = 100 ft/s)	19
9	Particle Velocity History in Air for Uniform Flow Case for Different Drag Coefficient Correlations (r_p = 0.5 μm, u_{p_i} = 100 ft/s)	21
10	Particle Temperature History in Air for Uniform Flow Case for Different Drag Coefficient Correlations (r_p = 0.5 μm, u_{p_i} = 100 ft/s)	22
11	Trajectory of Particle in Air for Uniform Flow Case for Different Drag Coefficient Correlations (r_p = 0.5 μm, u_{p_i} = 2000 ft/s)	23
12	Particle Velocity History in Air for Uniform Flow Case for Different Drag Coefficient Correlations (r_p = 0.5 μm, u_{p_i} = 2000 ft/s)	24
13	Particle Temperature History in Air for Uniform Flow Case for Different Drag Coefficient Correlations (r_p = 0.5 μm, u_{p_i} = 2000 ft/s)	25

FIGURE		PAGE
14	Trajectory of Particle in Air for Uniform Flow Case for Different Drag Coefficient Correlations (r_p = 50 μm, u_{p_i} = 100 ft/s)	26
15	Particle Velocity History in Air for Uniform Flow Case for Different Drag Coefficient Correlations (r_p = 50 μm, u_{p_i} = 100 ft/s)	27
16	Particle Temperature History in Air for Uniform Flow Case for Different Drag Coefficient Correlations (r_p = 0.5 μm, u_{p_i} = 100 ft/s)	28
17	Trajectory of Particle Passing Through Prandtl-Meyer Expansion Fan in Air for Different Drag Coefficient Correlations (r_p = 0.5 μm, u_{p_i} = 100 ft/s)	29
18	Particle Velocity History Through Prandtl-Meyer Expansion Fan in Air for Different Drag Coefficient Correlations (r_p = 0.5 μm, u_{p_i} = 100 ft/s)	30
19	Particle Temperature History Through Prandtl-Meyer Expansion Fan in Air for Different Drag Coefficient Correlations (r_p = 0.5 μm, u_{p_i} = 100 ft/s)	31
20	Trajectory of Particle Passing Through Prandtl-Meyer Expansion Fan in Air for Different Drag Coefficient Correlations (r_p = 0.5 μm, u_{p_i} = 2000 ft/s)	32
21	Particle Velocity History Through Prandtl-Meyer Expansion Fan in Air for Different Drag Coefficient Correlations (r_p = 0.5 μm, u_{p_i} = 2000 ft/s)	34
22	Particle Temperature History Through Prandtl-Meyer Expansion Fan in Air for Different Drag Coefficient Correlations (r_p = 0.5 μm, u_{p_i} = 2000 ft/s)	35
23	Trajectory of Particle Passing Through Prandtl-Meyer Expansion Fan in Air for Different Drag Coefficient Correlations (r_p = 50 μm, u_{p_i} = 100 ft/s)	36
24	Particle Velocity History Through Prandtl-Meyer Expansion Fan in Air for Different Drag Coefficient Correlations (r_p = 50 μm, u_{p_i} = 100 ft/s)	37

FIGURE		PAGE
25	Particle Temperature History Through Prandtl-Meyer Expansion Fan in Air for Different Drag Coefficient Correlations (r_p = 50 μm, u_{p_i} = 100 ft/s)	38
26	Trajectory of Particle Passing Through an Oblique Shock in Air for Different Drag Coefficient Correlations (r_p = 5 μm, u_{p_i} = 100 ft/s)	39
27	Particle Velocity History Through an Oblique Shock in Air f r Different Drag Coefficient Correlations (r_p = 5 μm, u_{p_i} = 100 ft/s)	40
28	Particle Temperature History Through an Oblique Shock in Air for Different Drag Coefficient Correlations (r_p = 5 μm, u_{p_i} = 100 ft/s)	41
29	Two-Phase Flow Field and Associated Particle Trajectories About a 10° Half-Angle Wedge	43
30	Particle Velocity History on Particle Trajectories (1) and (4) in Two-Phase Flow Field About a 10° Half-Angle Wedge	44
31	Particle Temperature History on Particle Trajectories (1) and (4) in Two-Phase Flow Field About a 10° Half-Angle Wedge	45
32	Mass Flux Density Profiles at Three Axial Locations in Two-Phase Flow Field About a 10° Half-Angle Wedge .	46
33	Trajectory of Particle in Different Gases for Uniform Flow Case (r_p = 5 μm, u_{p_i} = 100 ft/s)	48
34	Particle Velocity History in Different Gases for Uniform Flow Case (r_p = 5 μm, u_{p_i} = 100 ft/s)	49
35	Particle Temperature History in Different Gases for Uniform Flow Case (r_p = 5 μm, u_{p_i} = 100 ft/s)	50
36	Trajectory of Particle in Air for Uniform Flow Case for Different Particles (r_p = 5 μm, u_{p_i} = 100 ft/s) .	51
37	Particle Velocity History in Air for Uniform Flow Case for Different Particles (r_p = 5 μm, u_{p_i} = 100 ft/s)	52

FIGURE		PAGE
38	Particle Temperature History in Air for Uniform Flow Case for Different Particles (r_p = 5 μm, u_{p_i} = 100 ft/s)	53
39	Particle Concentration by Wave Systems - Facility Schematic	56
40	Measured Pitot Pressure Profile for Two-Phase Flow Tunnel (No Particles)	57
41	Schematic of Particle Feed System	58
42	Particle Size Histogram of Titanium Dioxide Used in Experimental Study	59
43	Laser Scattering Instrumentation Schematic	61
44	Intensity as a Function of Time at a Fixed Profile Location	63
45	Relationship Between Valve Openings and Dust Introduced into Tunnel	64
46	Nondimensional Intensity Profile as Function of Distance from ℄ of Tunnel	65
47	Profile of Titanium Dioxide Particles Due to Scattered Light - No Model Inserted	66
48	Profile of Titanium Dioxide Particles Due to Scattered Light - No Model Inserted	67
49	Profile of Titanium Dioxide Particles Due to Scattered Light - No Model Inserted	68
50	Profile of Titanium Dioxide Particles Due to Scattered Light - 5° Total Angle Wedge at 0° Angle of Attack	69
51	Profile of Titanium Dioxide Particles Due to Scattered Light - 5° Total Angle Wedge at 0° Angle of Attack	70
52	Profile of Titanium Dioxide Particles Due to Scattered Light - 5° Total Angle Wedge at 2.5° Angle of Attack	71

FIGURE		PAGE
53	Profile of Titanium Dioxide Particles Due to Scattered Light - 5° Total Angle Wedge at 7.5° Angle of Attack	72
54	Profile of Titanium Dioxide Particles Due to Scattered Light - 15° Total Angle Wedge at 0° Angle of Attack	73
55	Profile of Titanium Dioxide Particles Due to Scattered Light - 15° Total Angle Wedge at 10° Angle of Attack	74

SECTION I

INTRODUCTION

Conventional techniques of simulating hypervelocity flight environments in ground-based facilities are severely limited by their ability to produce simultaneously the total enthalpy and total pressure required for adequate simulation. The testing mediums generally are not representative of true atmospheric conditions because of contamination caused by the heating process and incomplete chemical recombination of the test gas during the acceleration process. The multicomponent flow device described by Johnson and von Ohain[1] has the objective of producing air flows which simulate hypervelocity flight without passing the working gas through phases of high static temperature. In this device, a multicomponent flow process is employed in which kinetic energy is transferred from a low molecular weight working gas to a much higher molecular weight gas, such as air. In both the direct and indirect energy exchange processes,[1] either liquid air or refractory particles are accelerated by the low molecular weight gas in a multistage process.

In addition to the RHEA device of Ref. 1, there is a critical requirement for development of a combined erosion-ablation test facility to simulate certain phases of high speed vehicle flight. In this facility, solid particles are injected into a high enthalpy flow; however, the injection must be accomplished in the supersonic portions of the flow to avoid vaporization of the particles before they reach the test section. Accompanying the injection of particles is a complicated interaction between the main high enthalpy flow and the flow containing the particles.

There is a paucity of data regarding focusing of solid and/or liquid particles in a two-phase flow. The majority of investigations on two-phase flows has been directed toward the determination of the effect of the particles on the overall flow properties and the determination of particle trajectories in conventional nozzle geometries.[2-8] While the motivations for these studies are much different from those of this study, the techniques of analysis have direct application. The theoretical methods can be used to characterize the flow properties, and the experimental results provide guidelines for the choice of particle sizes which lead to optimum velocity slip. When wave systems are used for focusing, the inertial properties of the particles and the associated velocity and thermal slip between them and the carrier gas are extremely important in determining the final particle trajectories. While certain theoretical analyses of gaseous focusing systems are available,[9,10] detailed experimental studies of focusing in two-phase flows are required before successful operation of the multicomponent flow device can be achieved.

A critical problem in the multicomponent flow device is the separation of the accelerated particles from the low molecular weight carrier gas. In the direct process, the particles must be focused into a region suitable for their vaporization by energy addition. In the indirect process, the focusing must be accomplished in a manner which leads to an efficient transfer of momentum and energy to the tunnel working gas (air). Detailed examinations of the wave pattern and flow field geometries which result in such focusing is the subject of this study.

Theoretical and experimental studies have been conducted to examine particle trajectories in various flow field geometries. Detailed analyses of shear drag coefficients at high Mach number and low Reynolds number were conducted, and a new correlation for shear drag coefficient which improves the accuracy of trajectory calculations in high speed flows was developed. Exploratory experimental studies were conducted to examine particle trajectories in basic flow field geometries.

SECTION II

TWO-PHASE FLOW THEORETICAL ANALYSIS

A. TWO-PHASE FLOW CONSERVATION EQUATIONS/COMPUTER PROGRAM

A digital computer program has been developed to analyze the steady flow of a gas-particle mixture in which the gas affects the particles, but the particles do not interact with the gas. Energy exchange is assumed to occur between the gas and the particles by forced convection and between the particles and space by radiation. Drag forces are the only external forces assumed to act on the particles. These important assumptions, in addition to others adopted, are listed below.

1. Theoretical Two-Phase Flow Assumptions

   a. In an uncoupled steady-flow of a gas-particle mixture the gas affects the particles, but the particles do not interact with the gas.
   b. No mass or energy is lost from the system.
   c. No mass is exchanged between the phases.
   d. Volume occupied by the particles is negligible.
   e. Thermal (Brownian) motion of particles is negligible.
   f. Particles do not interact.
   g. Gas environment is inviscid except for the drag it exerts on the particles.
   h. Composition and specific heats of both gas and particles are constant.
   i. Energy exchange occurs between the gas and particle by forced convection, and between the particle and space by radiation.
   j. Drag forces are the only external forces acting on the particles.

Utilizing the above assumptions the conservation equations can be written[1] describing the flow of the gas-particle system by treating the gas velocity, gas temperature, particle velocity, and particle temperature as dependent variables and distance as the independent variable. These equations have been formulated in a coordinate system with axes parallel and perpendicular to the local particle direction. The particle momentum equations take the form:

$$\frac{du_p}{dq} = \frac{3}{8}\left[\frac{\rho_g f_p}{\rho_p r_p}\right]\left[\frac{u_{rel}}{u_p}\right] \cos(\cdot\cdot) \qquad (1.)$$

$$\frac{d\alpha}{dq} = \frac{9}{2}\left[\frac{\mu_g f_p}{\rho_p r_p^2}\right]\left[\frac{u_{rel}}{u_p}\right]\left[\frac{\sin(\beta-\alpha)}{\cos(\beta-\alpha)}\right] \qquad (2)$$

In the above equations, the factor (f_p) accounts for deviations of the drag coefficient from the ideal Stokes flow value (24/Re).

Similarly, the particle energy equation is given by

$$\frac{dT_p}{dq} = \frac{3}{r_p \rho_p C u_p \cos(\beta-\alpha)}\left[\frac{C_{pg} f_g (T_g - T_p)}{r_p} + \epsilon\sigma(T_p^4 - T_g^4)\right] \qquad (3)$$

Included in the above equation is a correction term f_g, similar to f_p, to account for deviations from Stokes flow, thereby including rarefaction, compressibility, and inertial effects.[17] The continuity equation and equation of state for a perfect gas complete the set of equations.

For the purposes of this study it has been assumed that the gaseous flow field can be adequately described by an inviscid two-dimensional flow in which both Prandtl-Meyer expansion waves and oblique shock waves can be embedded. Also, the particles are assumed to be spherical and are defined by specifying their molecular weight, radius, and specific heat. There are averaging techniques available at AARL that are not documentated in this report which allow mixtures of particles with different characteristics to be treated.

The viscosity term which appears in Eq (1)-(3) can be computed from the results of Bartz,[18] which is accurate for most mixtures consisting principally of diatomic gases. However, for greater accuracy the viscosity can be obtained from the results of an analysis similar to that of Adler and Anderson,[19] which is valid for a dilute gas mixture with a frozen chemical composition.

As stated in the initial assumptions, the only force acting to accelerate the particles is the drag. The drag term in Eqs (1) and (2) has been represented by a ratio of the actual sphere drag coefficient to that in Stokes' flow. It may be noted that Stokes's flow regime is valid for incompressible flows at Reynolds numbers less than 0.1. Since it is possible for the particle to experience free-molecule, slip, and continuum flow conditions, it is necessary to include a drag coefficient valid over the entire range of flow conditions. To this end, the results of several drag coefficient correlations have been used in this study to give empirical fits of f_p as a function of Mach and Reynolds numbers. These are discussed in detail in the next section of this report.

A computer program to numerically solve Eqs (1)-(3) has been written using a fourth-order Runge-Kutta numerical integration scheme

with a variable step size. A block diagram of the method of solution is given in Figure 1. Calculations begin at a specified axial location, $Z = Z_{min}$, with specified initial conditions for the gaseous flow field, i.e., Mach number, flow angle, ratio of specific heats, total pressure, and temperature. The initial particle velocity, flow direction, temperature, and concentration are specified as functions of the radial coordinate r. For $Z > Z_{min}$, selected particle trajectories are computed with flow properties determined from either isentropic expansion or oblique shock relationships. Particle velocity, gas velocity, particle and gas flow directions, particle and gas temperatures, relative Mach number, relative Reynolds number, Knudsen number, relative dynamic pressure, and drag coefficient are given at specified axial intervals and corresponding radial locations.

In the calculation of the particle concentration profiles the continuity equation for the particle is applied along the previously computed particle trajectories, which, in effect, are particle streamlines. That is, the continuity equation for the particles can be written as

$$(\rho udA)_{initial} = (\rho udA)_Z \tag{4}$$

where

$$\rho uA = \begin{pmatrix}\text{mass density}\\ \text{of particles}\end{pmatrix}\begin{pmatrix}\text{particle}\\ \text{velocity}\end{pmatrix}(\text{area})$$

Now

$$\rho = \begin{pmatrix}\text{volume of}\\ \text{particle}\end{pmatrix}\begin{pmatrix}\text{particle}\\ \text{density}\end{pmatrix}\begin{pmatrix}\text{number of particles}\\ \text{per unit volume}\end{pmatrix}$$

i.e.,

$$\rho = \left(\frac{4}{3}\pi r_p^3\right)(\rho_p)(N_p) \tag{5}$$

To find an equivalent form for the udA term, consider two particle streamlines, i and j. Therefore

$$\Delta r = r_j - r_i$$

and

$$dA = (r_j - r_i) \cdot 1 \tag{6}$$

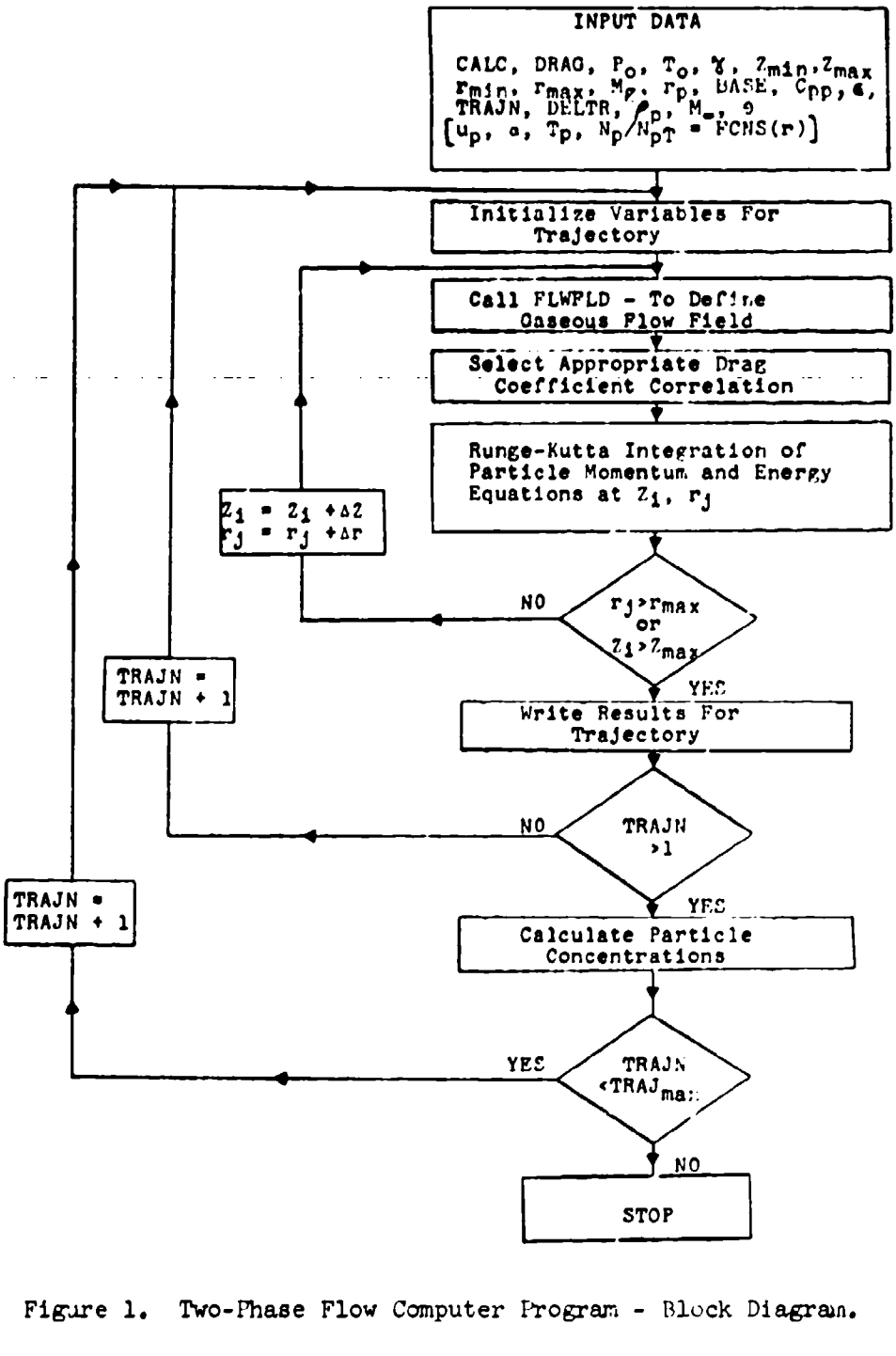

Figure 1. Two-Phase Flow Computer Program - Block Diagram.

The velocity term, averaged, becomes

$$u = \left(\frac{u_{p_i} + u_{p_j}}{2} \right) \tag{7}$$

The plane normal to the average velocity vector can be expressed as

$$\cos \left[\frac{\alpha_i + \alpha_j}{2} \right]^{-1} \left[r_j - r_i \right] \tag{8}$$

and the term udA becomes

$$\left(r_j - r_i \right) \left[\cos \left\{ \frac{\alpha_i + \alpha_j}{2} \right\}^{-1} \right] \left[\frac{u_{p_i} + u_{p_j}}{2} \right] \tag{9}$$

Therefore the term ρudA becomes

$$\rho udA = \frac{4}{3} \pi r_p^3 \rho_p N_p \pi \left(r_j - r_i \right) \left[\cos \left\{ \frac{\alpha_i + \alpha_j}{2} \right\}^{-1} \right] \left[\frac{u_{p_i} + u_{p_j}}{2} \right] \tag{10}$$

Placing this expression into Eq (4) and simplifying result in

$$\left\{ \left(\frac{N_p}{N_{p_T}} \right) \left(r_j - r_i \right) \left\{ \cos \left[\frac{\alpha_i + \alpha_j}{2} \right] \right\}^{-1} \left[\frac{u_{p_i} + u_{p_j}}{2} \right] \right\}_{\text{initial}} =$$

$$\left\{ \left(\frac{N_p}{N_{p_T}} \right) \left(r_j - r_i \right) \left\{ \cos \left[\frac{\alpha_i + \alpha_j}{2} \right]^{-1} \left[\frac{u_{p_i} + u_{p_j}}{2} \right] \right\} \right\}_z \tag{11}$$

Note that

$$\frac{N_p}{N_{p_T}} = \frac{\left(\frac{N_p}{N_{p_T}} \right)_i + \left(\frac{N_p}{N_{p_T}} \right)_j}{2} \tag{12}$$

The continuity equation is then satisfied at each specified axial location. The necessary information is available at this location in the gaseous flow field to obtain the local particle concentration value.

B. SPHERE DRAG COEFFICIENT CORRELATIONS

An important ingredient in the two-phase flow theoretical analyses is the correlation employed to obtain the drag coefficient of the solid particles. Various drag coefficient correlations were examined and were compared with the results of experimental sphere drag coefficient measurements obtained in a ballistic range.[15] These data provide sphere drag coefficients over a range of Mach numbers from approximately 0.1 to 7.0 with sphere Reynolds numbers ranging from 5×10^{0} to 8×10^{4}. This set of data includes over 500 data points taken in the same facility by the same investigators. These data are for $T_w/T_o = 1$ and therefore comparisons of sphere drag coefficients can be made without considering wall temperature effects.

The sphere drag coefficient correlation of Carlson and Hoglund[12]

$$C_D = \frac{24}{Re}\left[\frac{(1 + 0.15\ Re^{0.687})(1 + \exp[(0.427/M^{4.63}) - (3.0/Re^{0.88})])}{(1 + (M/Re)(3.82 + 1.28\ \exp[-1.25\ Re/M])}\right] \tag{13}$$

and that of Crowe[16]

$$C_D = \left(C_{D_{inc}}{}^{-2}\right)\exp[-3.07(\gamma)^{1/2}(M/Re)g(Re)] + \frac{h(M)}{(\gamma)^{1/2}M}\exp[-Re/2M] + 2$$

where

$$\log_{10}g(Re) = 1.25[1 + \tanh(0.77\ \log_{10}Re - 1.92)] \tag{14}$$

and

$$h(M) = \left[2.3 + 1.7\left(\frac{T_p}{T_g}\right)^{1/2}\right] - 2.3\ \tanh(1.17\ \log_{10}M)$$

were first examined. Comparisons of the drag coefficients of Carlson and Hoglund and Crowe are shown in terms of percent deviation from experimental data[15] in Figure 2. Percent deviation is defined as

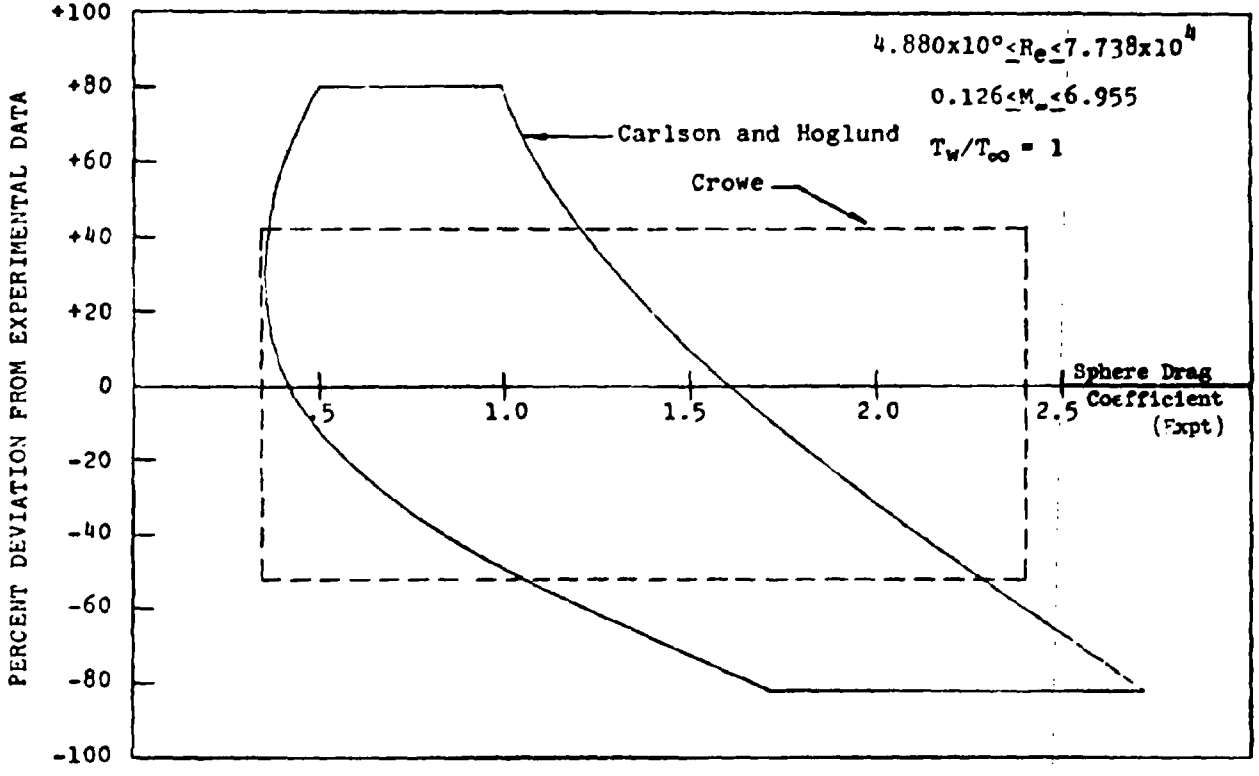

Figure 2. Comparison of Existing Sphere Drag Correlations with Experimental Data.

$$\% \text{ Deviation} = \left[\frac{C_{D_{exp}} - C_{D_{theor}}}{C_{D_{exp}}}\right] \times 100 \qquad (15)$$

As can be seen, the differences between the theoretical and experimental sphere drag coefficients of Carlson and Hoglund are extensive, ranging to ± 80%, while for the correlation of Crowe the deviations range from +40% to -50%. It is interesting to note that the Carlson and Hoglund predictions are consistently high for experimental sphere drag coefficients greater than approximately 1.6. Conversely, Crowe predicts both high and low theoretical sphere drag coefficients over the entire range of experimental sphere drag coefficients. A significant difference not apparent in this comparison is that the drag coefficient correlation of Crowe allows for various particle to gas temperature ratios while that of Carlson and Hoglund includes no wall temperature effects.

Another sphere drag coefficient correlation that was examined is that of Cuddihy, Beckwith, and Schroeder.[17]

For $M \leq 0.5$

$$C_D = \frac{C_{D_o} + \frac{51.1M}{Re_s}}{1 + 0.256M\left(C_{D_o} + \frac{51.1M}{Re_s}\right)}$$

where

$$C_{D_o} = \frac{24}{Re_s} + 0.4 + 1.6\exp\left[-0.028\ Re_s^{0.82}\right]$$

For $M > 0.5$

$$C_D = C_{D,C} + \left(C_{D,FM} - C_{D,C}\right)\exp\left[-ARe_s^{n}\right] \qquad (16)$$

where

$$\left.\begin{array}{rcl} 0.520 \leq & C_{D,C} & \leq 0.981 \\ 2.00 \leq & C_{D,FM} & \leq 7.80 \\ 0.0447 \leq & A & \leq 0.315 \\ 0.410 \leq & n & \leq 0.745 \end{array}\right\} \text{ (Table Inputs as FNS of Mach No.)}$$

This correlation[17] compares favorably with the ballistic range data of Bailey and Hyatt,[15] as shown in Figure 3, with maximum deviations ranging from approximately +30% to -40%. It does not, however, include the influences of unequal particle and gas temperatures.

A new sphere drag correlation formula has been developed from the ballistic range data by modifying the correlation of Cuddihy, Beckwith, and Schroeder to include varying particle and gas temperatures.

For $M \leq 0.5$

$$C_D = \frac{C_{D_o} + \frac{51.1M}{Re_s}}{1 + 0.256M\left(C_{D_o} + \frac{51.1M}{Re_s}\right)}$$

where

$$C_{D_o} = \frac{24}{Re_s} + 0.44 + 1.6\exp\left[-0.028\ Re_s^{0.82}\right]$$

For $M > 0.5$

$$C_D = h_1(M)\left[1 + \exp\left(-ARe_s^{n}\right)\right] - h_2(M)\exp\left(-ARe_s^{n}\right) + \Delta C_D(T) \qquad (17)$$

where

$$\left.\begin{aligned} 0.455 &\leq h_1(M) \leq 1.045 \\ 2.020 &\leq h_2(M) \leq 7.800 \\ 0.045 &\leq A \leq 0.315 \\ 0.410 &\leq n \leq 0.740 \end{aligned}\right\} \text{ (Table Inputs as FNS of Mach No.)}$$

$$\Delta C_D(T) = \frac{\frac{T_w}{T_\infty} - 1}{\gamma M}\left\{0.142 + \left[2.220 - 0.597\left(\frac{T_w}{T_\infty}\right)^{1}\right]\exp\left[-Re_2/M\right]\right\} \quad (M \geq 1)$$

Comparisons of Eq (16) and (17) show that for $M \leq 0.5$ the correlation is identical to that of Cuddihy, Beckwith and Schroeder. However, for $M \geq 0.5$ the rearrangement of the C_D expression and the changes to the

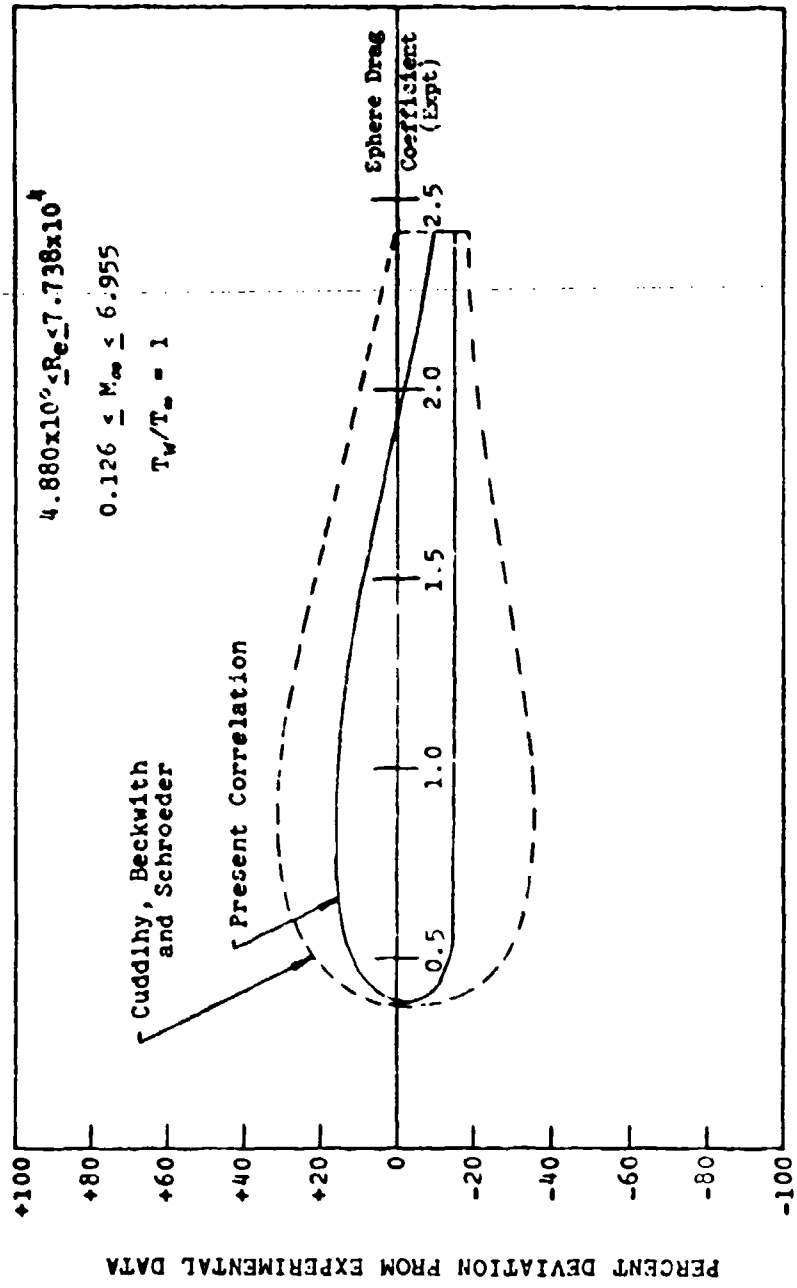

Figure 3. Comparison of Existing Sphere Drag Correlations with Experimental Data.

table inputs of $h_1(M)$ and $h_2(M)$ result in a more accurate fit of the experimental data (see Table I for new table inputs). A comparison of the percent deviation of the results of this present correlation with the ballistic range data is shown in Figure 3. It can be seen that the present correlation greatly improves the accuracy of the sphere drag coefficients, resulting in deviations of +15% to -20% over an extremely wide range of slip Mach number and slip Reynolds number. These comparisons have been made for $T_w/T_\infty = 1$. As shown in the present correlation [Eq (17)], a $\Delta C_D(T)$ term has been added to include the effects of variable wall temperatures. The results of Bailey and Hiatt[15] have again been used to verify the accuracy of the $\Delta C_D(T)$ term, as shown in Figures 4 through 7. It may be noted that the correlation is based on the freestream slip Mach number (M) and a slip Reynolds number behind a normal shock (Re_2). The following cases have been used for means of comparison:

M = 2.0	Re_2 = 6,10,20,50,100	(Figure 4)
M = 4.0	Re_2 = 2,7,10,20,50,200,700	(Figure 5)
M = 6.0	Re_2 = 7,10,20,50,200,1000	(Figure 6)
M = 10.4	Re_2 = 2,5,10,20,50,500,5000	(Figure 7)

As shown in Figures 4 through 7, the $\Delta C_D(T)$ term prediction is acceptable for a range of Mach numbers from 2 to 10.4 and Reynolds numbers from 2 to 5000. At the present time, the $\Delta C_D(T)$ term is restricted to $M > 1$ since no comparisons have been made for the subsonic slip Mach numbers.

C. INFLUENCE OF SPHERE DRAG COEFFICIENT CORRELATION ON TWO-PHASE FLOW CHARACTERISTICS

The influence of the sphere drag coefficient correlations on particle trajectories, velocities, and temperatures in simple flow situations was investigated. The flow situations consisted of uniform flow, where the particles are injected at an angle from the horizontal with a specific initial velocity, a simple Prandtl-Meyer expansion fan, and an oblique shock wave. The cases investigated were for particle radii of 0.5, 5, 25, and 50 μm and for particle velocities of 100, 1000, and 2000 ft/s. In this segment of the study, titanium dioxide (TiO_2) particles were used and the fluid was taken as air (molecular weight = 29).

1. Uniform Flow

The trajectories for a 1.0 μm diameter particle injected at an initial velocity of 100 ft/s into a Mach 5 air flow at an angle of 45° are shown in Figure 8. Note that there are large differences in the particle trajectories, depending on the specific drag coefficient correlation employed. Hence, accurate particle drag coefficients are required to obtain reliable particle trajectories. Corresponding

TABLE I

TABLE INPUTS AS FUNCTIONS OF MACH NUMBER
FOR PRESENT SPHERE DRAG CORRELATION

Mach No.	$h_1(M)$	$h_2(M)$	A	n
0.5	0.480	7.800	0.315	0.410
0.6	0.455	6.500	0.240	0.468
0.7	0.497	5.570	0.182	0.500
0.8	0.535	4.920	0.141	0.545
0.9	0.610	4.450	0.110	0.590
1.0	0.820	4.100	0.090	0.620
1.1	0.900	3.850	0.070	0.645
1.2	0.990	3.600	0.065	0.670
1.3	0.993	3.420	0.060	0.680
1.4	0.995	3.230	0.055	0.690
1.5	0.999	3.110	0.052	0.700
1.6	1.000	2.980	0.049	0.710
1.7	1.020	2.890	0.048	0.713
1.8	1.005	2.800	0.047	0.715
1.9	0.990	2.740	0.047	0.718
2.0	1.045	2.680	0.046	0.720
2.2	1.035	2.580	0.046	0.723
2.4	1.040	2.480	0.046	0.725
2.6	1.035	2.420	0.046	0.725
2.8	1.035	2.360	0.046	0.725
3.0	1.035	2.320	0.045	0.727
3.2	1.030	2.280	0.045	0.730
4.0	1.025	2.170	0.045	0.730
5.0	1.030	2.100	0.045	0.735
6.0	1.040	2.050	0.045	0.735
8.0	1.030	2.020	0.045	0.740

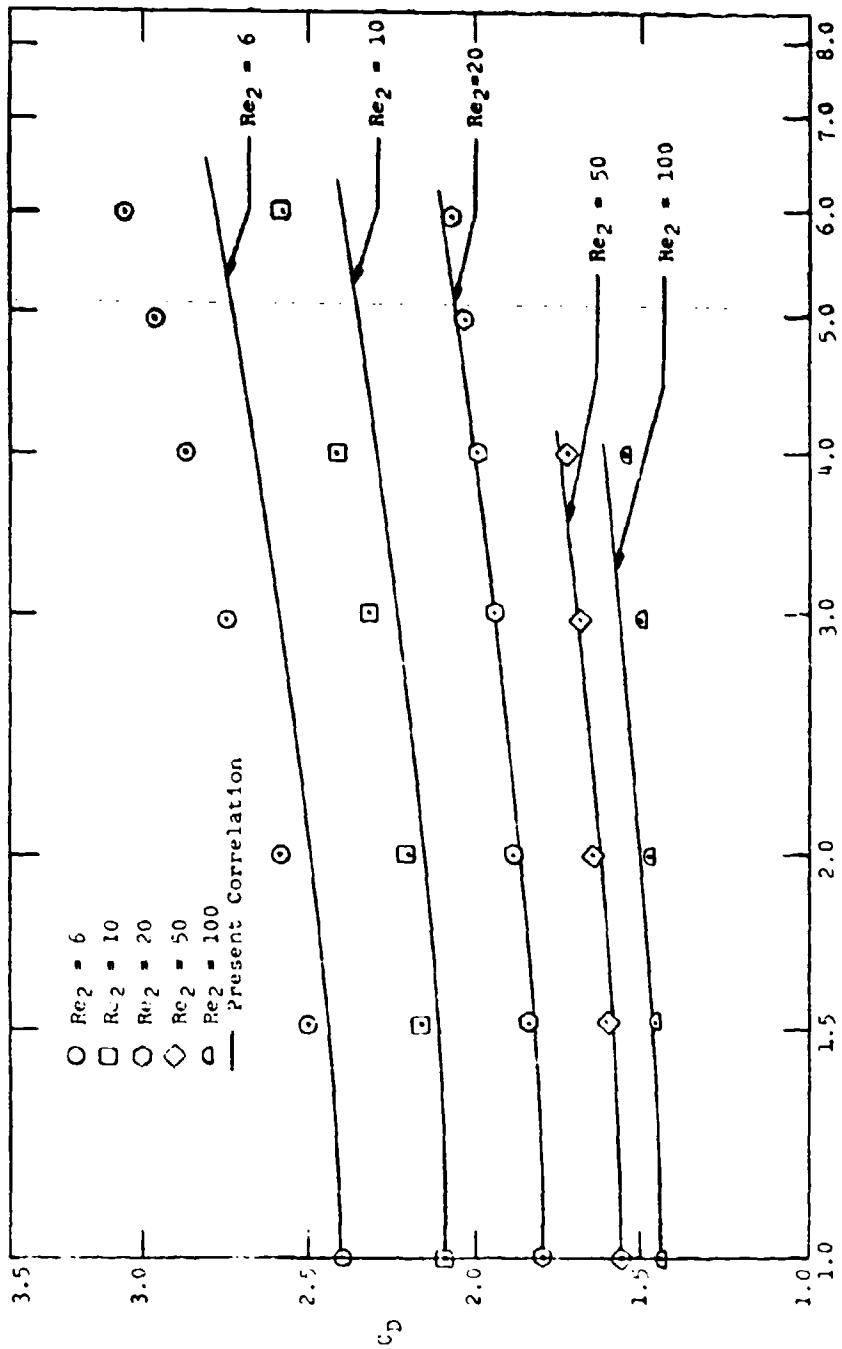

Figure 4. The Comparison of Temperature Dependent Sphere Drag Data with the Present Correlation ($M_\infty = 2.0$).

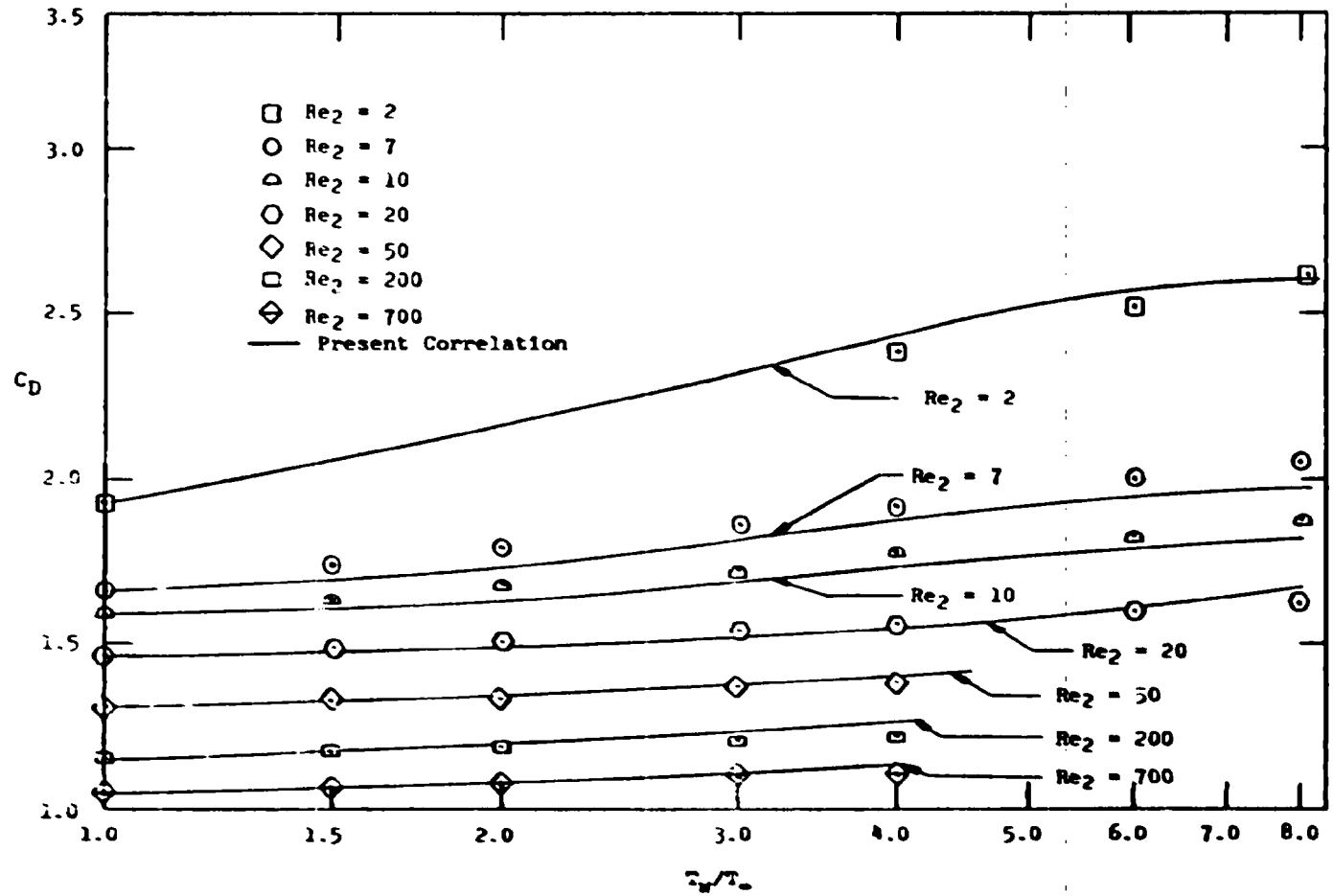

Figure 5. The Comparison of Temperature Dependent Sphere Drag Data with the Present Correlation (M_∞ = 4.0).

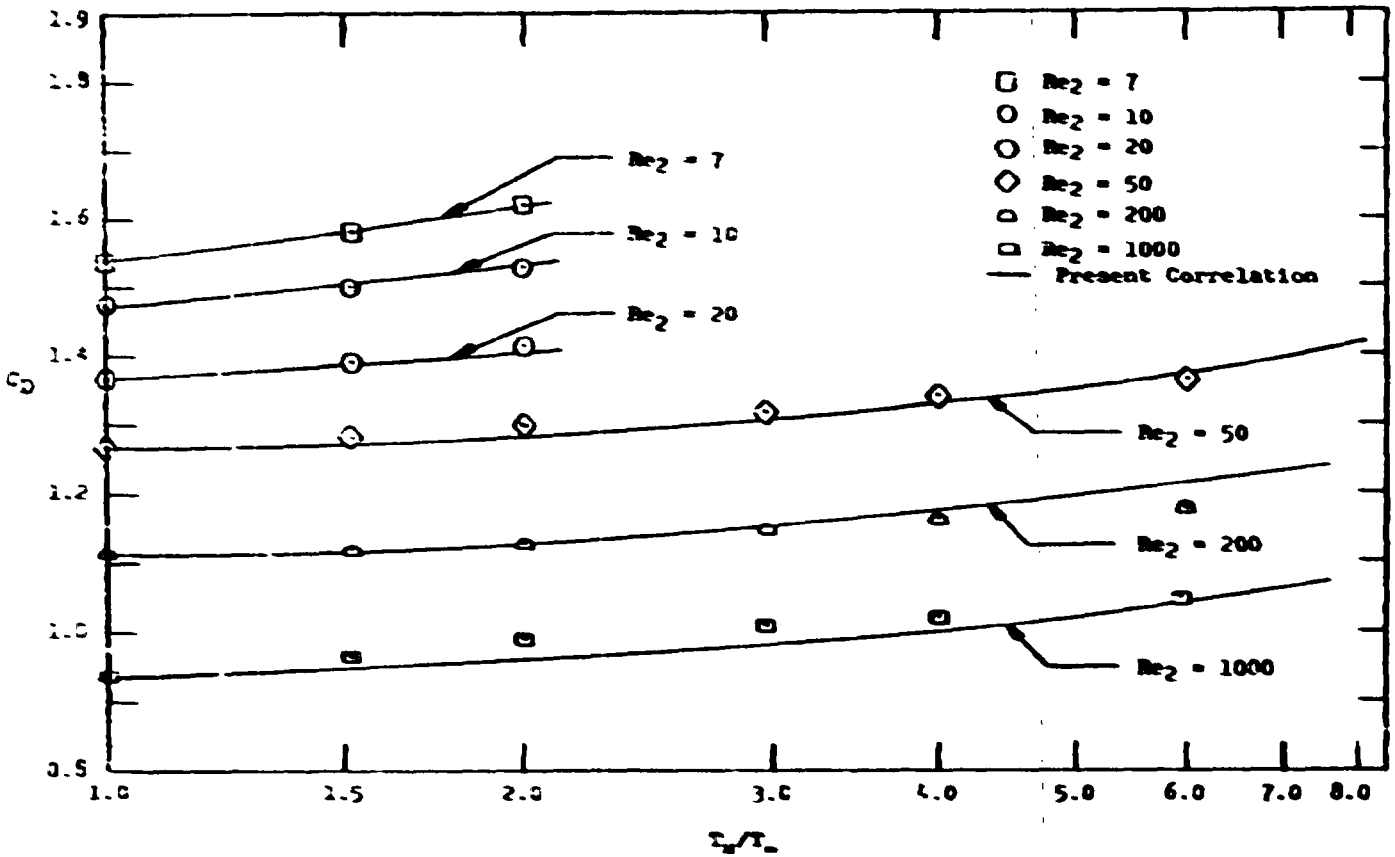

Figure 6. The Comparison of Temperature Dependent Sphere Drag Data with the Present Correlation (M_∞ = 6.0).

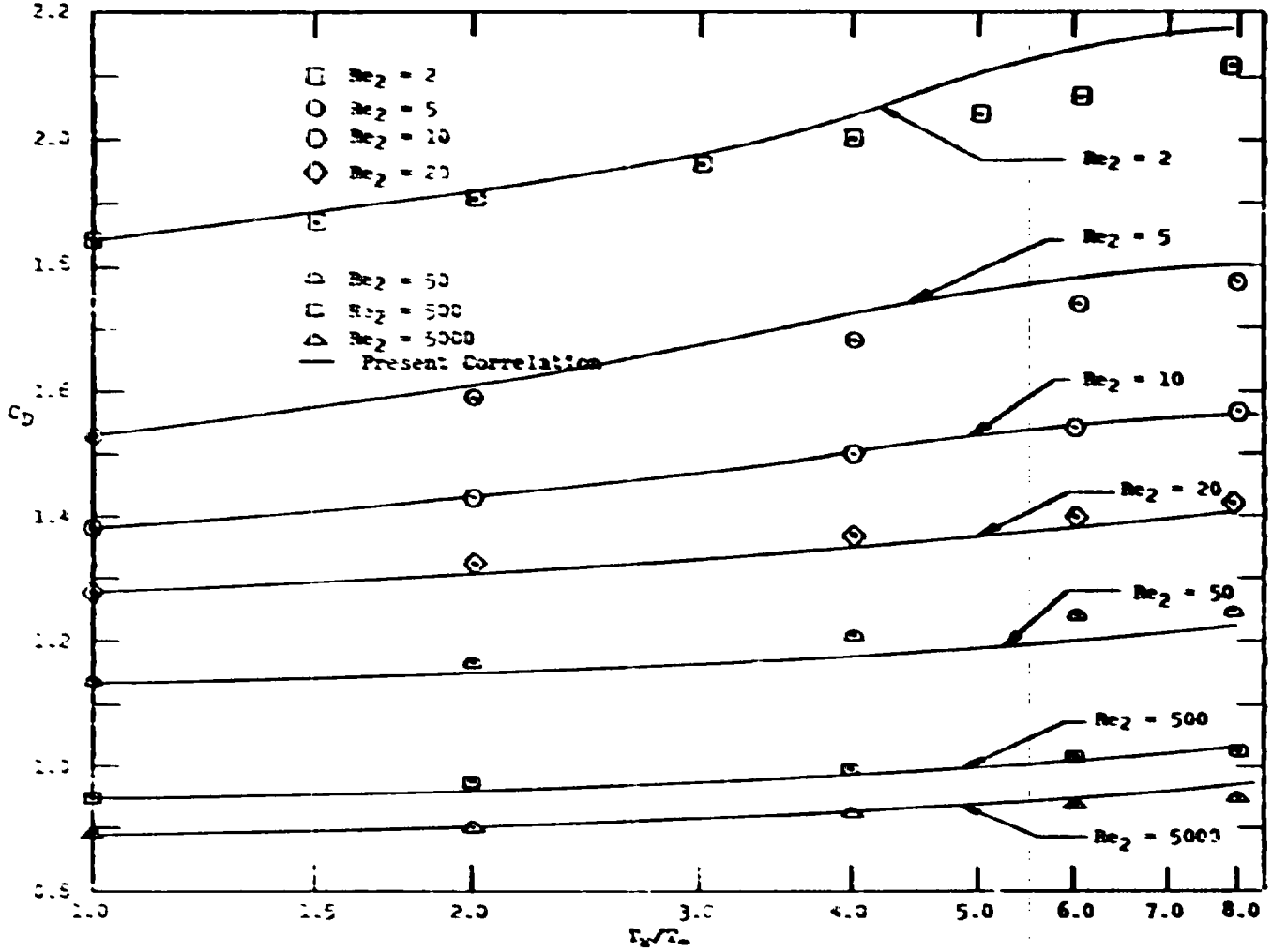

Figure 7. The Comparison of Temperature Dependent Sphere Drag Data with the Present Correlation (M_∞ = 10.4).

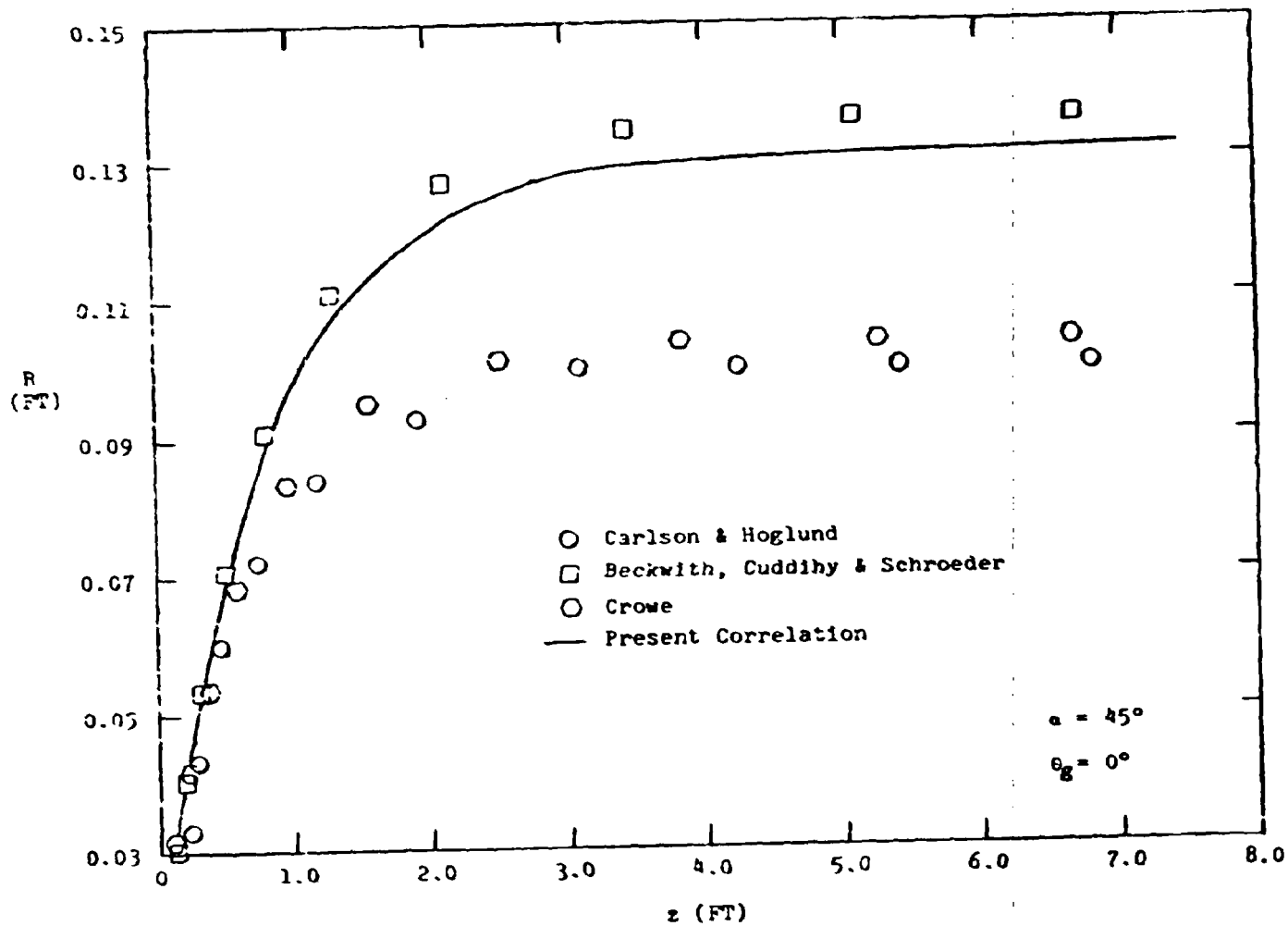

Figure 8. Trajectory of Particle in Air for Uniform Flow Case for Different Drag Coefficient Correlations (r_p = 0.5 μm, u_{p_i} = 100 ft/s).

variations of the particle velocity and particle temperature obtained with the various drag coefficients are shown in Figures 9 and 10. It can be seen that there is little influence of the specific drag coefficient correlation on the particle velocity and temperature.

Since the gas velocity in this case is 2324 ft/s, an initial particle velocity of 2000 ft/s was chosen to investigate the effect of this variable. The results are shown in Figure 11, where again it is noted that large differences in the particle trajectories depending on the specific drag coefficient correlation are found. Also, as shown in Figures 12 and 13 the corresponding variations of particle velocity and particle temperature show little influence of the drag coefficient correlation.

The particle size in the previous cases was relatively small. Therefore, the case where a 100 μm diameter particle was injected in air at an initial velocity of 100 ft/s at an angle of 45° was investigated. The particle trajectories for the sphere drag coefficient correlations for this case are shown in Figure 14. It is interesting to note that for this particle size, there is no significant difference in trajectories, as experienced with the 1 μm particle diameter, for the four different sphere drag correlations. However, as shown in Figures 15 and 16, there are significant differences in particle velocity and temperatures. Hence, accurate sphere drag coefficients are required for all particle sizes to correctly predict the trajectory, velocity, and temperature of the particles.

Other cases were investigated for particle injection into a uniform flow and are contained in Appendix A. These cases are for particle radii of 0.5, 5, 25, and 50 μm and for initial particle velocities of 100, 1000, and 2000 ft/s. The results of these calculations are similar to those discussed above.

2. Prandtl-Meyer Expansion Fan

A series of numerical experiments were conducted to examine particle trajectories through simple expansion waves. Typical results for a 1 μm diameter particle with an initial velocity of 100 ft/s traveling through a Prandtl-Meyer expansion fan with a total turning angle of 30° are shown in Figure 17. Results are given for all four drag coefficient correlations examined, and it is clear that the drag coefficient correlation has a significant effect on the particle trajectories through the expansion fan. It is also interesting to note that the corresponding particle velocity and particle temperature variations through the expansion fan shown in Figures 18 and 19 show little difference in the sphere drag coefficient correlation used.

As in the uniform flow investigation, this case was also examined for an initial velocity of 2000 ft/s. The resulting particle trajectories shown in Figure 20 display even more significant differences. Notably the results with the present sphere drag coefficient

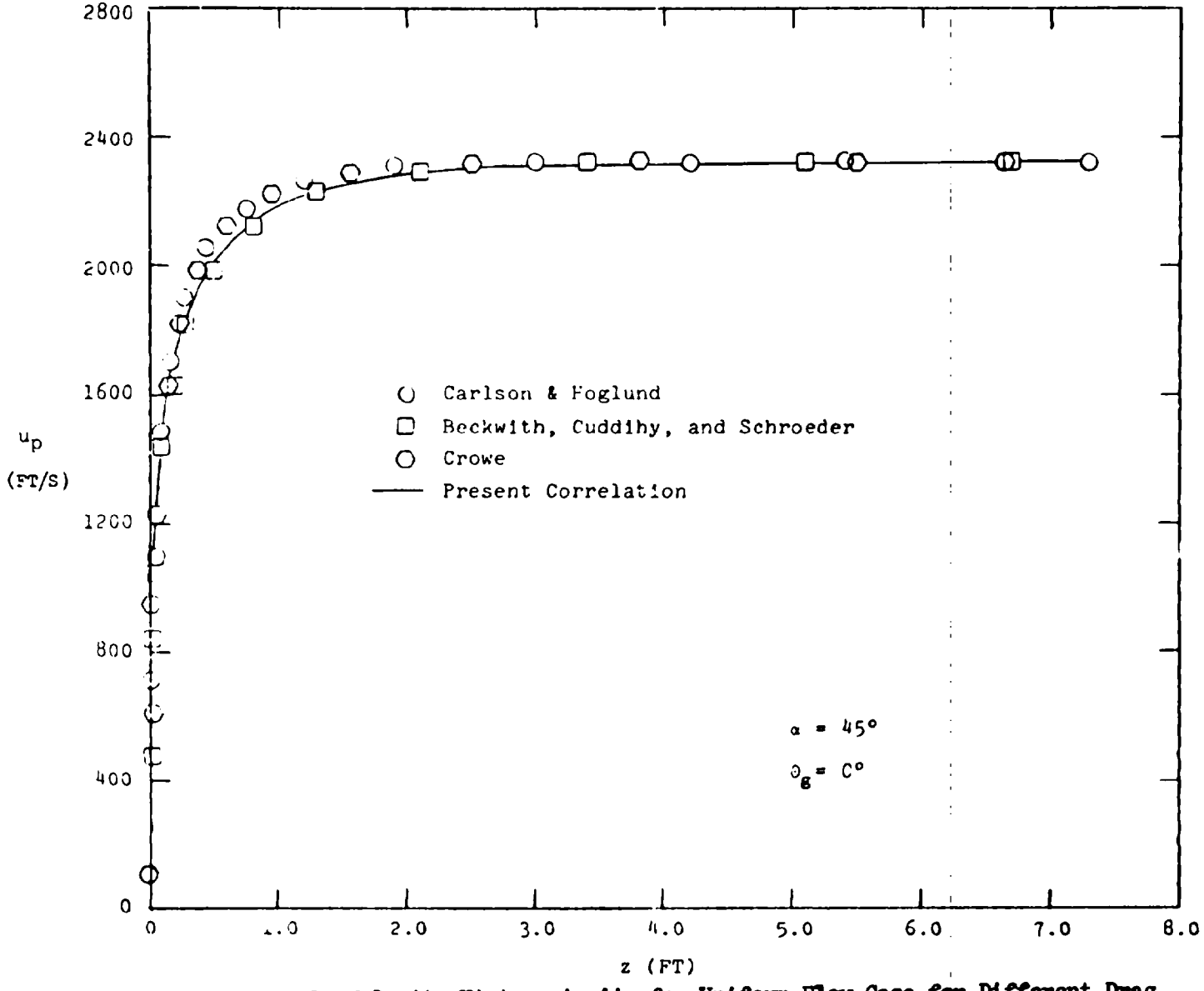

Figure 9. Particle Velocity History in Air for Uniform Flow Case for Different Drag Coefficient Correlations (r_p = 0.5 μm, u_{p_i} = 100 ft/s).

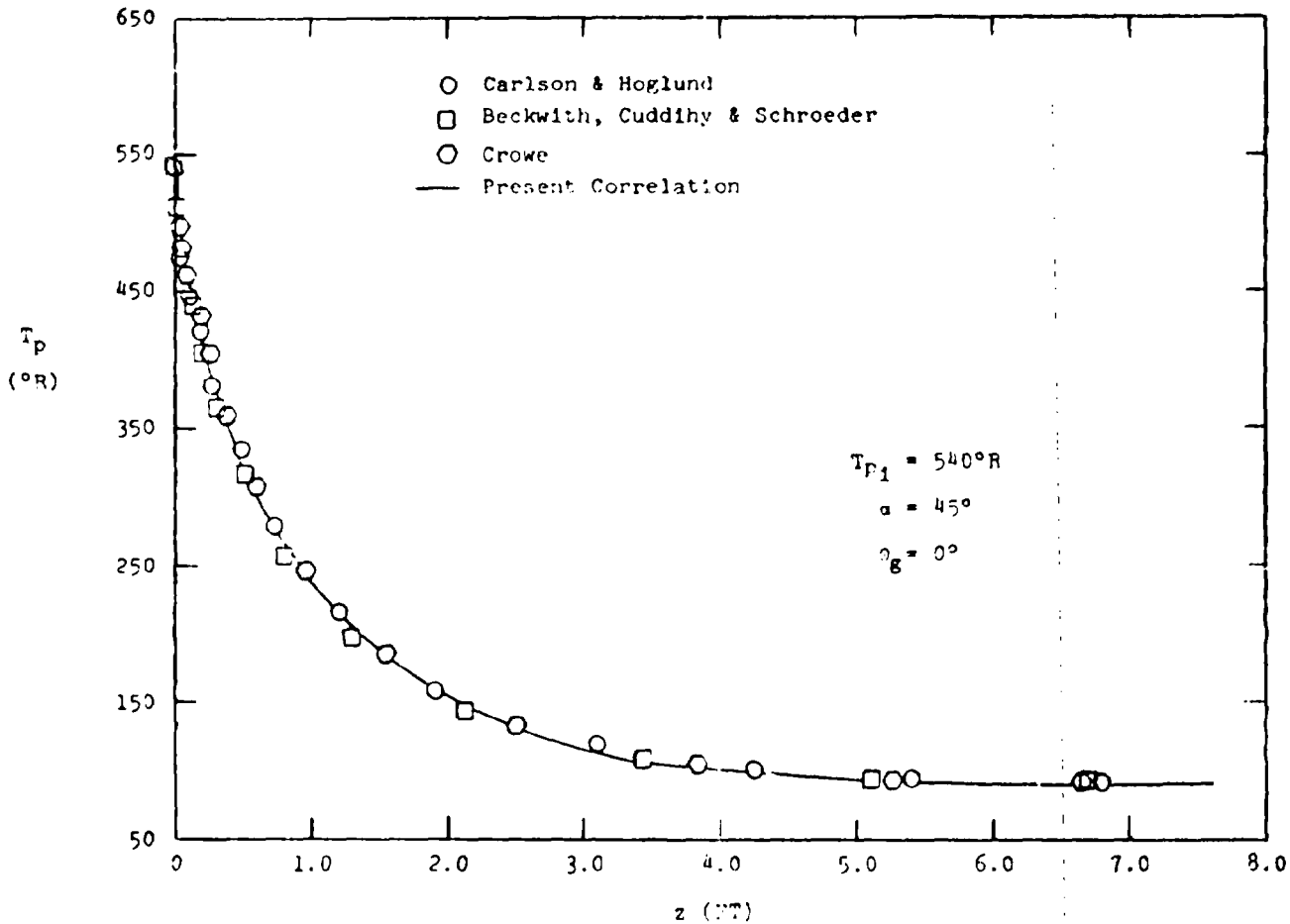

Figure 10. Particle Temperature History in Air for Uniform Flow Case for Different Drag Coefficient Correlations (r_p = 0.5 μm, u_{p_i} = 100 ft/s).

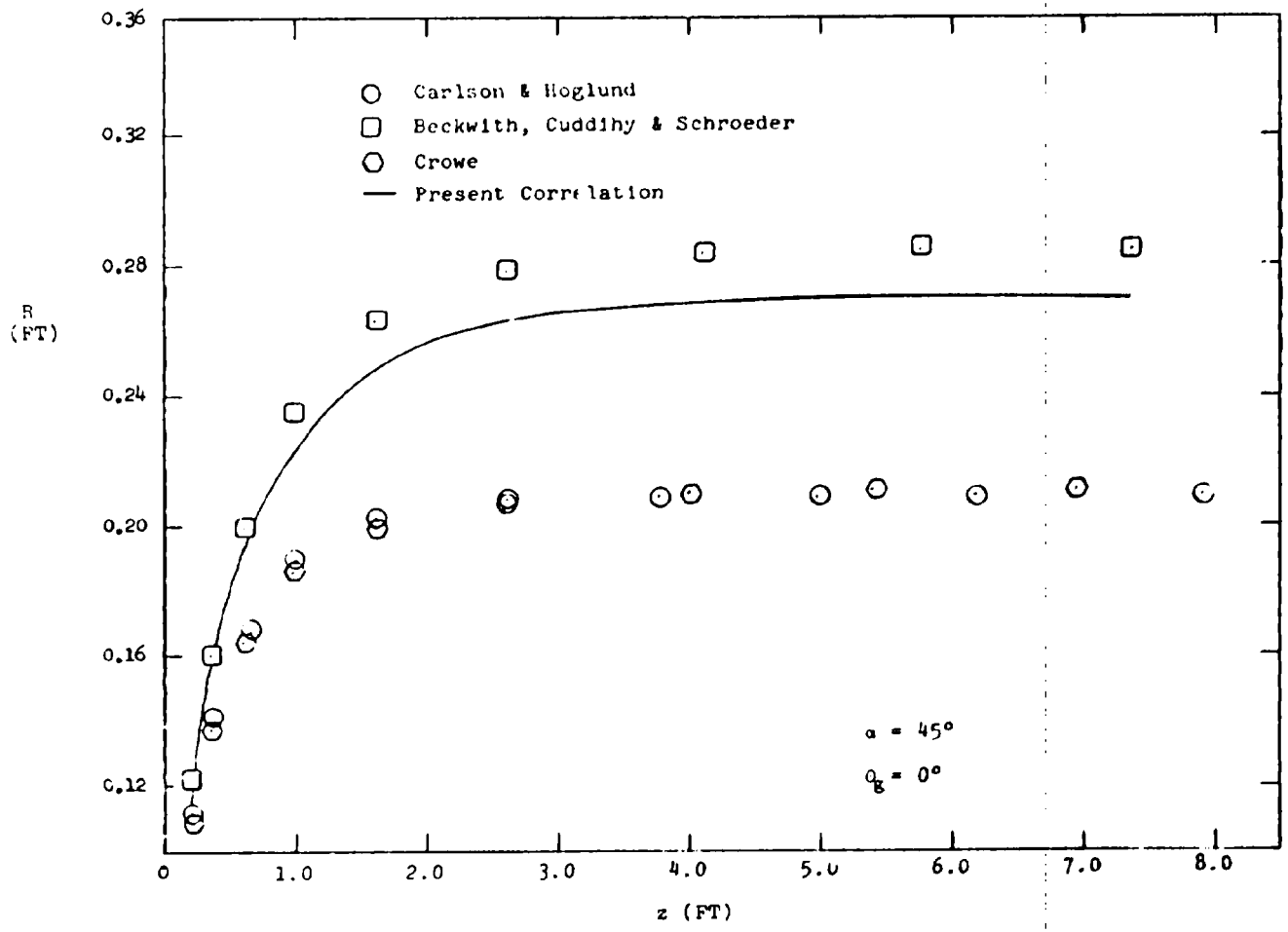

Figure 11. Trajectory of Particle in Air for Uniform Flow Case for Different Drag Coefficient Correlations (r_p = 0.5 μm, u_{p_i} = 2000 ft/s).

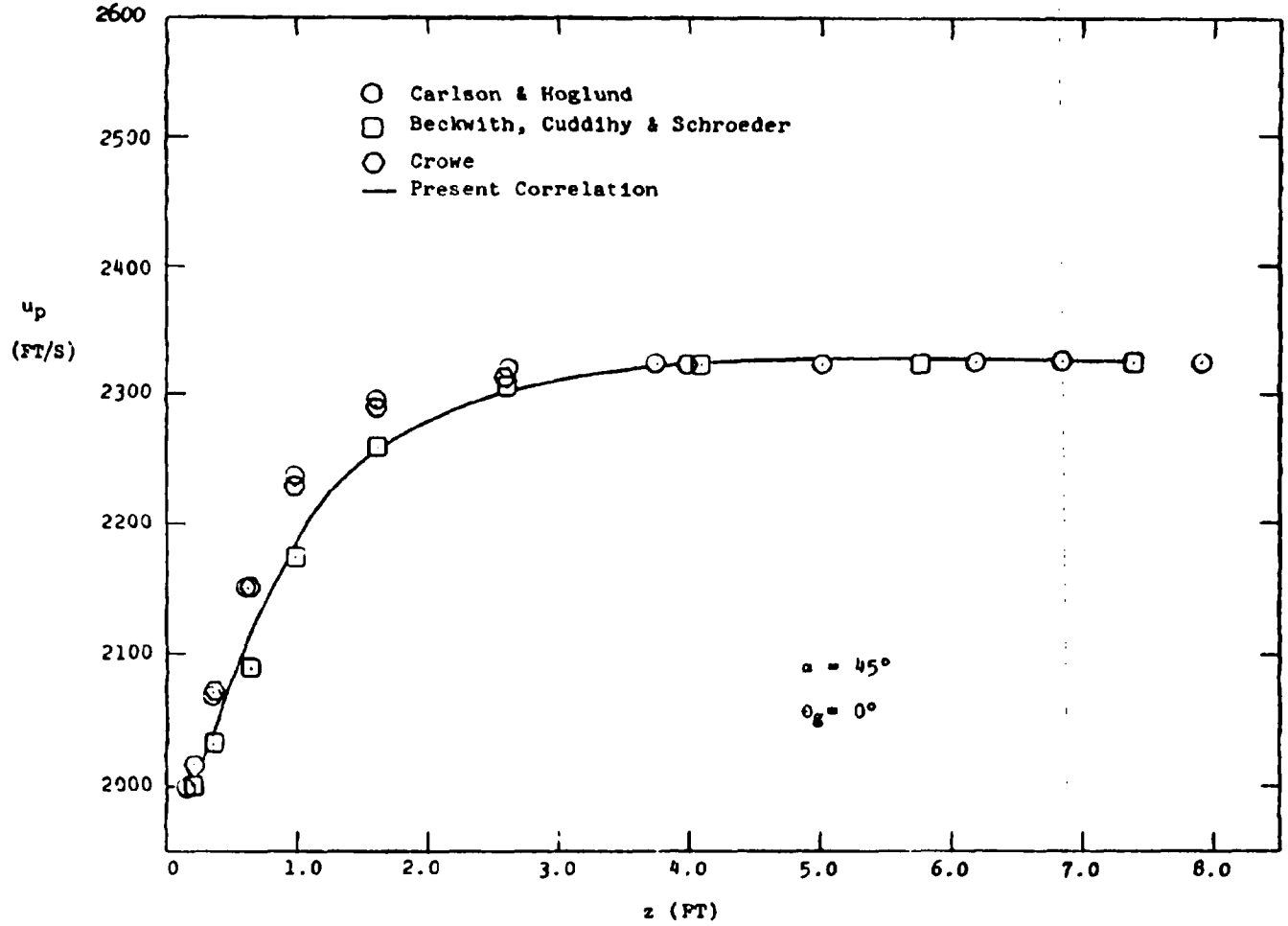

Figure 12. Particle Velocity History in Air for Uniform Flow Case for Different Drag Coefficient Correlations (r_p = 0.5 μm, u_{p_i} = 2000 ft/s).

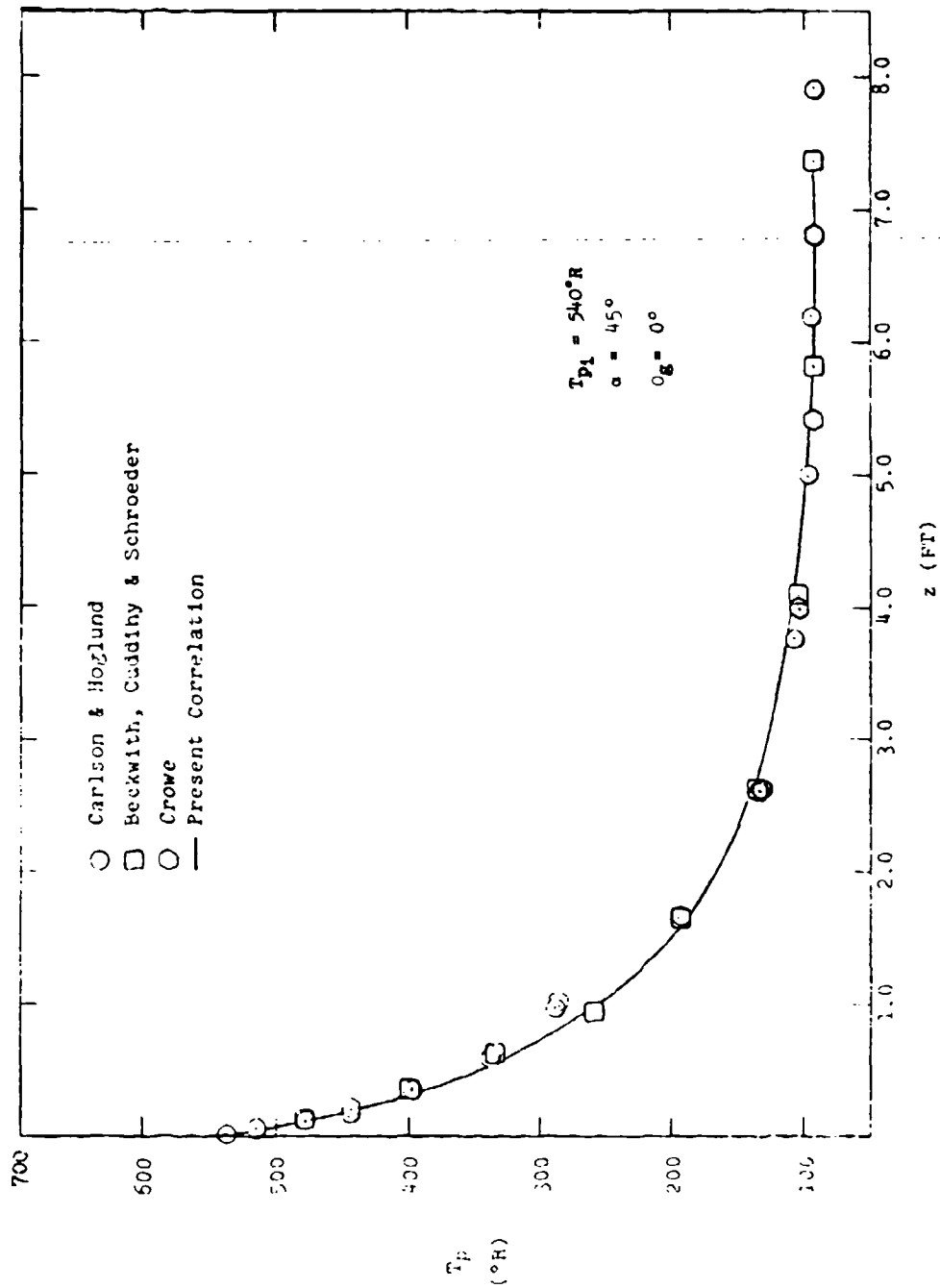

Figure 13. Particle Temperature History in Air for Uniform Flow Case for Different Drag Coefficient Correlations (r_p = 0.5 μm, u_{p_1} = 2000 ft/s).

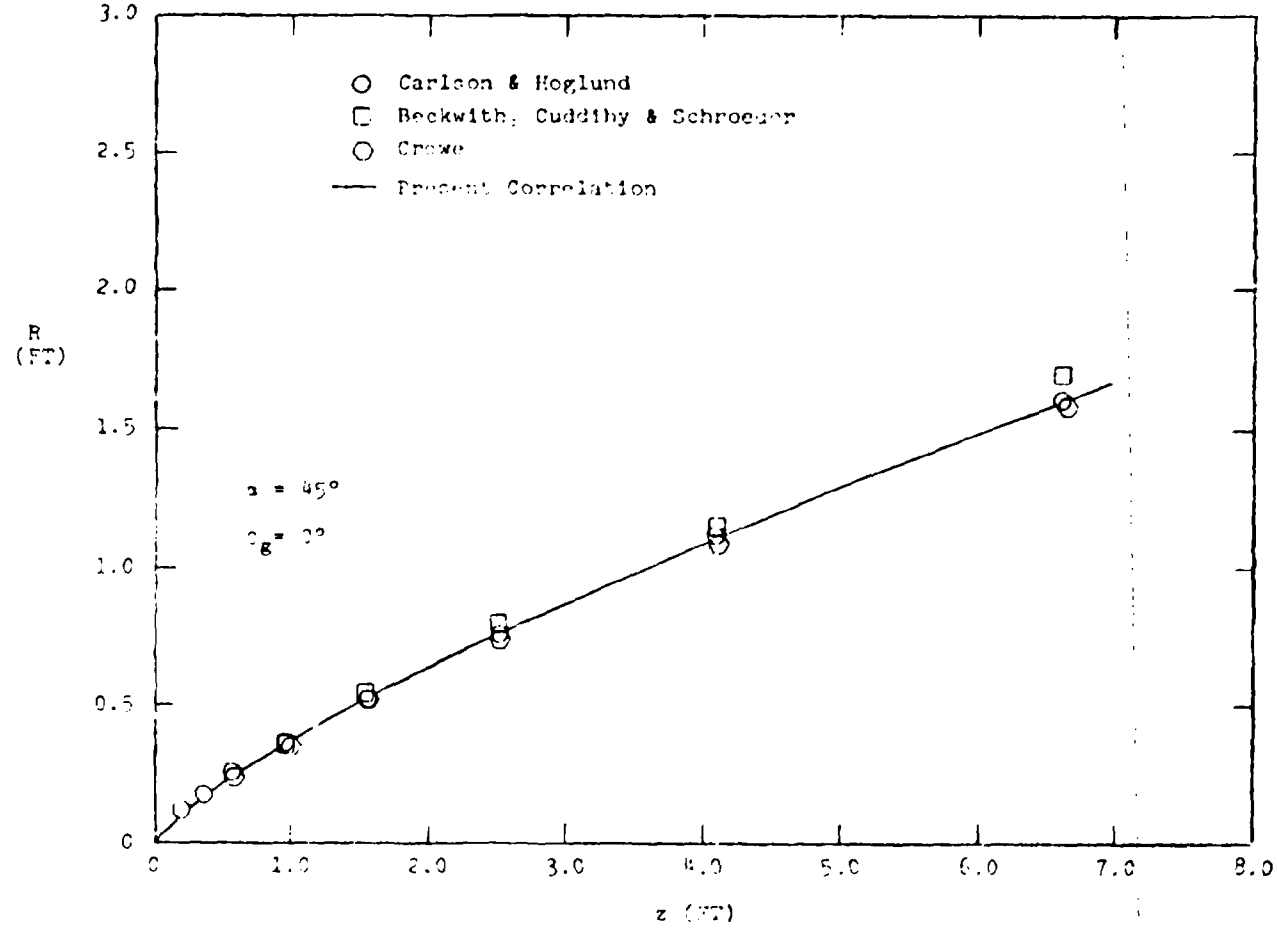

Figure 14. Trajectory of Particle in Air for Uniform Flow Case for Different Drag Coefficient Correlations (r_p = 50 μm, u_{p_i} = 100 ft/s).

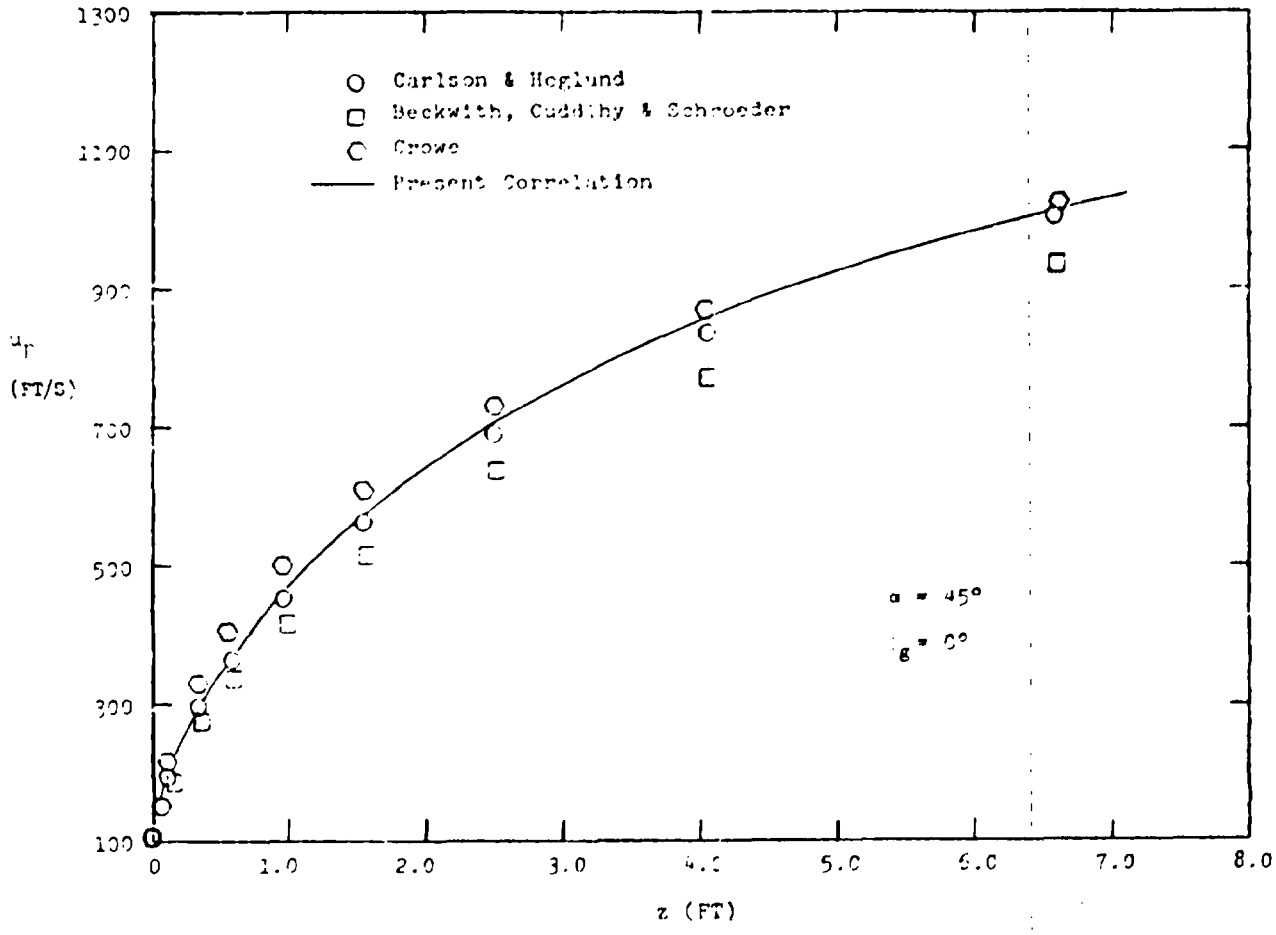

Figure 15. Particle Velocity History in Air for Uniform Flow Case for Different Drag Coefficient Correlations (r_p = 50 μm, u_{p_i} = 100 ft/s).

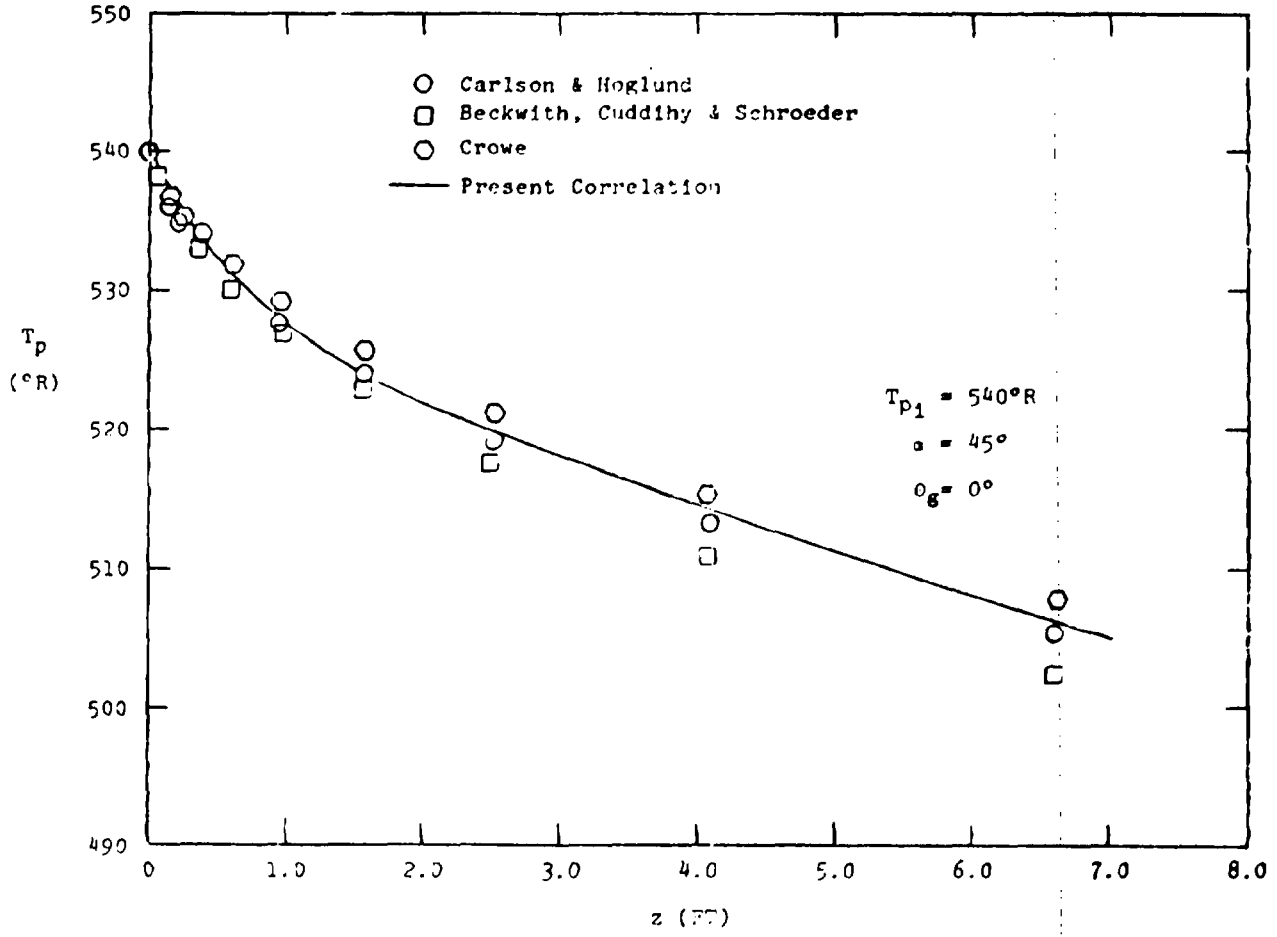

Figure 16. Particle Temperature History in Air for Uniform Flow Case for Different Drag Coefficient Correlations (r_p = 0.5 μm, u_{p_i} = 100 ft/s).

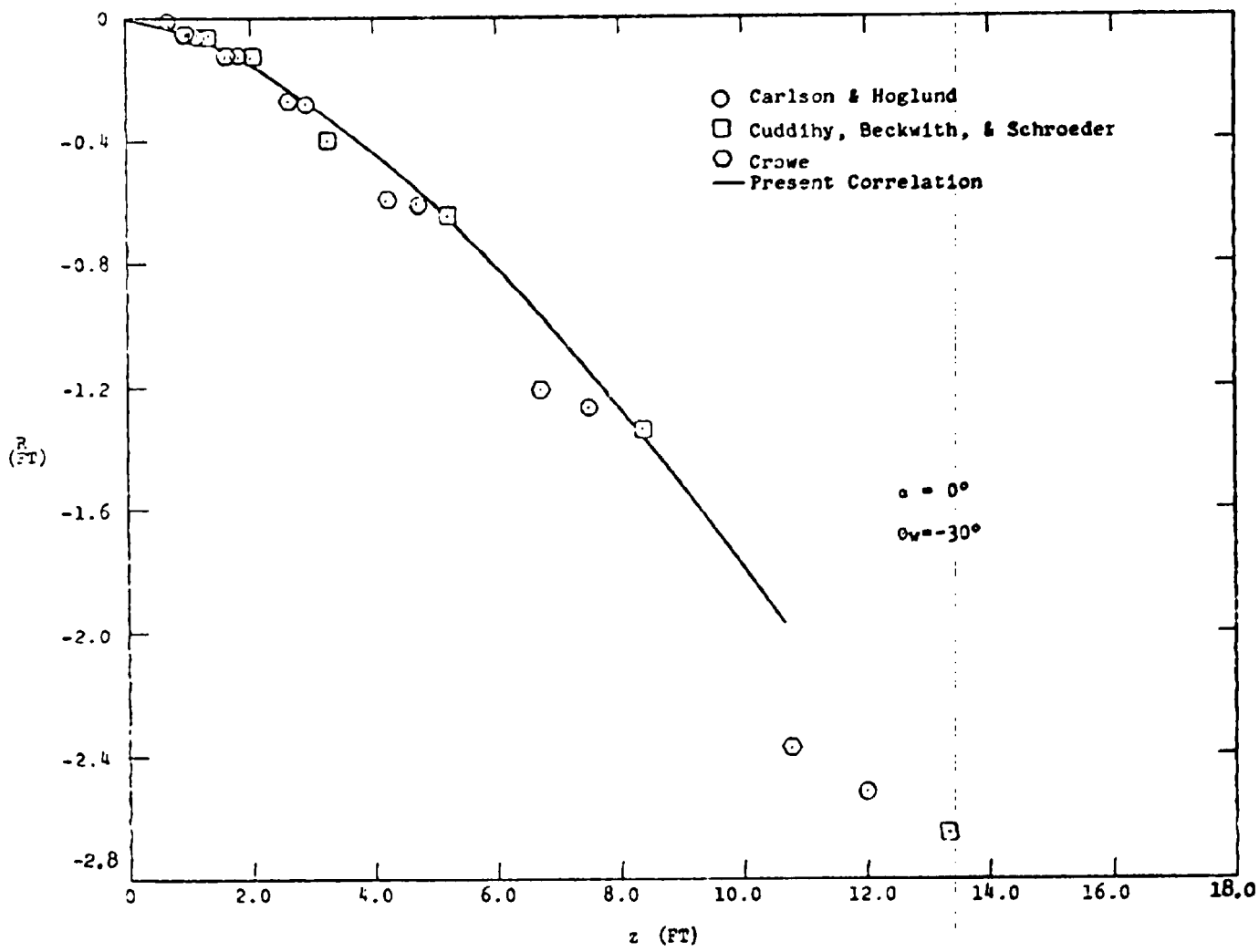

Figure 17. Trajectory of Particle Passing Through Prandtl-Meyer Expansion Fan in Air for Different Drag Coefficient Correlations (r_p = 0.5 μm, u_{p_i} = 100 ft/s).

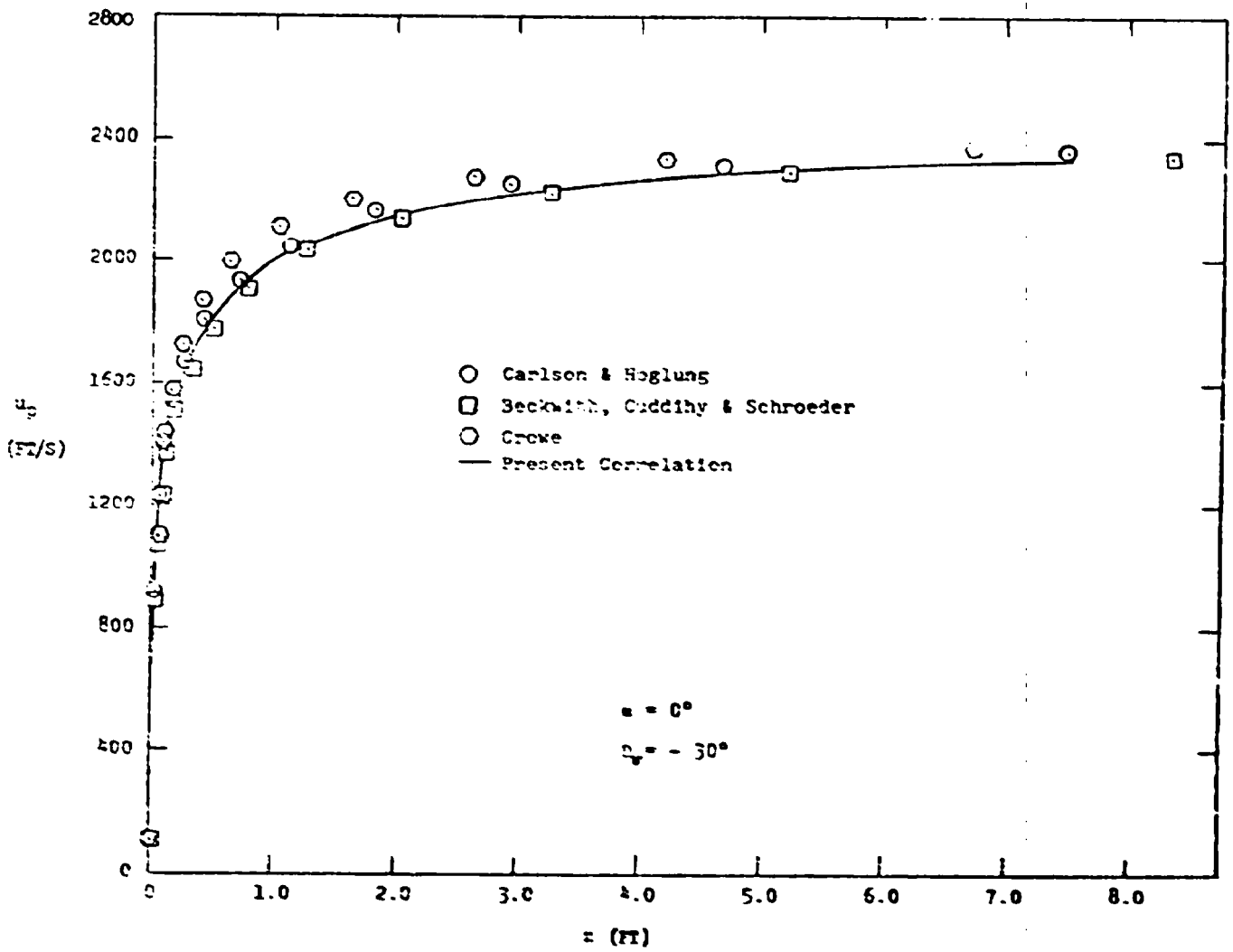

Figure 18. Particle Velocity History Through Prandtl-Meyer Expansion Fan in Air for Different Drag Coefficient Correlations (r_p = 0.5 μm, u_{p_i} = 100 ft/s).

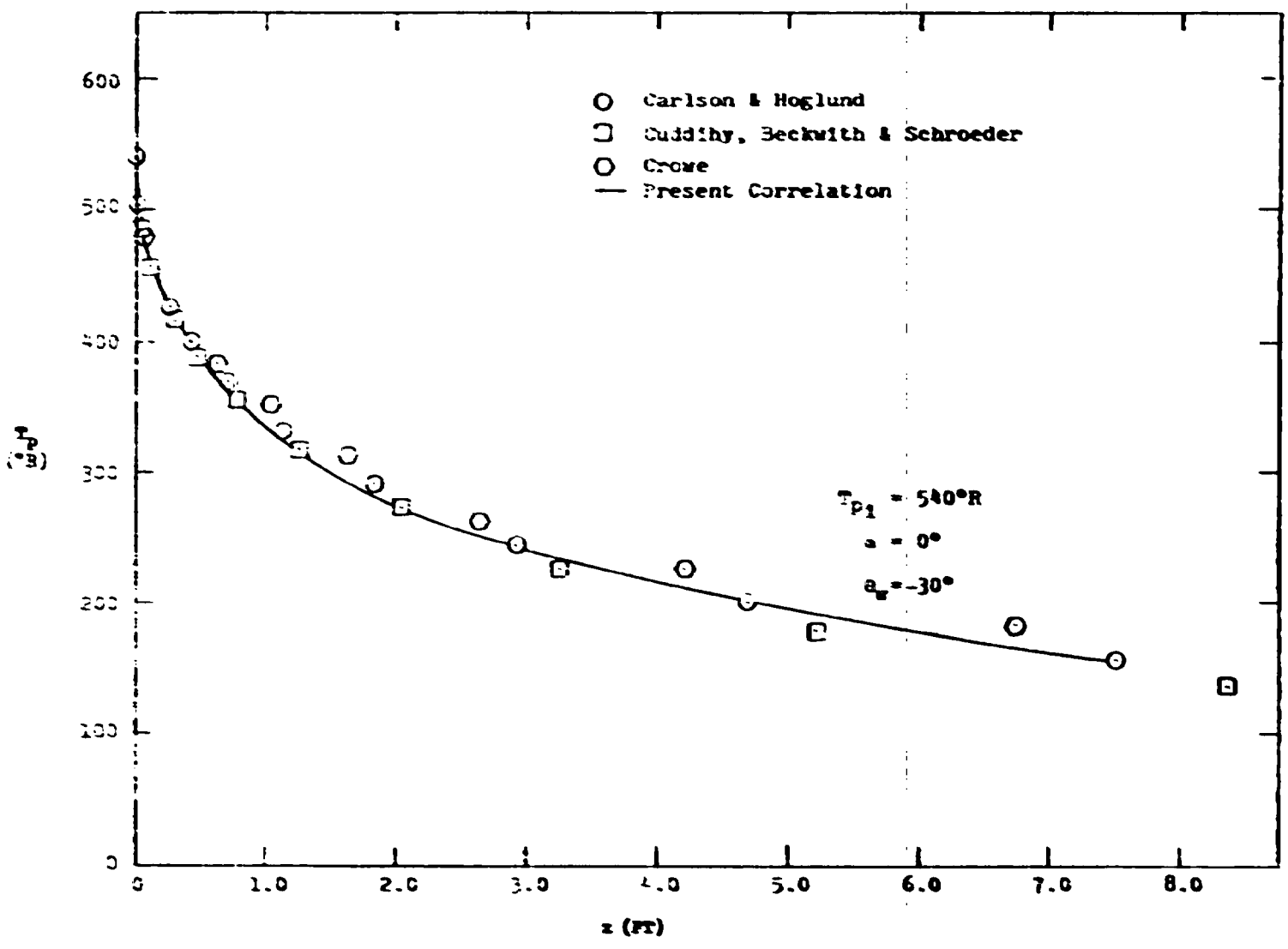

Figure 19. Particle Temperature History Through Prandtl-Meyer Expansion Fan in Air for Different Drag Coefficient Correlations (r_p = 0.5 μm, u_{p_i} = 100 ft/s).

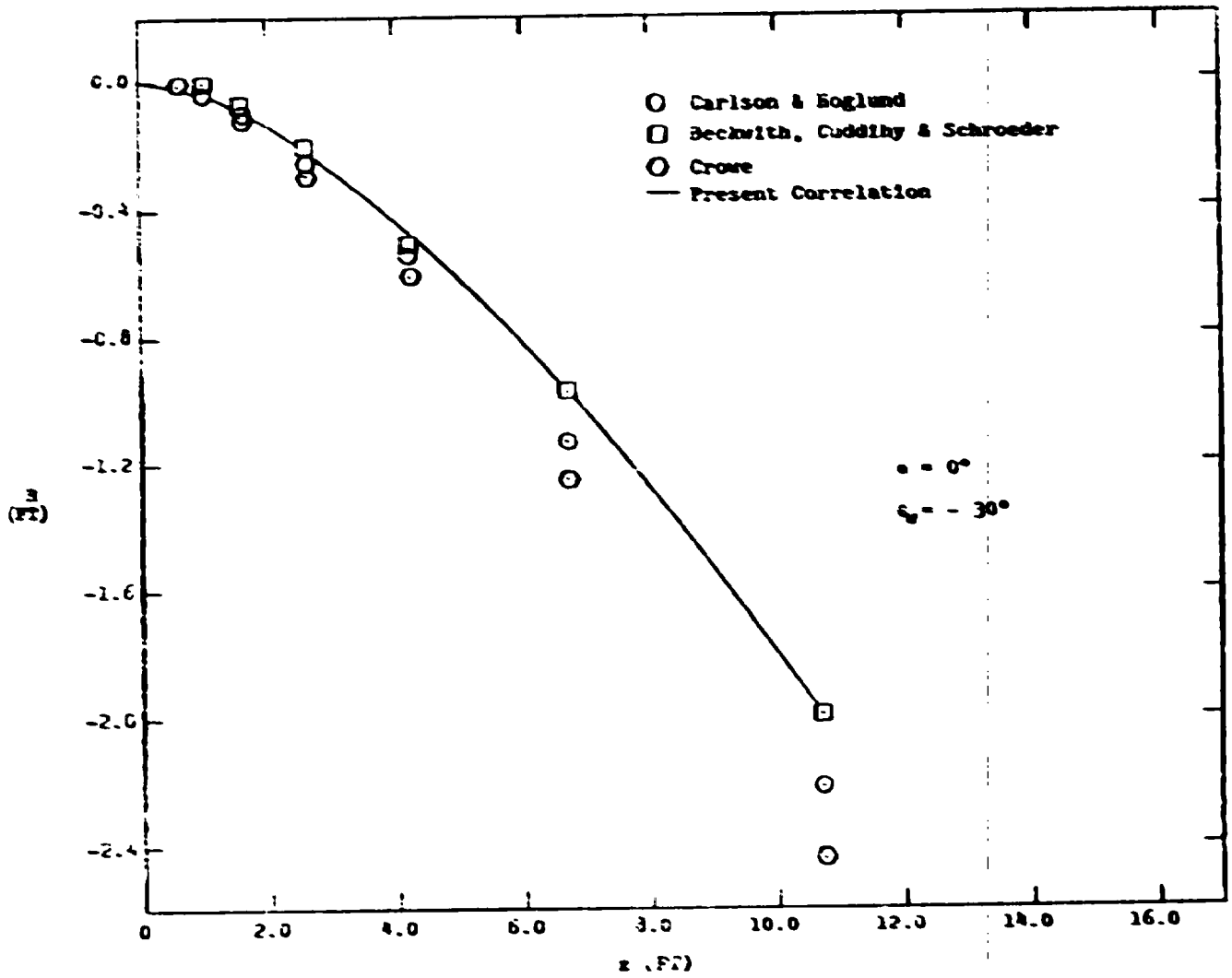

Figure 20. Trajectory of Particle Passing Through Prandtl-Meyer Expansion Fan in Air for Different Drag Coefficient Correlations (r_p = 0.5 μm, u_{Pi} = 2000 ft/s).

correlation are similar to those using the Cuddihy, Beckwith, and Schroeder[17] correlation. The corresponding particle velocity and particle temperature variations are shown in Figures 21 and 22. These results indicate a significant difference in the particle velocities 3 to 4 feet downstream from the turning point; however, there is little difference in the particle temperatures.

As a means of comparison, the case for a 100 μm diameter particle with an initial velocity of 100 ft/s is shown in Figure 23. Here again, the trajectories for the larger particle show little effect due to changes in the sphere drag coefficient as opposed to those for the 1 μm diameter particles. The corresponding particle velocities shown in Figure 24, and the particle temperatures given in Figure 25 show greater effects of changes in the drag correlation.

Additional cases were also investigated for the Prandtl-Meyer expansion fan and are contained in Appendix B. These cases are for particle radii of 0.5, 5, and 50 μm and for initial particle velocities of 100, 1000, and 2000 ft/s turning an angle of 30°.

3. Two-Dimensional Wedge/Oblique Shock

Numerical experiments were conducted to determine the trajectories, velocities, and temperatures of the particles when passing through a two-dimensional oblique shock wave. A 30° wedge in a Mach 5 air flow which generated an oblique shock with an angle of approximately 42° was chosen. The trajectory of a particle with a 10 μm diameter and an initial velocity of 100 ft/s was computed for the four sphere drag coefficient correlations, with the results shown in Figure 26. It can be seen that there is no significant difference in the particle trajectories. This type of behavior is also exhibited in the particle velocity and particle temperature variation as shown in Figures 27 and 28. Therefore, in the compression case there is little variation in results as the sphere drag coefficient is changed. This is substantiated by the additional cases examined; these results are included in Appendix C for particle radii of 5 and 50 μm and for initial particle velocities of 100, 1000, and 2000 ft/s.

D. COMPOSITE SOLUTION TO DESCRIBE THE PARTICLE FLOW ABOUT A TWO-DIMENSIONAL WEDGE

The previous section described the particle behavior in simple flow situations, i.e., uniform flow, Prandtl-Meyer expansion fan, and an oblique shock. The flow field generated by a wedge when placed in a supersonic stream would contain all three of these flow situations. Therefore, a 10° half-angle two-dimensional wedge was chosen and placed into a Mach 2 air flow, and the computer program was used to determine the two-phase inviscid solution. This calculation was performed in two steps. First, given the free stream conditions and the wedge half-angle, one obtains the solution for a two-dimensional infinite wedge in

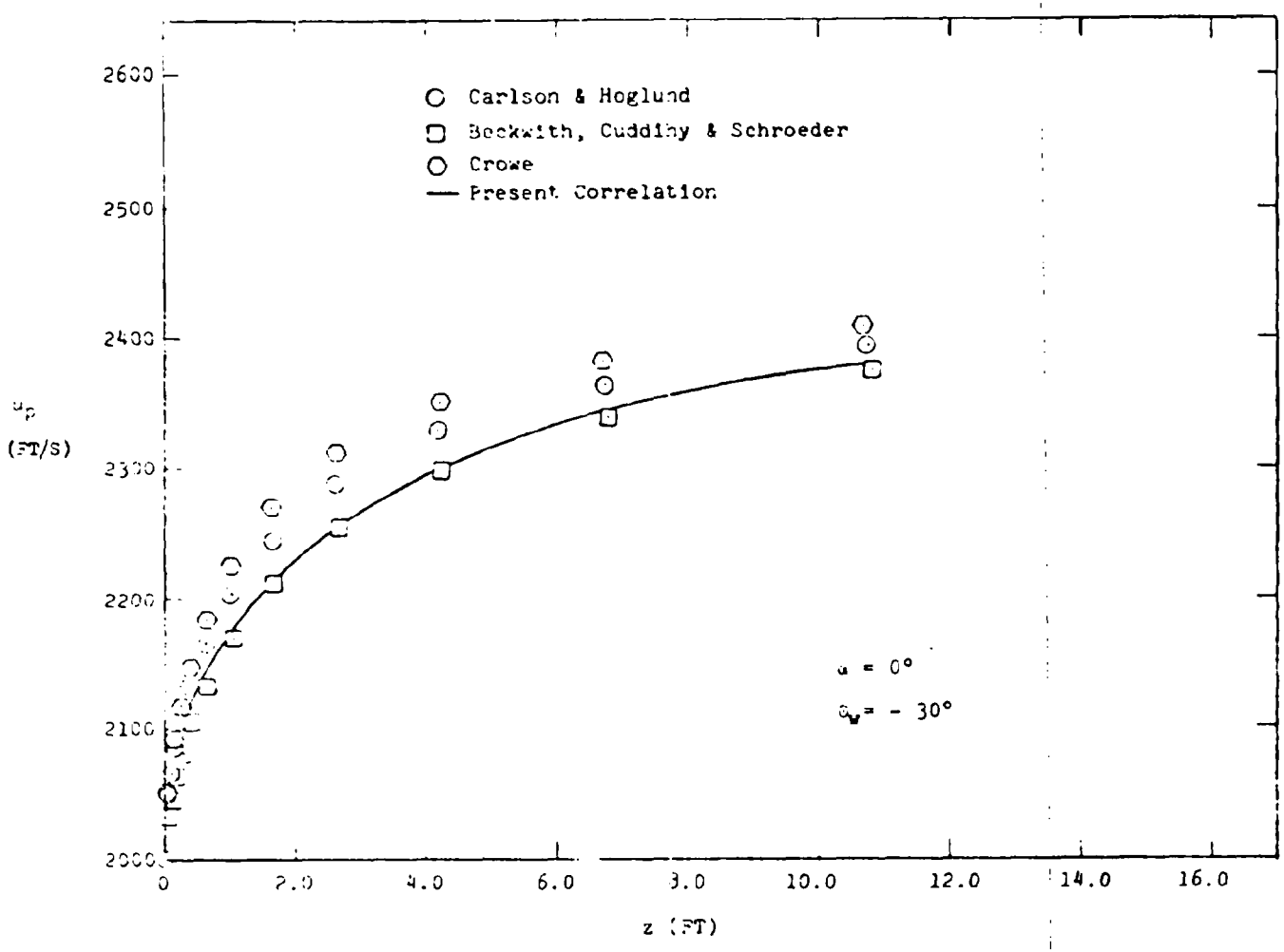

Figure 21. Particle Velocity History Through Prandtl-Meyer Expansion Fan in Air for Different Drag Coefficient Correlations (r_p = 0.5 μm, u_{p_i} = 2000 ft/s).

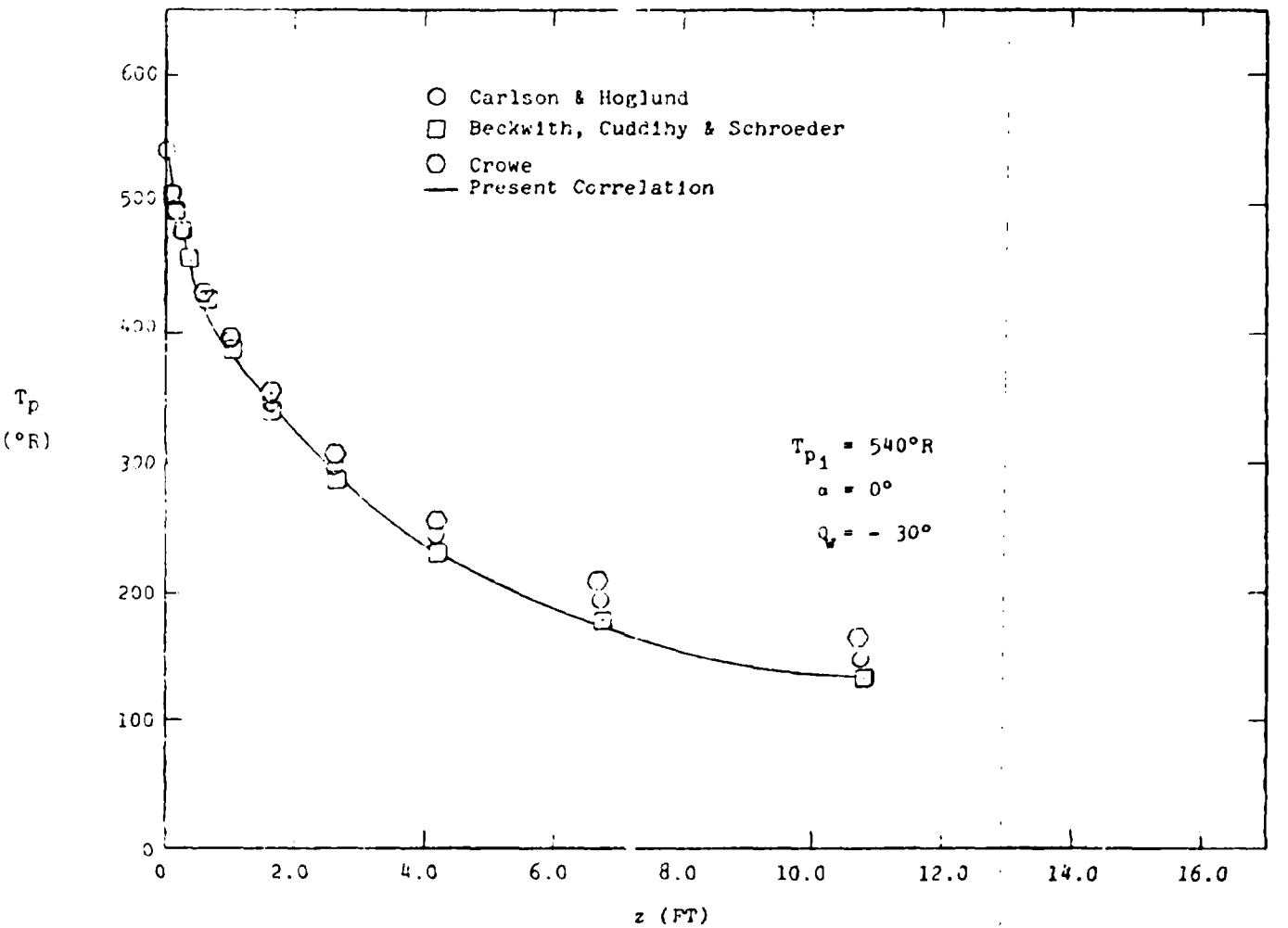

Figure 22. Particle Temperature History Through Prandtl-Meyer Expansion Fan in Air for Different Drag Coefficient Correlations (r_p = 0.5 μm, u_{p_i} = 2000 ft/s).

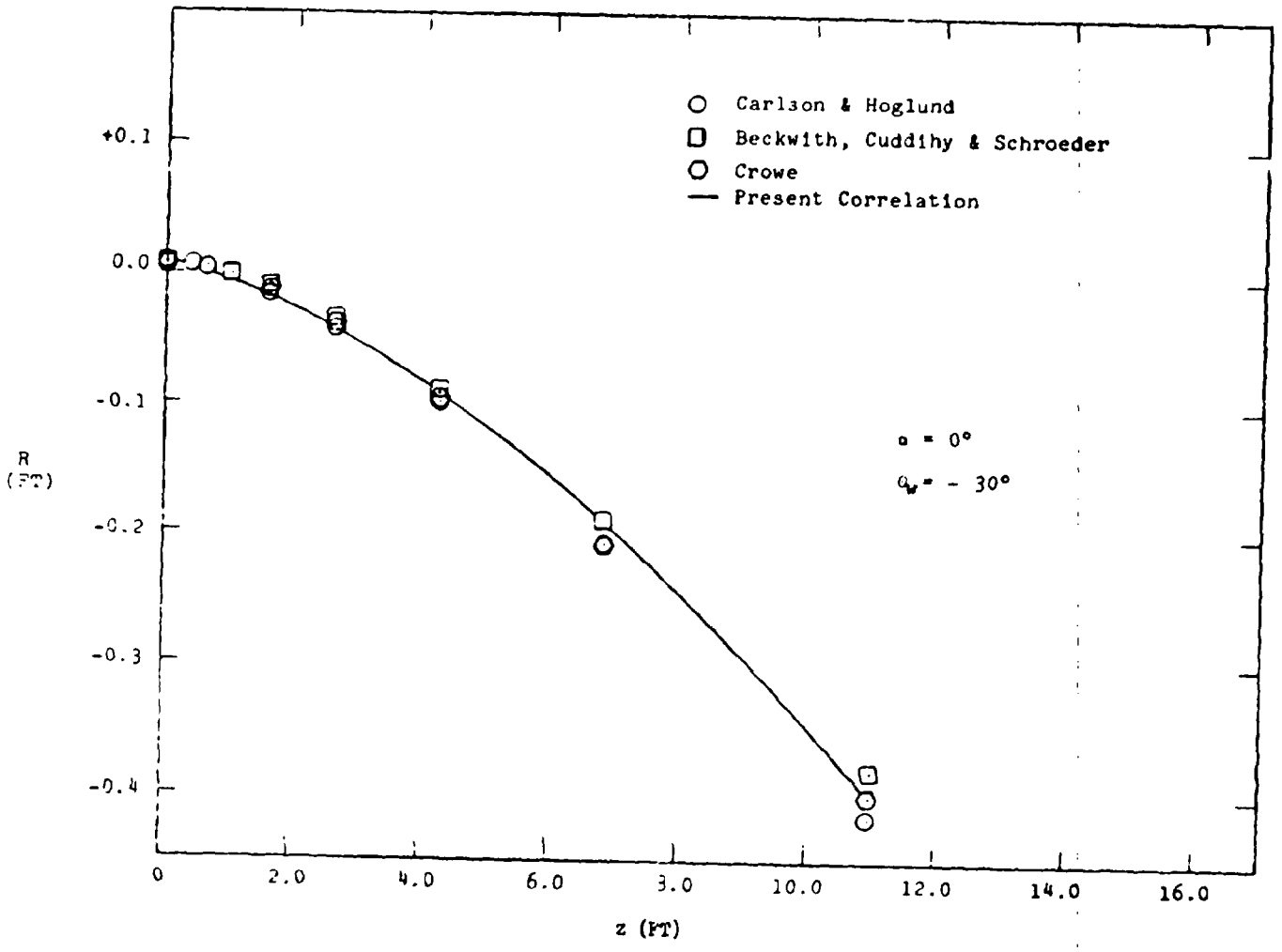

Figure 23. Trajectory of Particle Passing Through Prandtl-Meyer Expansion Fan in Air for Different Drag Coefficient Correlations (r_p = 50 μm, u_{p_i} = 100 ft/s).

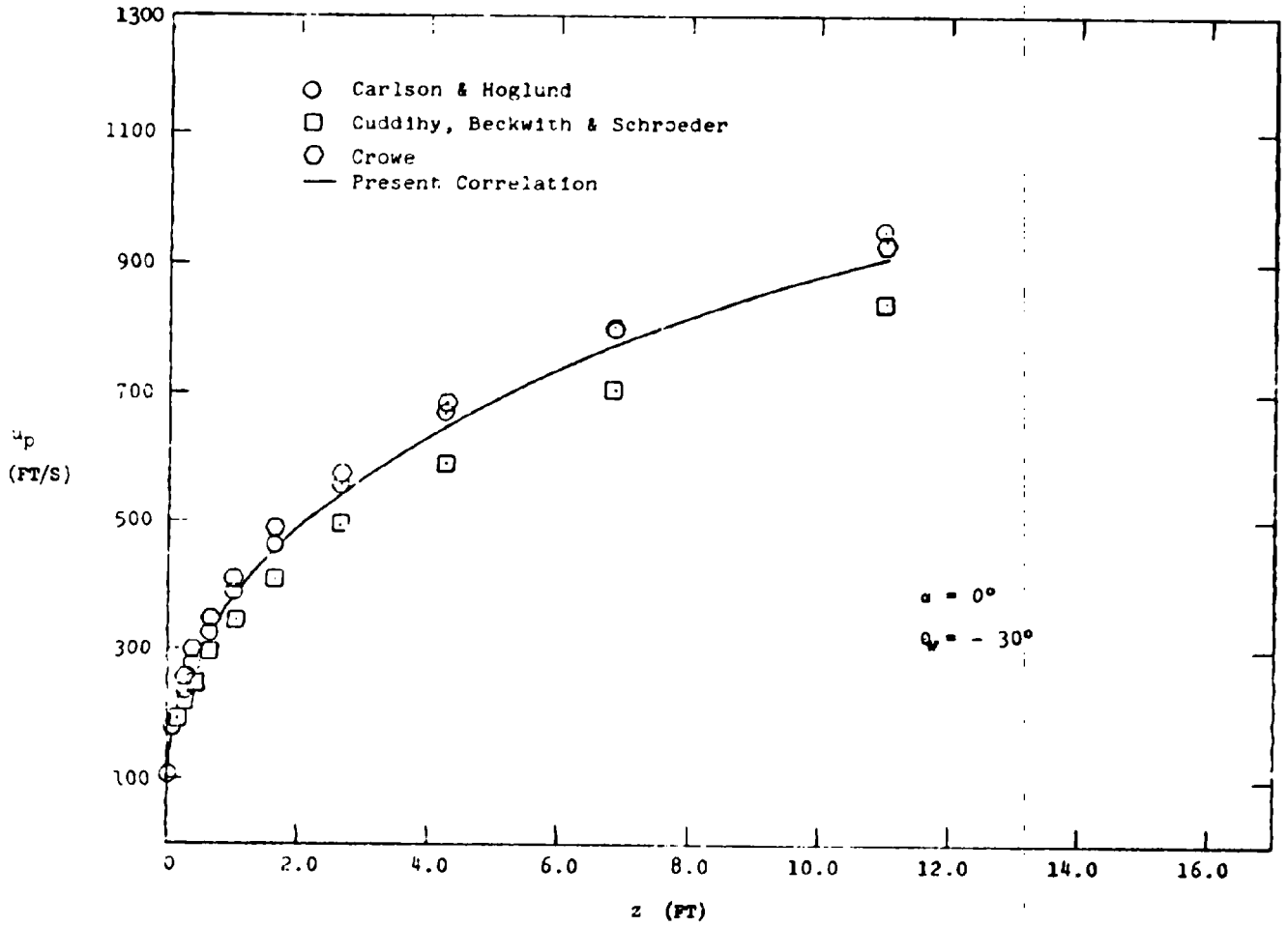

Figure 24. Particle Velocity History Through Prandtl-Meyer Expansion Fan in Air for Different Drag Coefficient Correlations (r_p = 50 μm, u_{pi} = 100 ft/s).

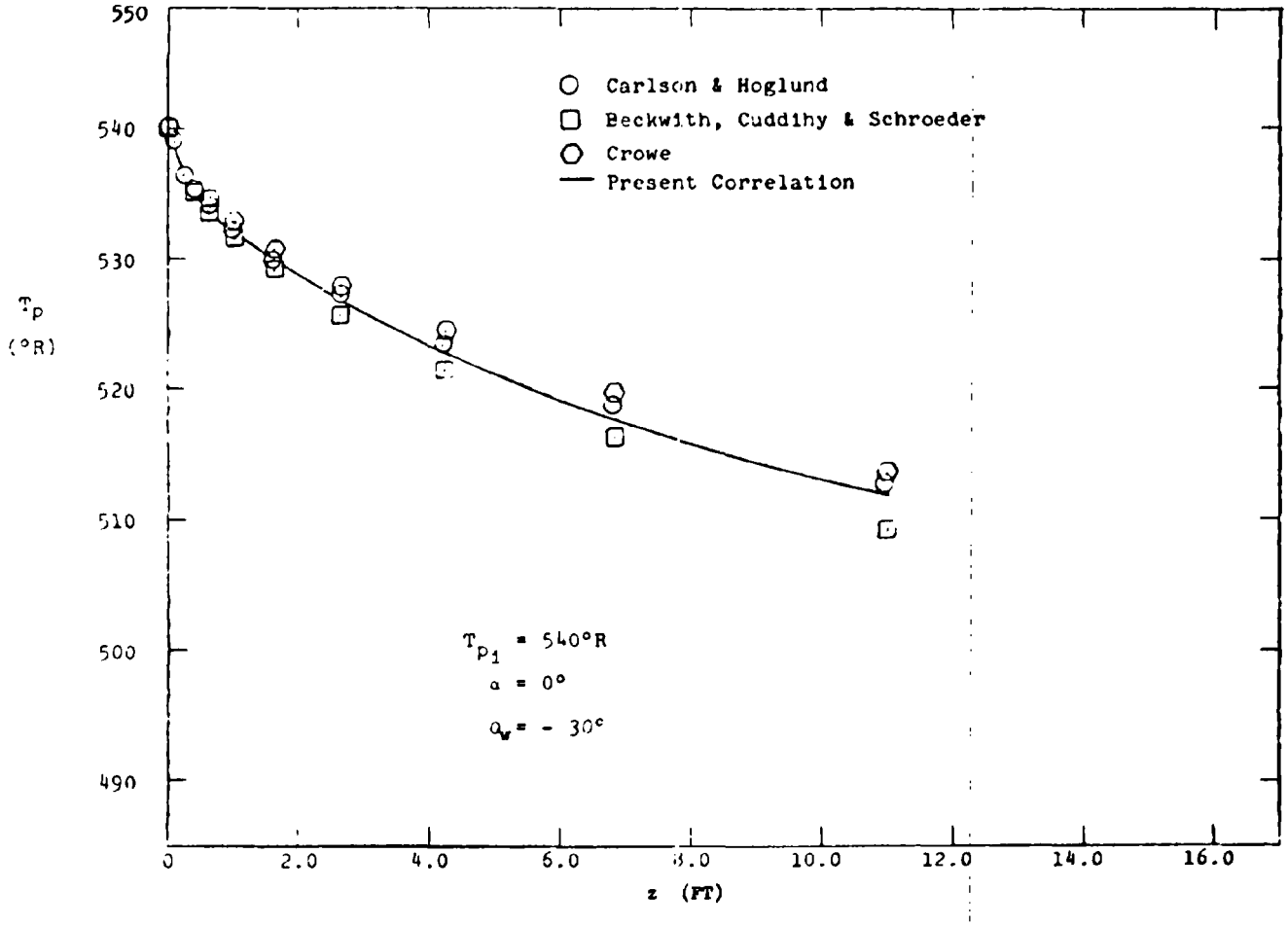

Figure 25. Particle Temperature History Through Prandtl-Meyer Expansion Fan in Air for Different Drag Coefficient Correlations (r_p = 50 μm, u_{p_1} = 100 ft/s).

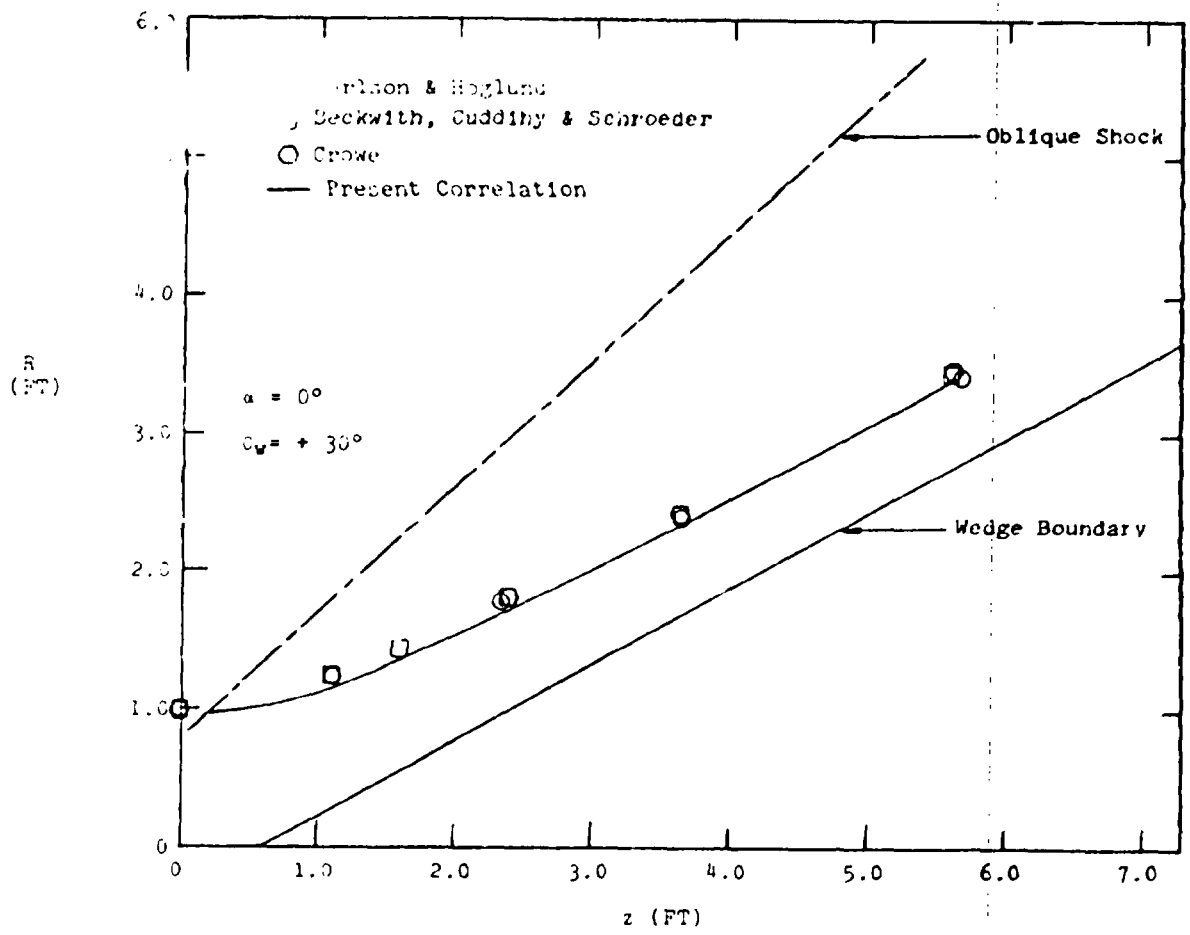

Figure 26. Trajectory of Particle Passing Through an Oblique Shock in Air for Different Drag Coefficient Correlations (r_p = 5μm, u_{p_i} = 100 ft/s).

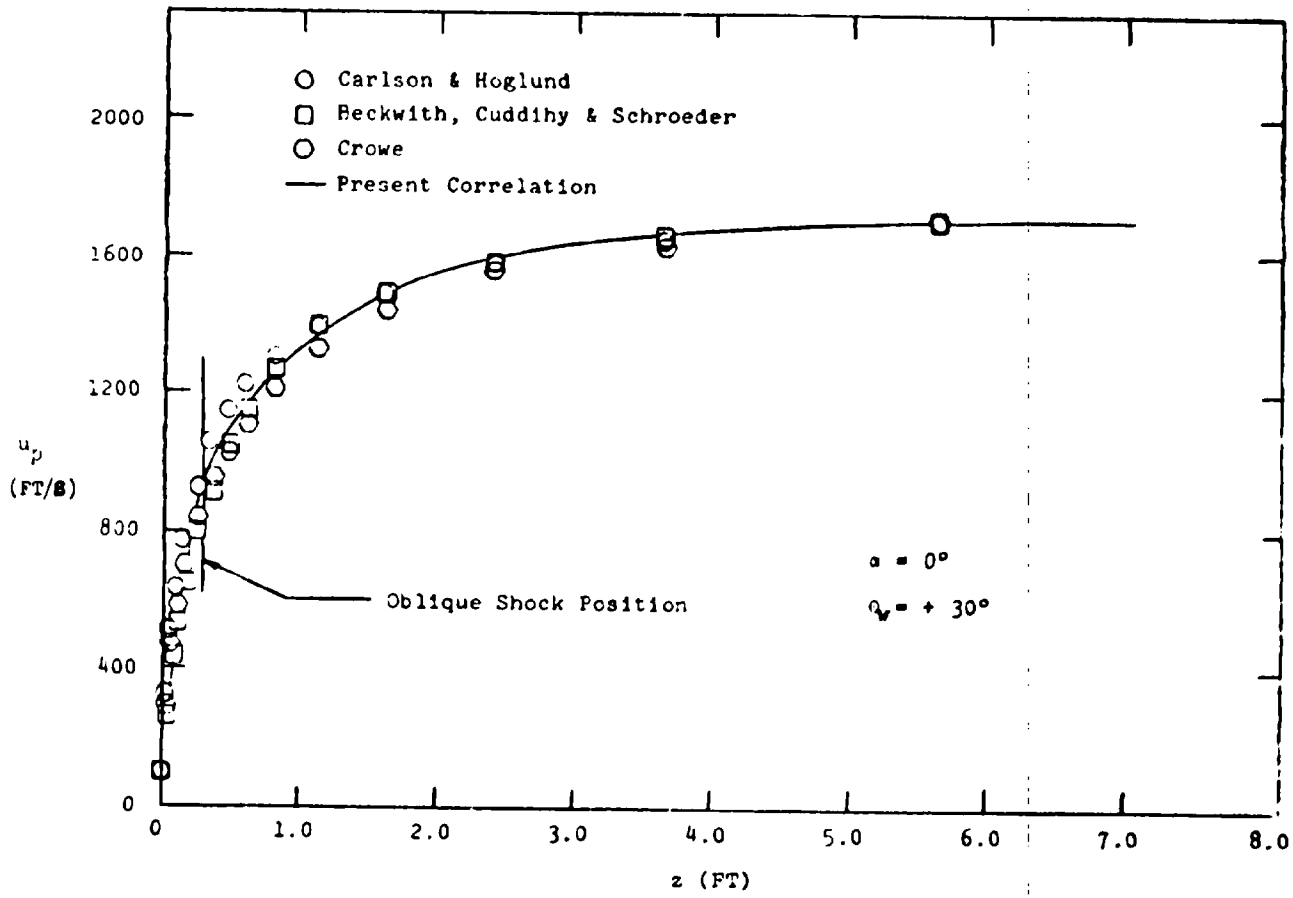

Figure 27. Particle Velocity History Through an Oblique Shock in Air for Different Drag Coefficient Correlations (r_p = 5 μm, u_{p_i} = 100 ft/s).

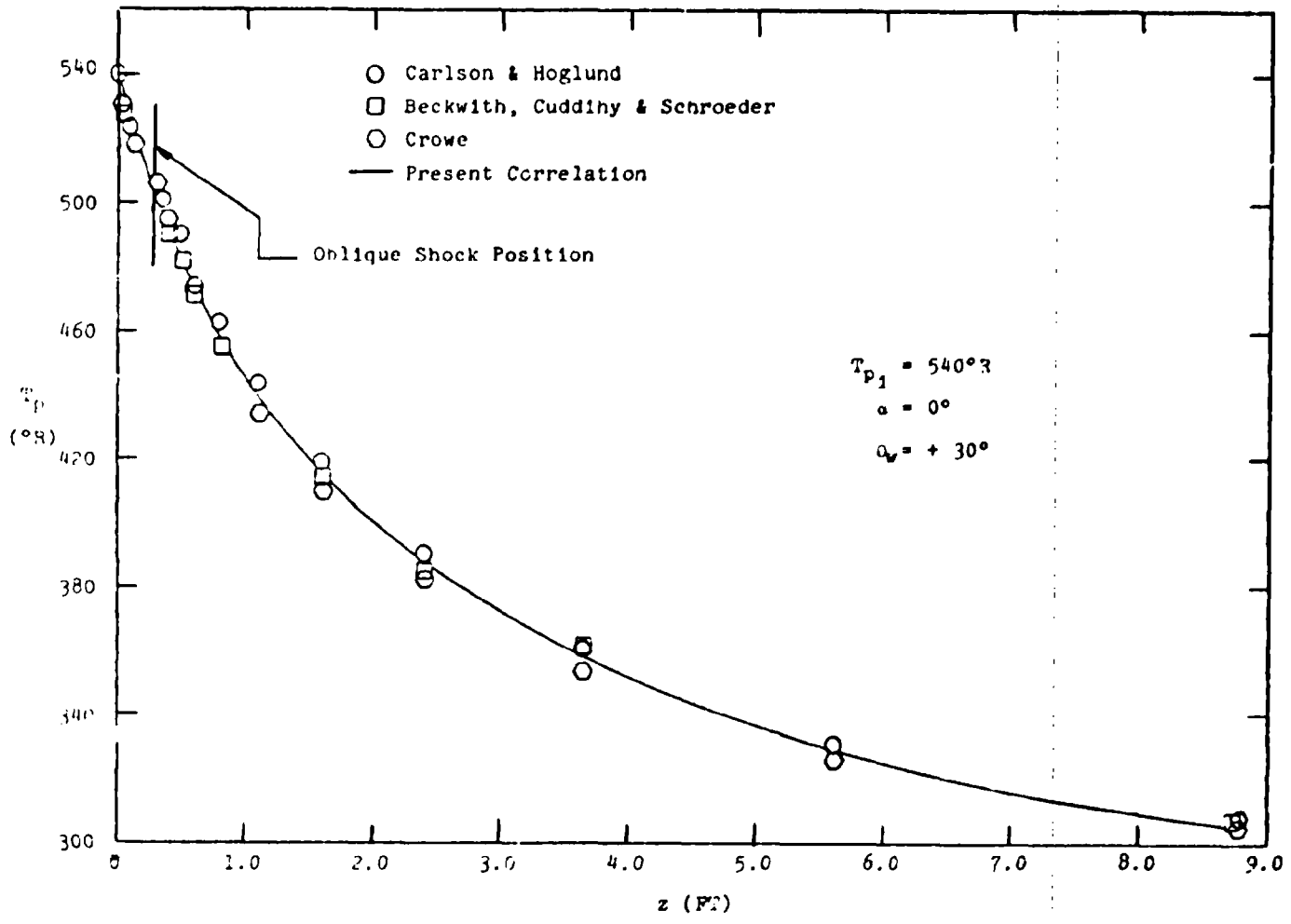

Figure 28. Particle Temperature History Through an Oblique Shock in Air for Different Drag Coefficient Correlations (r_p = 5 μm, u_{p_i} = 100 ft/s).

a supersonic stream. This solution yields the flow variables and the particle trajectories at all points behind the shock.

To complete the solution for the finite wedge, the expansion of the flow about the shoulder of the wedge defined by the point (r_w, z_w) must be computed. To obtain this solution, the flow field variables must be specified as functions of r at the initial axial location, z_w. These initial conditions are determined from the results of the two-dimensional infinite wedge solution. It should be noted that the Prandtl-Meyer expansion cannot be used in its general form for the flow over the shoulder of the wedge since theory predicts an expansion to an infinite Mach number and zero pressure. Physically, there is a free shear layer formed at the shoulder of the wedge which must be accounted for in the calculations to obtain the appropriate turning angle of the flow. In the present computer program, the flow conditions behind the wedge are specified with a base pressure correlation[14] for flows over two-dimensional bodies. From this correlation the base pressure behind the wedge can be calculated for a given free stream Mach number, and from this base pressure the proper turning for the flow can be calculated.

The results of the application of this procedure to a two-dimensional 10° half-angle wedge for a 2 μm diameter titanium dioxide particle are shown in Figure 29. The following free stream conditions were used:

P_∞ = 7920 PSF	u_{p_i} = 100 ft/s
T_∞ = 540°R	T_{p_i} = 540°R
γ = 1.4	α_{p_i} = 0°
M_∞ = 2.0	

and results in the particle trajectories shown in Figure 29. The velocities and temperature variation for two particle trajectories are shown in Figures 30 and 31. In addition, the mass flux density profiles at three axial locations in the flow field are shown in Figure 32 and tend to emphasize the focusing effect when a body of this type is placed into a supersonic two-phase flow. Hence, it is possible to predict the entire two-phase flow field about a body of arbitrary symmetry placed into a supersonic stream since the flow field can be constructed from the uniform flow, Prandtl-Meyer expansion fan, and oblique shock flow cases.

E. EFFECT OF DIFFERENT GASES ON TWO-PHASE FLOW CHARACTERISTICS

Investigations were conducted to determine if any significant difference results for particles injected into a gas different from air. A uniform flow was examined for the following gas conditions:

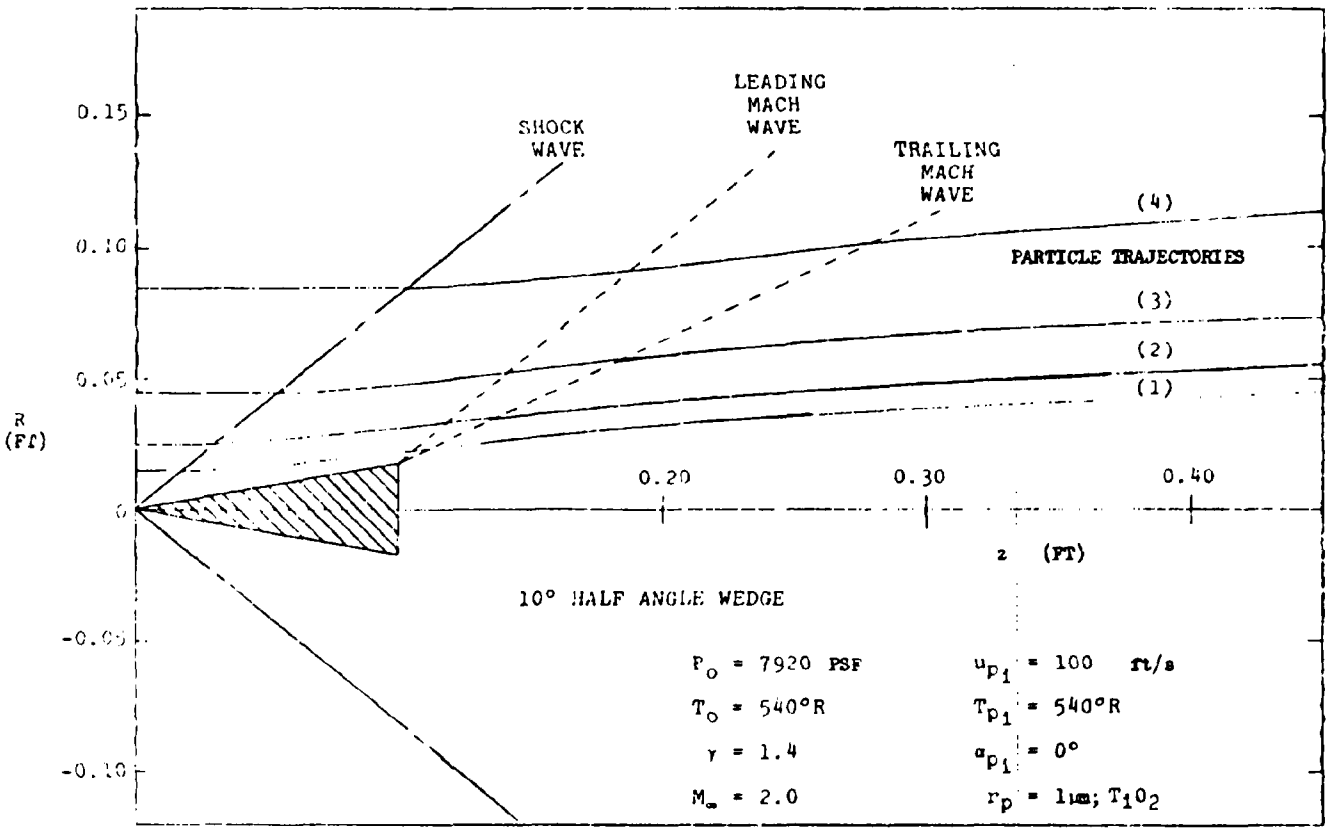

Figure 29. Two-Phase Flow Field and Associated Particle Trajectories About a 10° Half-Angle Wedge.

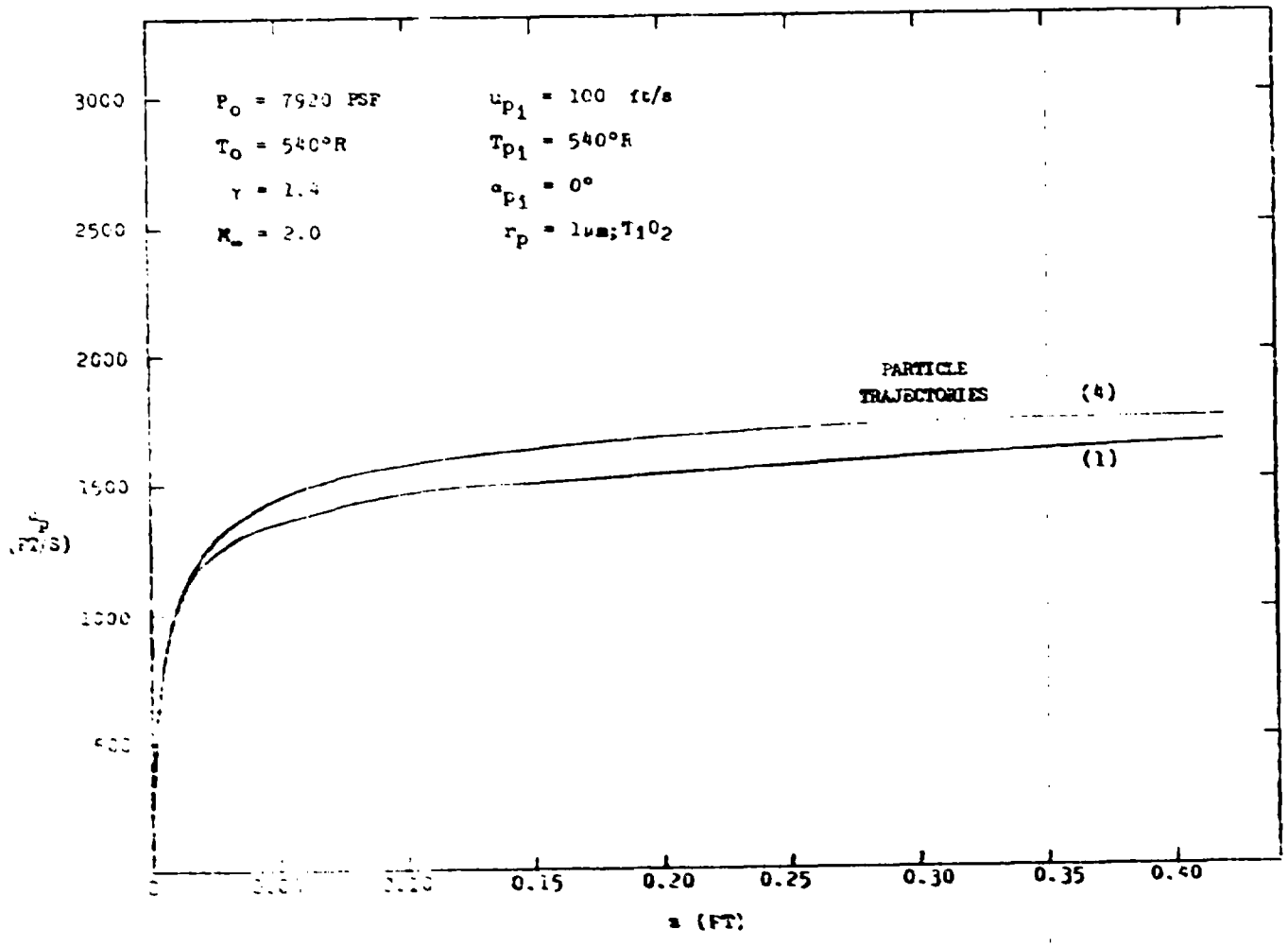

Figure 30. Particle Velocity History on Particle Trajectories (1) and (4) in Two-Phase Flow Field About a 10° Half-Angle Wedge.

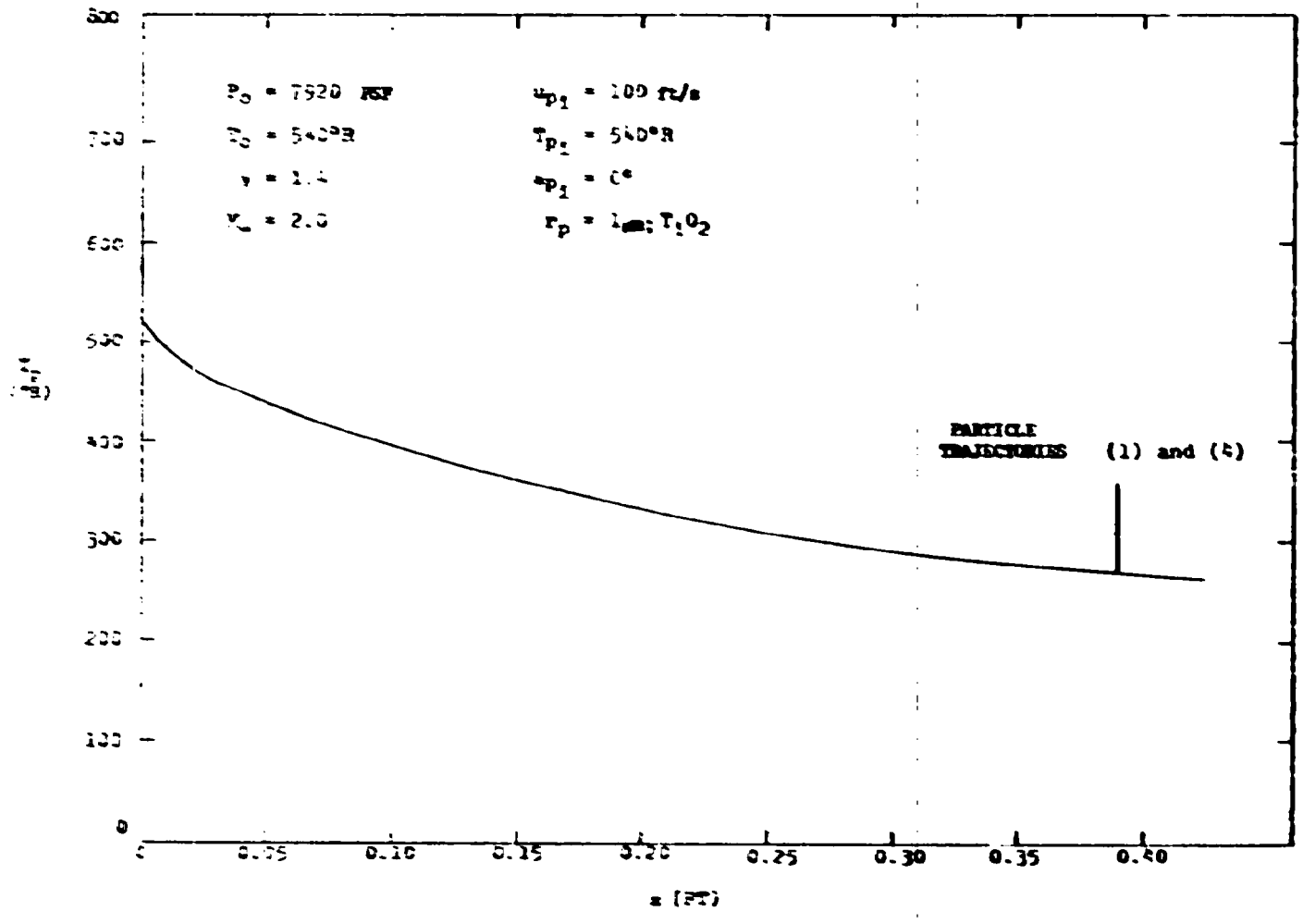

Figure 31. Particle Temperature History on Particle Trajectories (1) and (4) in Two-Phase Flow Field About a 10° Half-Angle Wedge.

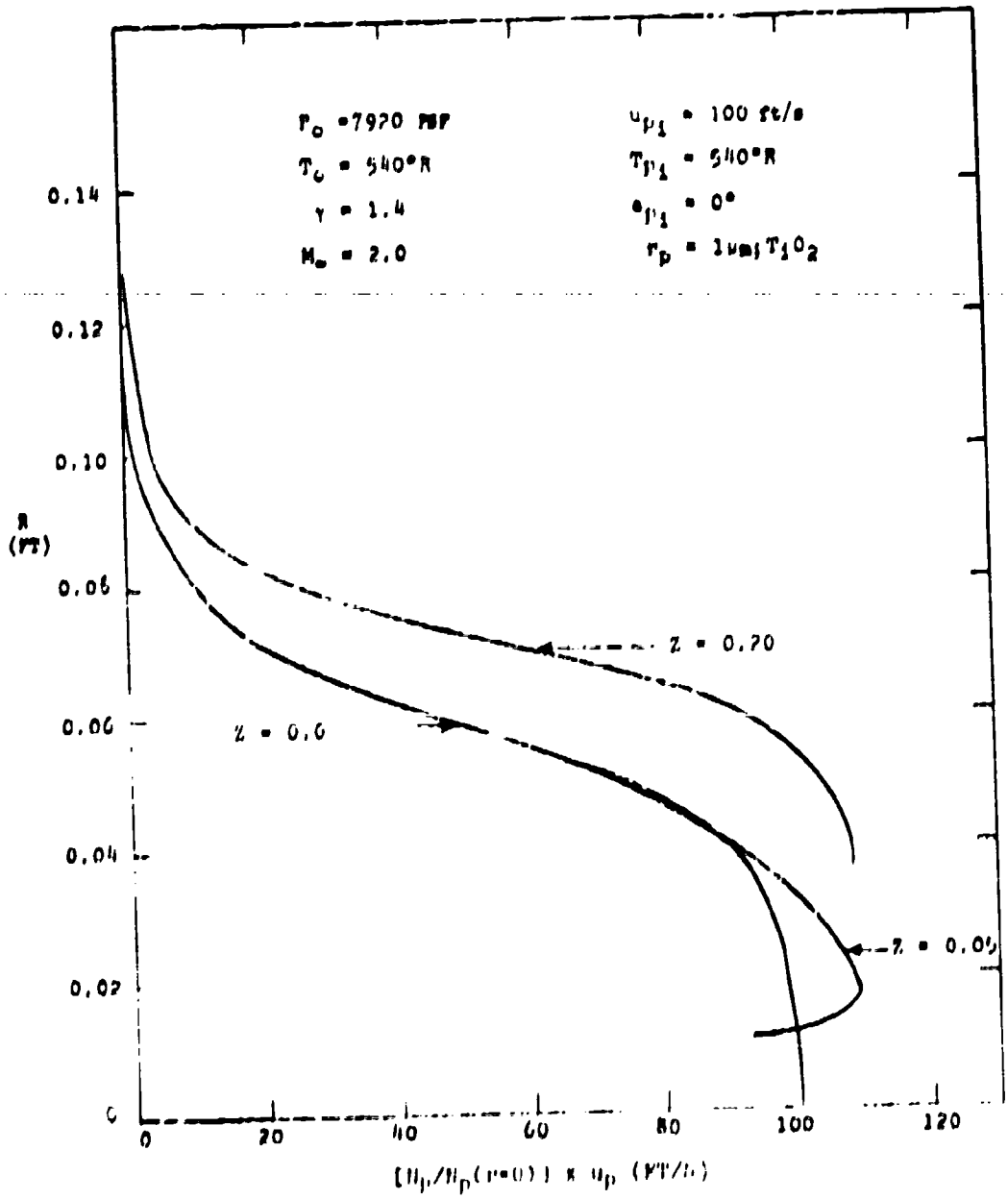

Figure 32. Mass Flux Density Profiles at Three Axial Locations in Two-Phase Flow Field About a 10° Half-Angle Wedge.

$M_\infty = 5.0$

$P_0 = 7876.8$ PSF

$T_0 = 540°R$

$\vartheta_g = 0°$

The particles were assumed to be titanium dioxide with a diameter of 10 μm, injected at an angle of 45° with an initial velocity of 100 ft/s and an initial temperature of 540°R. The particle trajectories shown in Figure 33 correspond to particle injection into helium, air, and argon. As can be seen, the radial coordinate is directly proportional to the molecular weight and there is a direct viscosity effect. The gas viscosity was assumed proportional to the molecular weight of the gas.[1]

Since the Mach number was specified, the gas velocities for the three cases investigated were different. The ratio of particle velocity to gas velocity is shown in Figure 34. Again, there is a definite relationship between the magnitude of u_p/u_g and the molecular weight. These results indicate that u_p/u_g approaches unity quicker for the larger molecular weight gas. This is significant when considering the momentum of the particle available for transfer. In contrast to these results, the ratio of particle temperature to gas temperature was used to evaluate the effect of different gases on the energy exchange process. The results are shown in Figure 35. There is little difference between results for argon and air; however, T_p/T_g is larger for helium than it is for both argon and air.

F. EFFECT OF DIFFERENT PARTICLES ON TWO-PHASE FLOW CHARACTERISTICS

In this phase of the study, the flow situation described in the previous section was adopted for air and the type of particle was varied; i.e., TiO_2, MgO, and Al_2O_3 particles were used. The characteristics of these particles are:

Particle	Molecular Weight	Density (slugs/ft³)	Specific Heat Capacity (ft²/s²-°R)
TiO_2	79.90	8.6	7564
MgO	40.32	10.3	9080
Al_2O_3	101.96	7.7	8100

The resulting particle trajectories are shown in Figure 36 and indicate there is no significant difference even though there is a large difference in the molecular weights. This is also true for particle velocities and temperatures, as shown in Figures 37 and 38. The conclusion

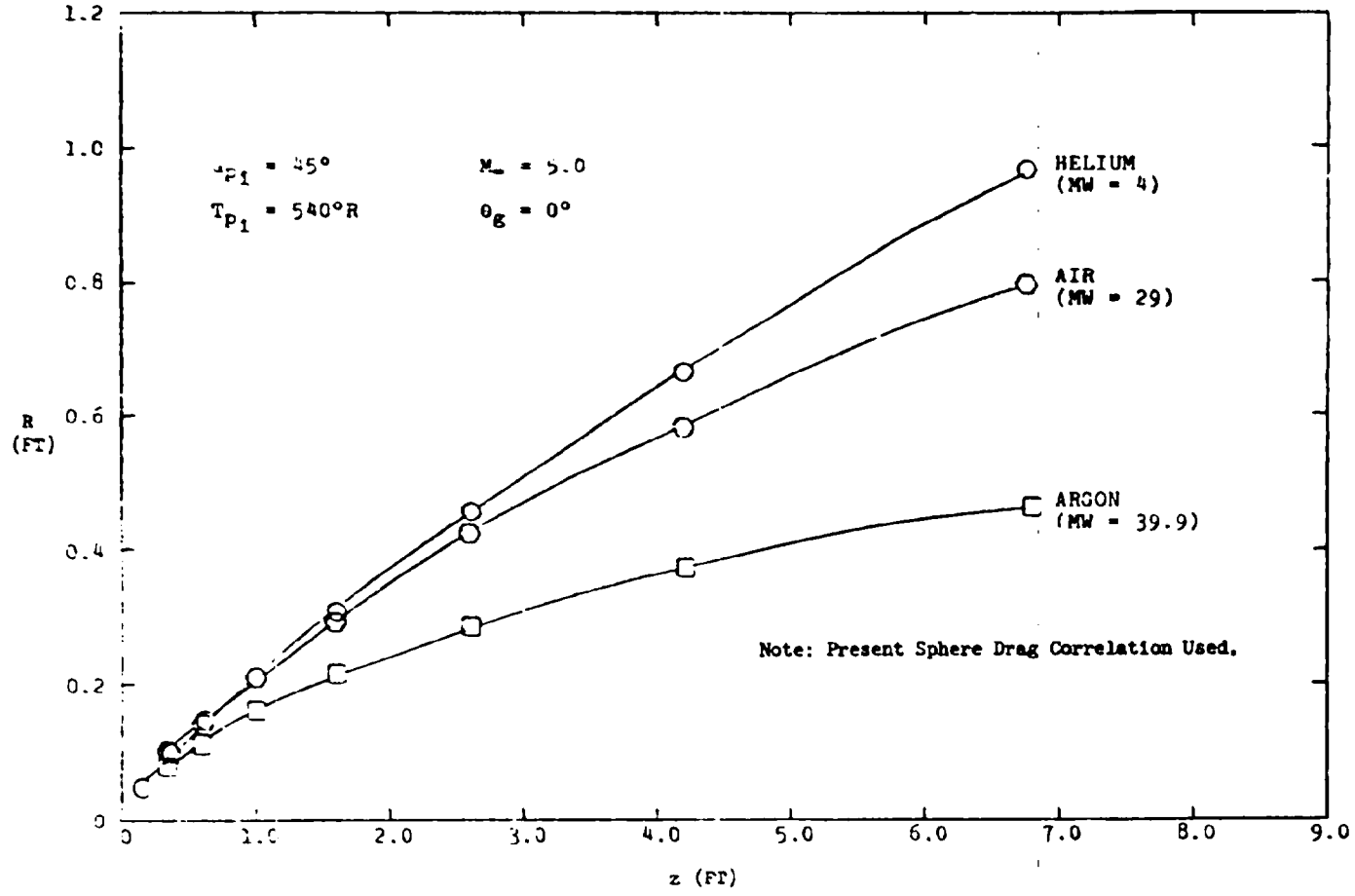

Figure 33. Trajectory of Particle in Different Gases for Uniform Flow Case (r_p = 5 μm, u_{p_i} = 100 ft/s.

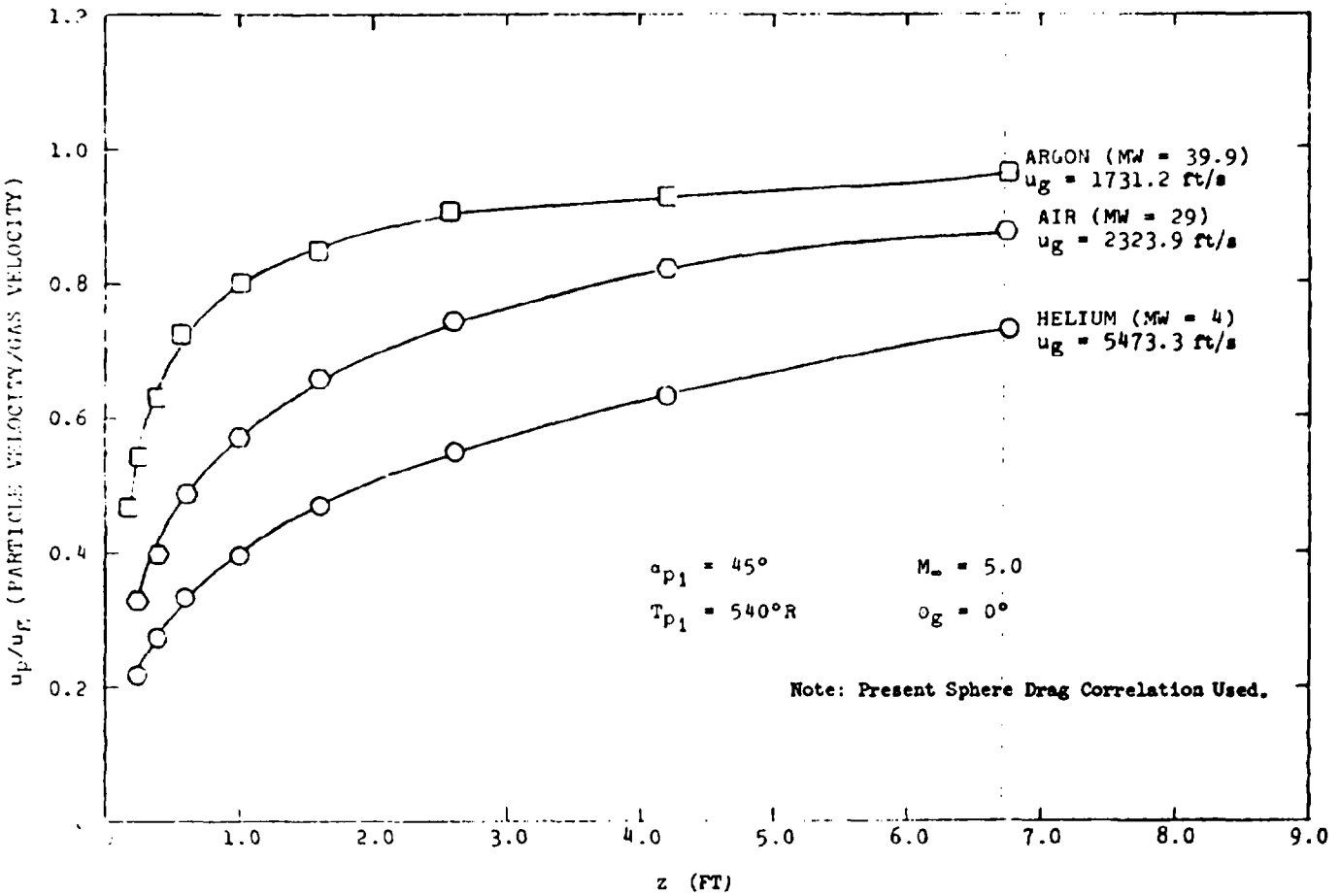

Figure 34. Particle Velocity History in Different Gases for Uniform Flow Case (r_p = 5 μm, u_{p_i} = 100 ft/s).

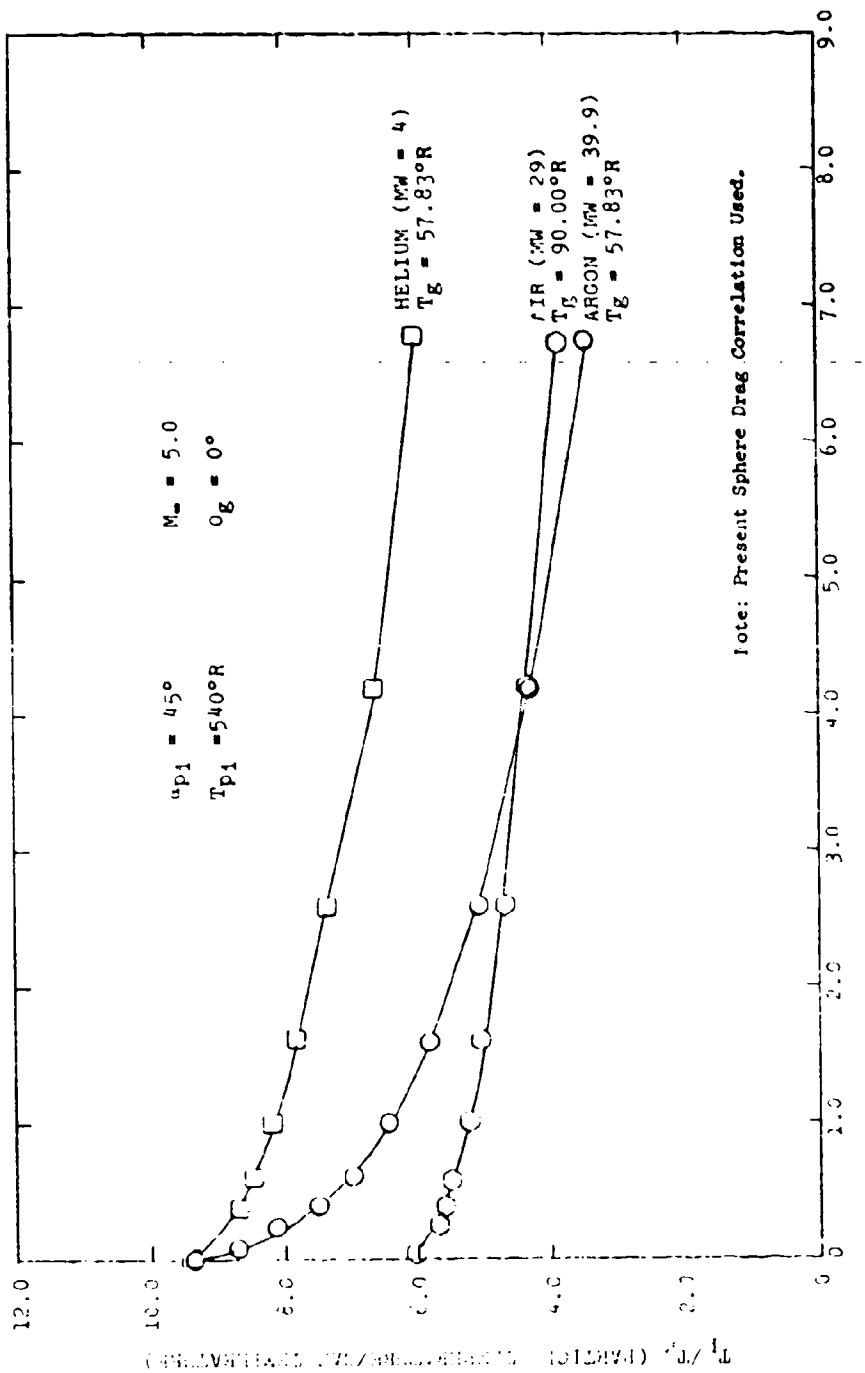

Figure 35. Particle Temperature History in Different Gases for Uniform Flow Case (r_p = 5 μm, u_{p_i} = 100 ft/s).

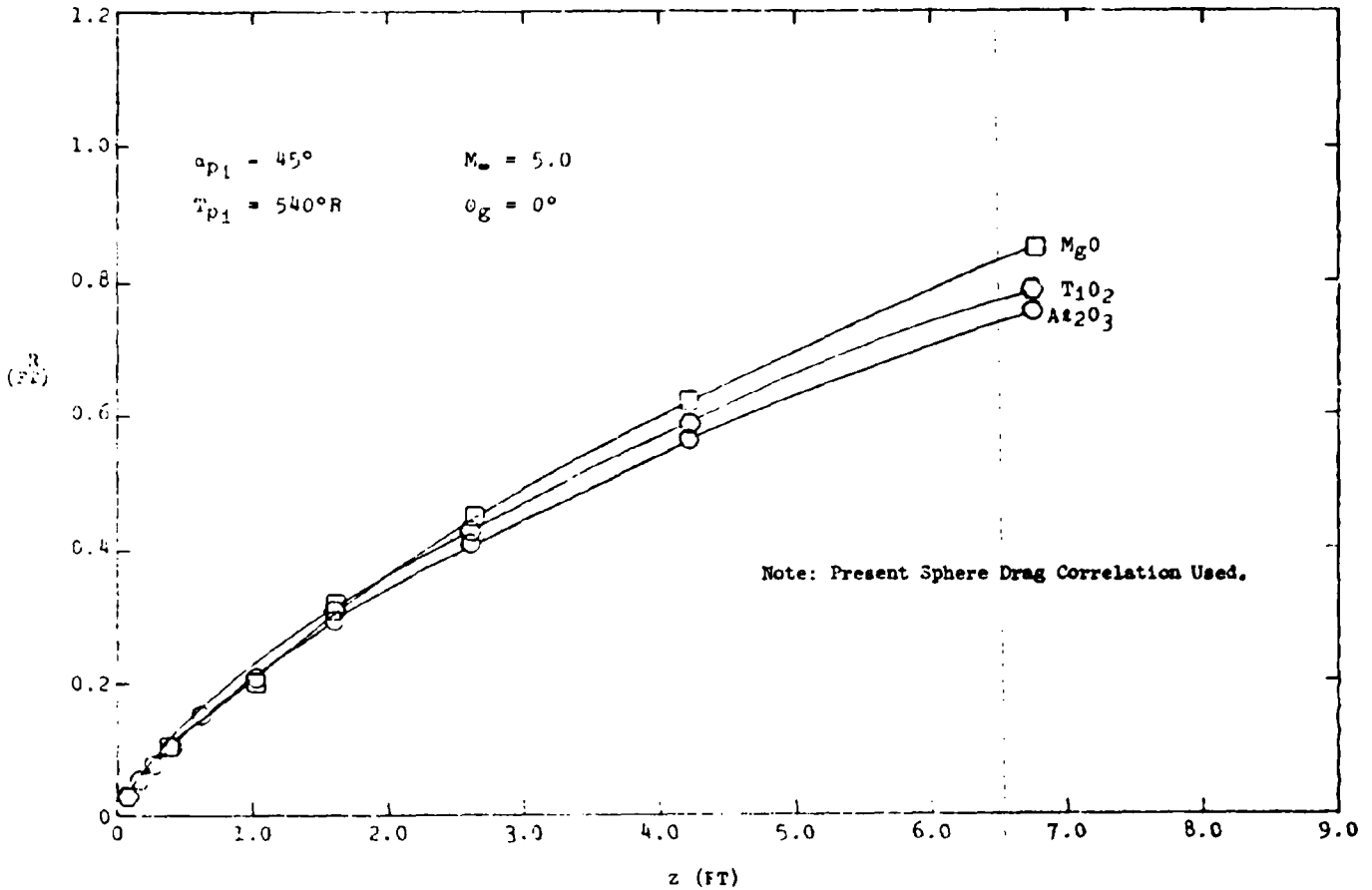

Figure 36. Trajectory of Particle in Air for Uniform Flow Case for Different Particles (r_p = 5 μm, u_{p_i} = 100 ft/s).

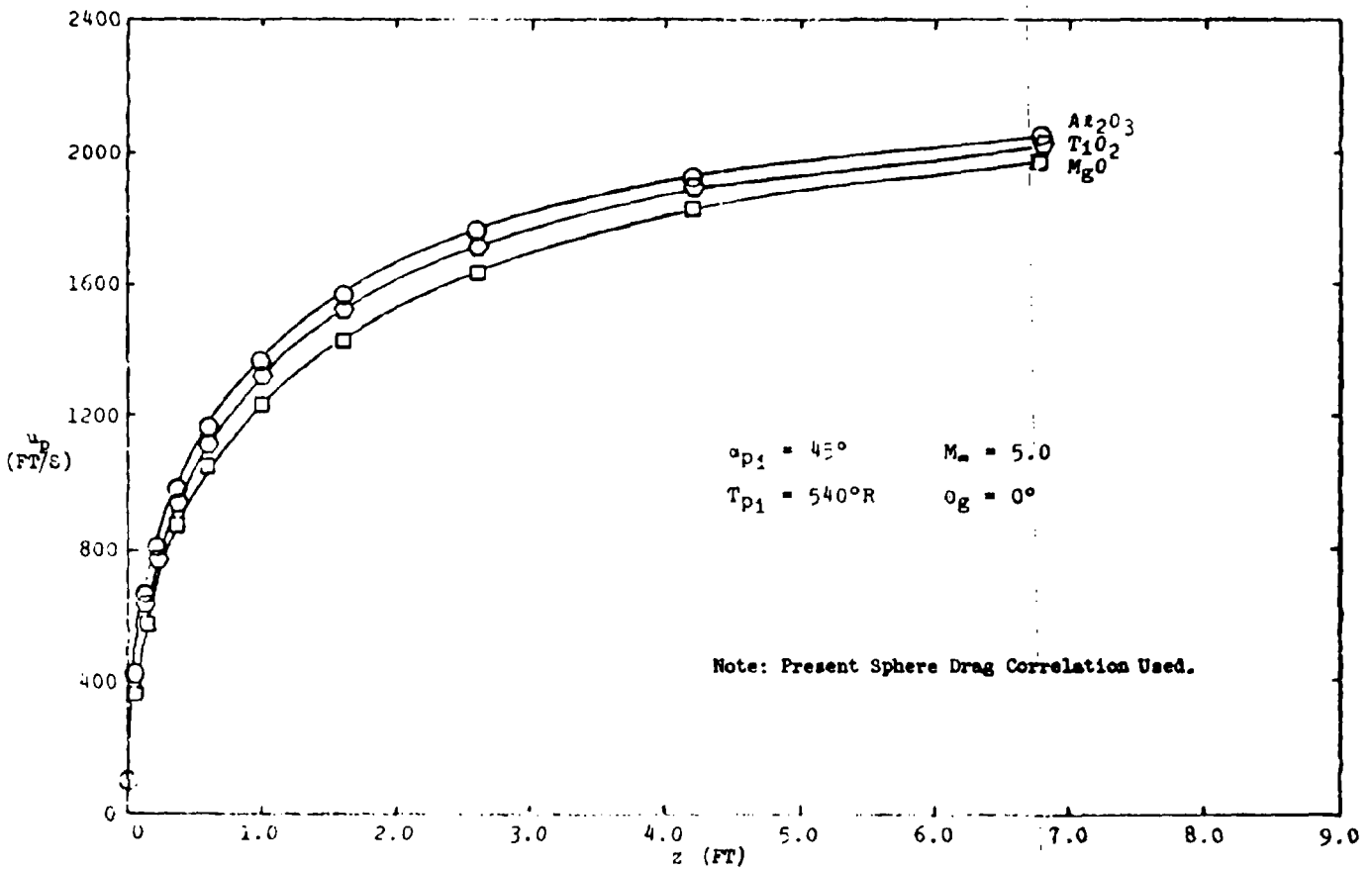

Figure 37. Particle Velocity History in Air for Uniform Flow Case for Different Particles (r_p = 5 μm, u_{p_i} = 100 ft/s).

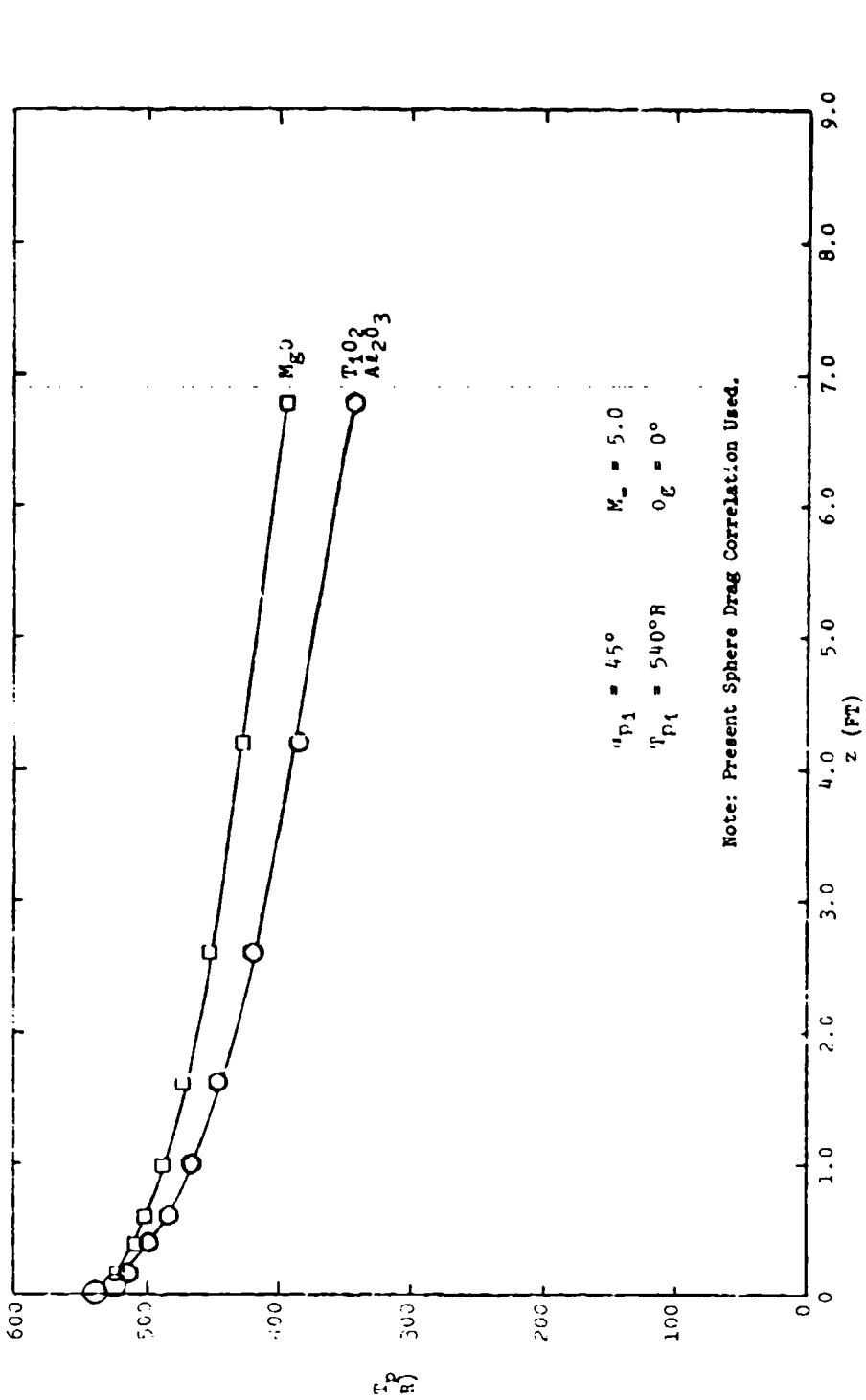

Figure 38. Particle Temperature History in Air for Uniform Flow Case for Different Particles (r_p = 5 μm, u_{p_1} = 100 ft/s).

can, therefore, be drawn that for the uniform flow situation, there is no significant difference in the two-phase flow characteristics for the range of particle molecular weights used.

SECTION III

TWO-PHASE FLOW EXPERIMENTAL STUDIES

An experimental study to examine wave patterns which lead to focusing of refractory particles was undertaken in this segment of the study. A special wind tunnel facility was assembled, and solid particles of known diameter and concentration were added to the nozzle flow as a first order simulation of the jet interaction region in a multi-component flow device. Bodies generating various wave systems were inserted into the two-phase flow field, and laser scattering techniques were employed for the determination of local particle concentration.

A. TEST FACILITIES

The experimental studies were conducted in a continuous flow wind tunnel system at the Aeronautical and Astronautical Research Laboratory. The wind tunnel employs an air storage system of 1500 ft^3 at 2650 psig and a two-stage ejector system located in the diffuser. The run times for the facility are limited only by the gas storage system. A schematic drawing of the facility is shown in Figure 39. It consists of a conical nozzle (exit diameter of 1.75 inches) with an exit air Mach number of 5 exhausting to an open jet test cabin. The measured pitot pressure profile for this facility taken at the nozzle exit plane is shown in Figure 40.

Particles were injected in the stagnation region of the facility with a fluidized bed system shown schematically in Figure 41. A helium supply was used to pressurize the particle container and thus fluidize the particles within the porous inner container. The particles were then injected into the tunnel by opening the on-off valve contained in the feed tube. The flow of particles was further regulated with a 0.090-inch orifice in the feed tube.

The particles were titanium dioxide, manufactured by Dow Chemical Company. A particle sample was analyzed with a Coulter-Counter Model T No. 1027 to obtain an accurate measurement of the particle size distribution. The results are shown in Figure 42 in terms of a particle size histogram, i.e., percent differential volume versus particle diameter. Percent differential volume is defined as the percent of the total volume occupied by the particles in a specific particle diameter range; e.g., approximately 24% of the volume is occupied by particles ranging between 0.8 and 1.0 μm in diameter. In addition to the TiO_2, the particle sample contained approximately 1% by weight of CAVASIL whose diameter was on the order of 0.1 μm. This material when added to the TiO_2 has a liquidizing effect, thereby increasing the flowing qualities of the powder. The particle histogram (Fig. 42) does not reflect this addition.

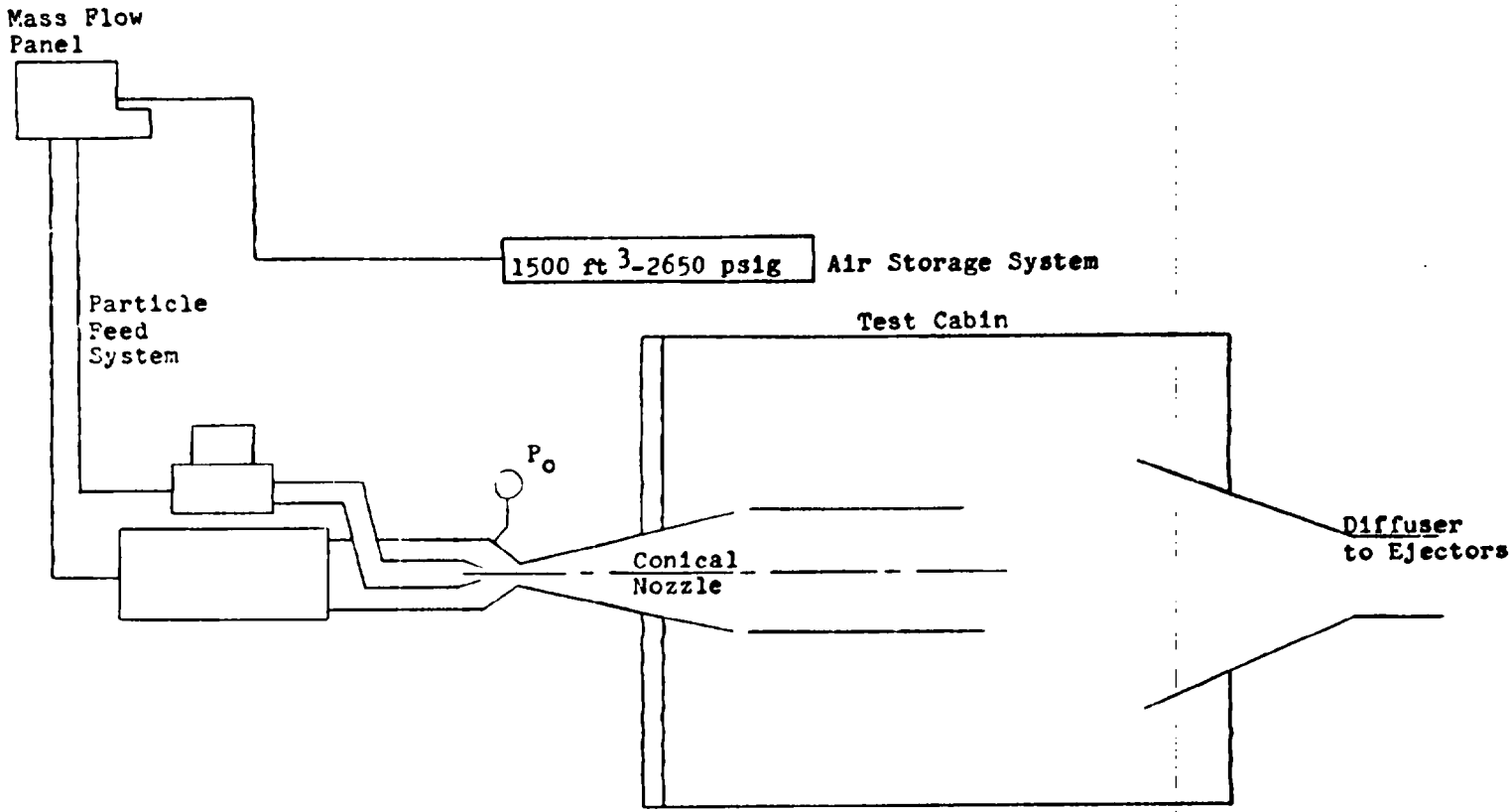

Figure 39. Particle Concentration by Wave Systems - Facility Schematic.

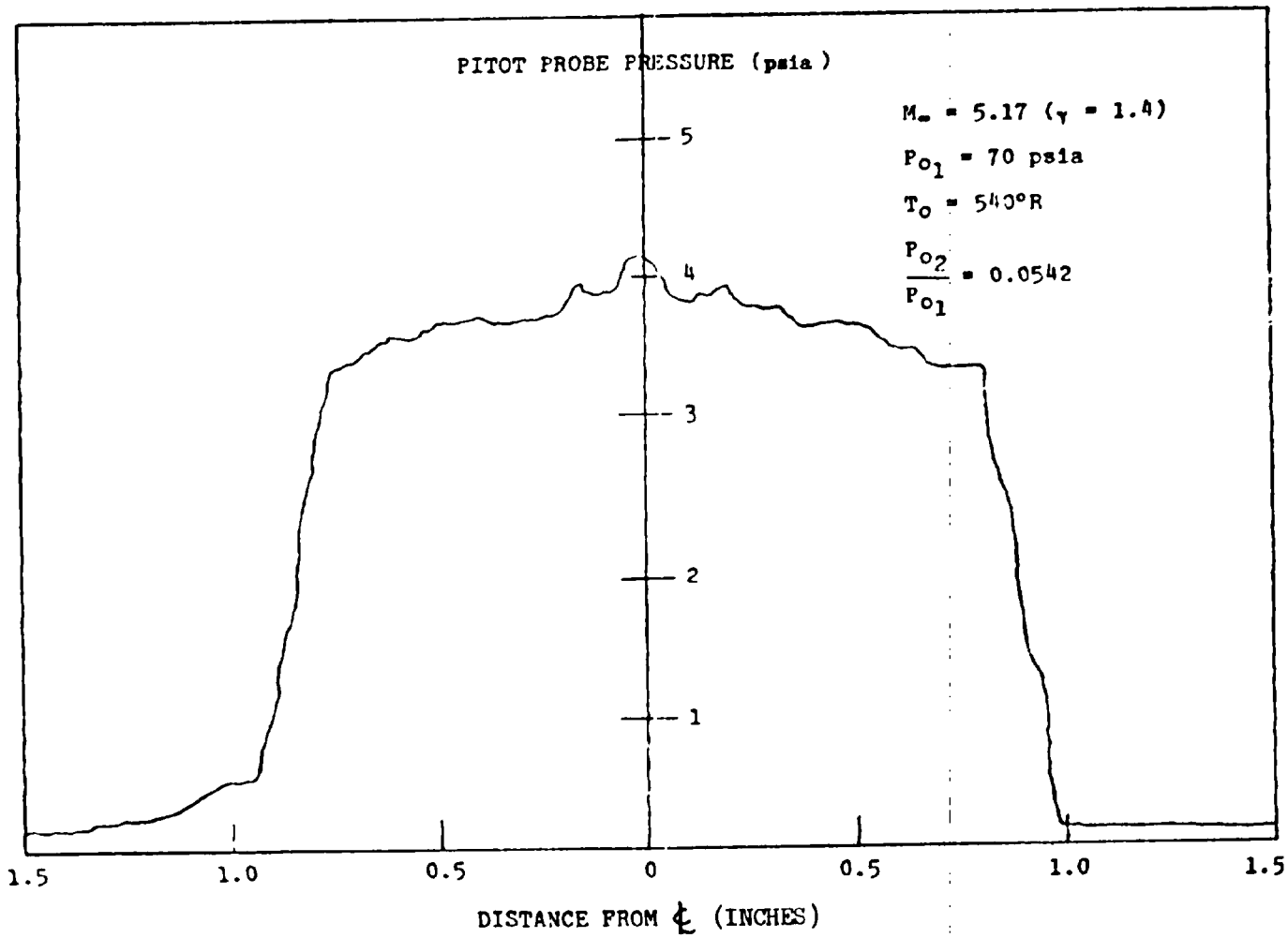

Figure 40. Measured Pitot Pressure Profile for Two-Phase Flow Tunnel (No Particles).

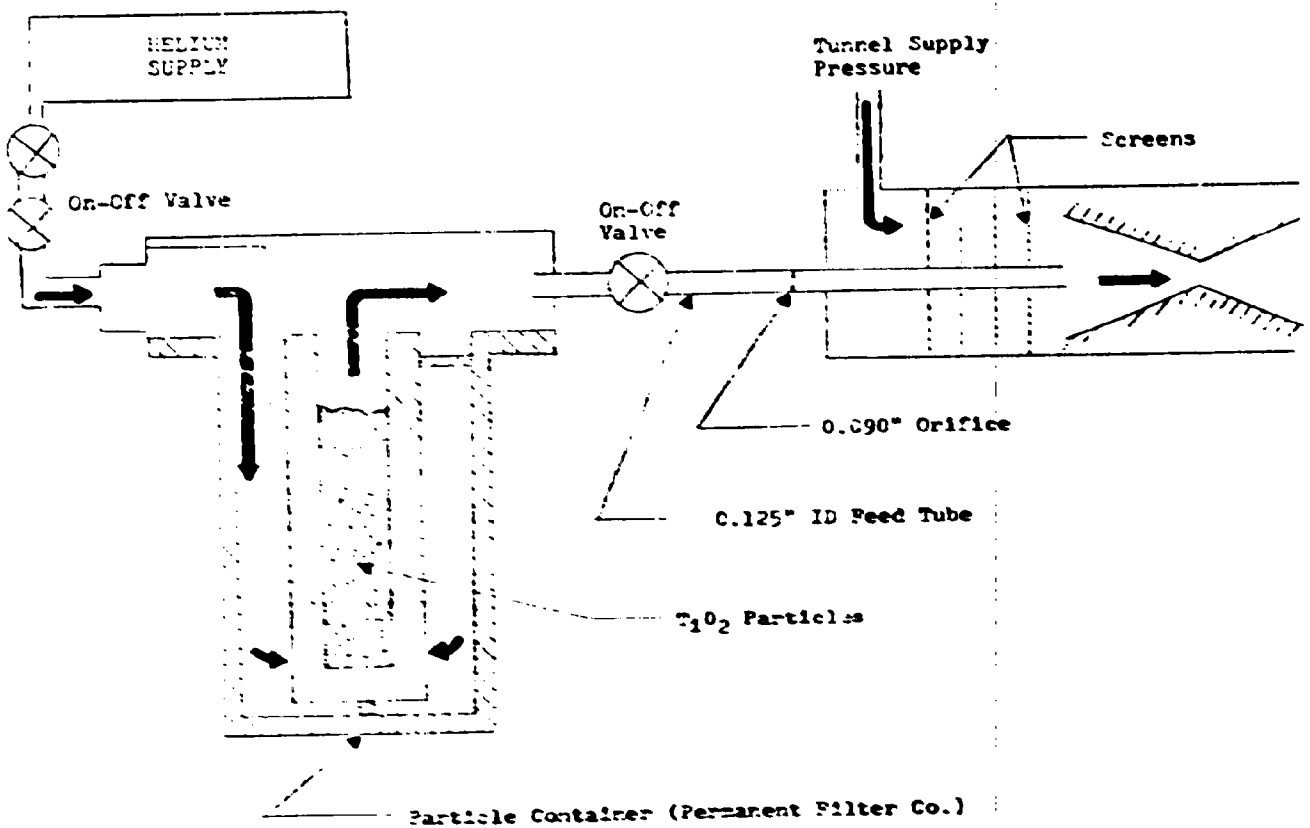

Figure 41. Schematic of Particle Feed System.

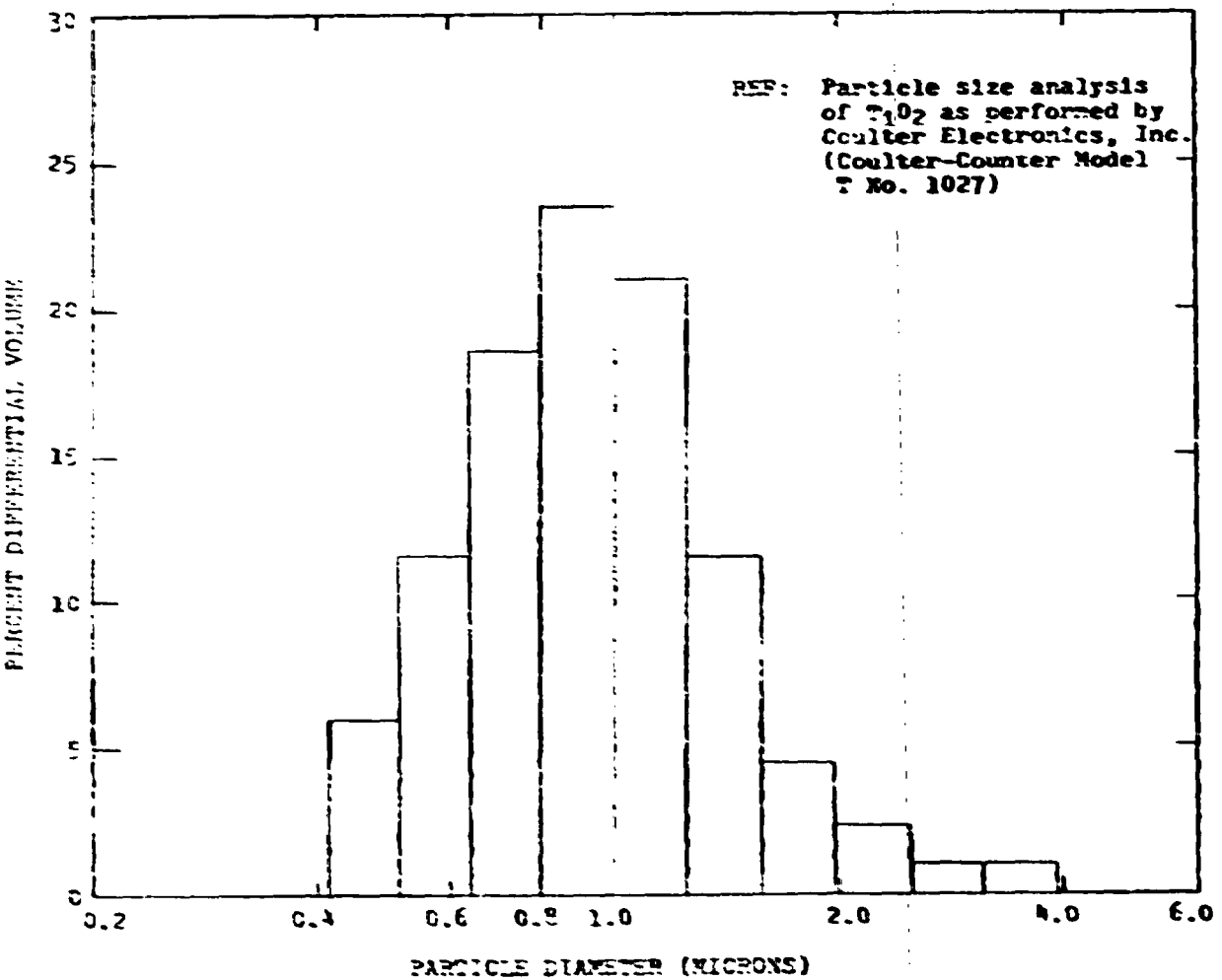

Figure 42. Particle Size Histogram of Titanium Dioxide Powder Used in Experimental Study.

B. MODELS

Various wedge models were inserted into the two-phase flow to determine the effect of the geometry and associated wave system on the particle concentration profiles. Wedges, 5 and 15°, spanning the entire nozzle exit plane with base dimensions of 0.088 and 0.262 inch, respectively, were used. The models were set at 0, 2.5, 7.5, and 10° angles of attack.

C. INSTRUMENTATION

Various particle concentration measurements techniques have been developed, primarily for use in rocket motors. These include spectroscopic and recovery tank methods,[1-7] mass sample probes used with mass spectrometers[8] and chromotographs,[9,10] and photographic observation techniques.[11] However, these methods either perturb the flow field because of the presence of a sampling probe or give integrated results across the flow field. It is also unlikely that the gas sampling methods will yield reliable measurements of particle concentration.

Recently, laser scattering techniques have been developed for the measurement of particle concentrations. In these techniques, a laser beam is projected across the flow field, and scattering of the photons by solid particles result. Typical applications of the technique can be found in the literature.[12-15] The type of laser scattering which results depends upon the ratio of the particle size to wavelength of the laser light. When the particle size compared to the wavelength is small, Rayleigh scattering results. The work of Daum and Farrell[16] for the detection of air condensation in hypersonic wind tunnel is typical of the application of Rayleigh scattering. However, when solid particles are present in the flow field, scattering results with a cross-section considerably larger than that for the Rayleigh scattering; therefore, the severe requirements placed on the scattering detection are alleviated when solid particles are responsible for the laser scattering.

Laser scattering techniques were employed in the present study for the measurement of particle concentrations. The instrumentation schematic for this system is shown in Figure 43. A 3 MW helium-neon laser was used and the scattered radiation was measured with a photomultiplier. This system gives accurate measurements of local particle concentrations at selected points within the two-phase flow field. Since the laser beam is relatively unaffected by the flow field, good spatial resolution in the measurements is obtained.

Particle concentrations were mapped by sending the beam from the laser through the test cabin and measuring the scattered light intensity. Scans were made along the laser beam and intensity versus distance

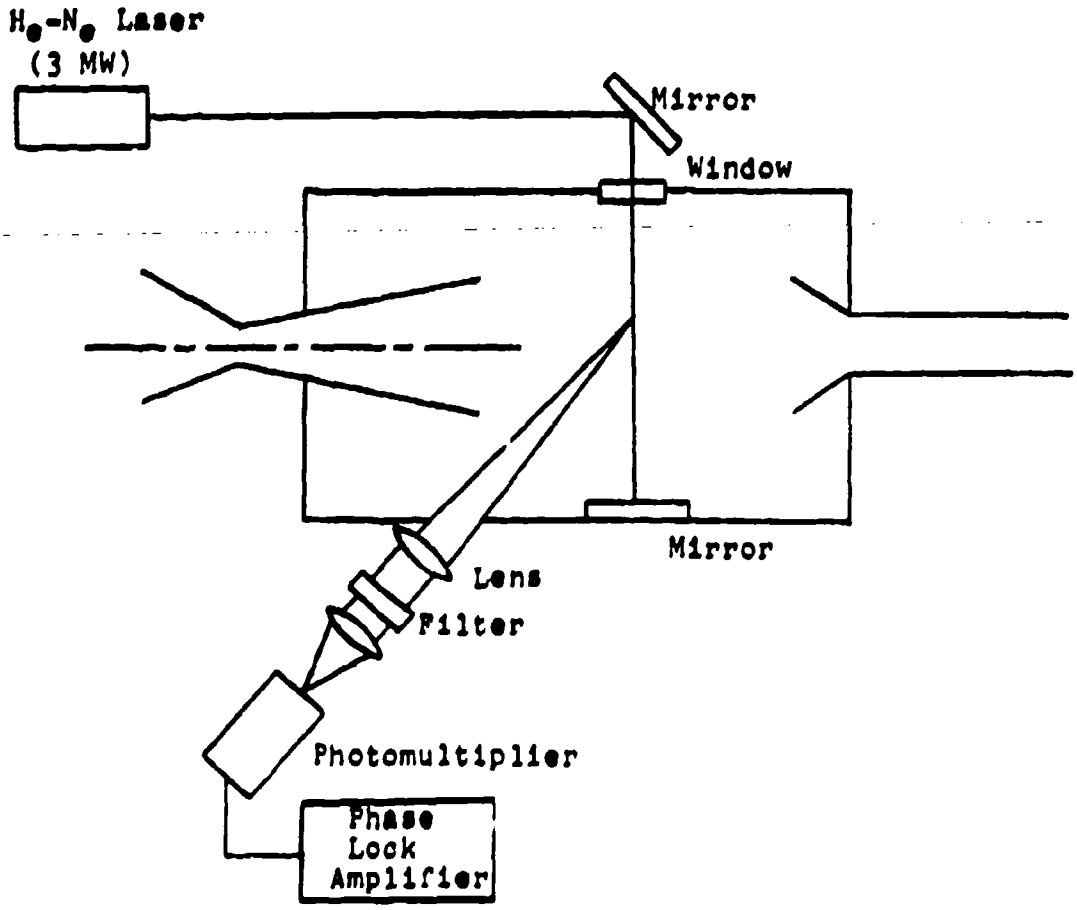

Figure 43. Laser Scattering Instrumentation Schematic.

profiles were obtained. The output from the spectrometer was amplified and processed by an analog computer and recorded on an X-Y plotter.

D. RESULTS AND DISCUSSION

A study was first conducted to determine the characteristics of the two-phase flow with the present injector scheme. The spectrometer was fixed at the geometrical centerline of the facility, and the particles were injected into the flow. The recorded intensity magnitude as a function of time is shown in Figure 44 and indicates that there is an approximate three-second segment in which the flow of particles is essentially constant. With the present physical arrangement, it appears that the 0.090-inch orifice is effective only during this time span. However, since the filter used in this study contains only a small quantity of particles which are injected through a fluidized bed, Figure 44 may indicate the result of a decreasing number of particles available for injection. This conclusion is verified by the data of Figure 45, where the percent decrease in intensity magnitude was measured at a fixed location as the valve was opened and closed a number of times without refilling the particle cylinder. The results show that the fluidized bed must be refilled for each measurement to obtain consistent data.

1. Basic Particle Concentration Profile

A typical nondimensional intensity profile is shown in Figure 46. The particle concentration profile is strongly peaked on the tunnel centerline when no wave systems are present to deflect the particles. The corresponding photographs taken in the facility are shown in Figures 47, 48, and 49.

2. Particle Concentration Profiles Behind Wedges

Particle concentration profiles downstream of various aerodynamic shapes have been investigated with the laser scattering technique. Photographs of the scattered laser light downstream of a 5 and 15° wedge at angles of attack of 0, 2.5, 7.5, and 10° are shown in Figures 50 through 55. The variation in intensity of the scattered light is clearly evident and reflects the variations of local particle concentration downstream of the wedge. These results indicate the focusing effect that can be obtained by placing an aerodynamic shape and its associated wave system into a two-phase flow.

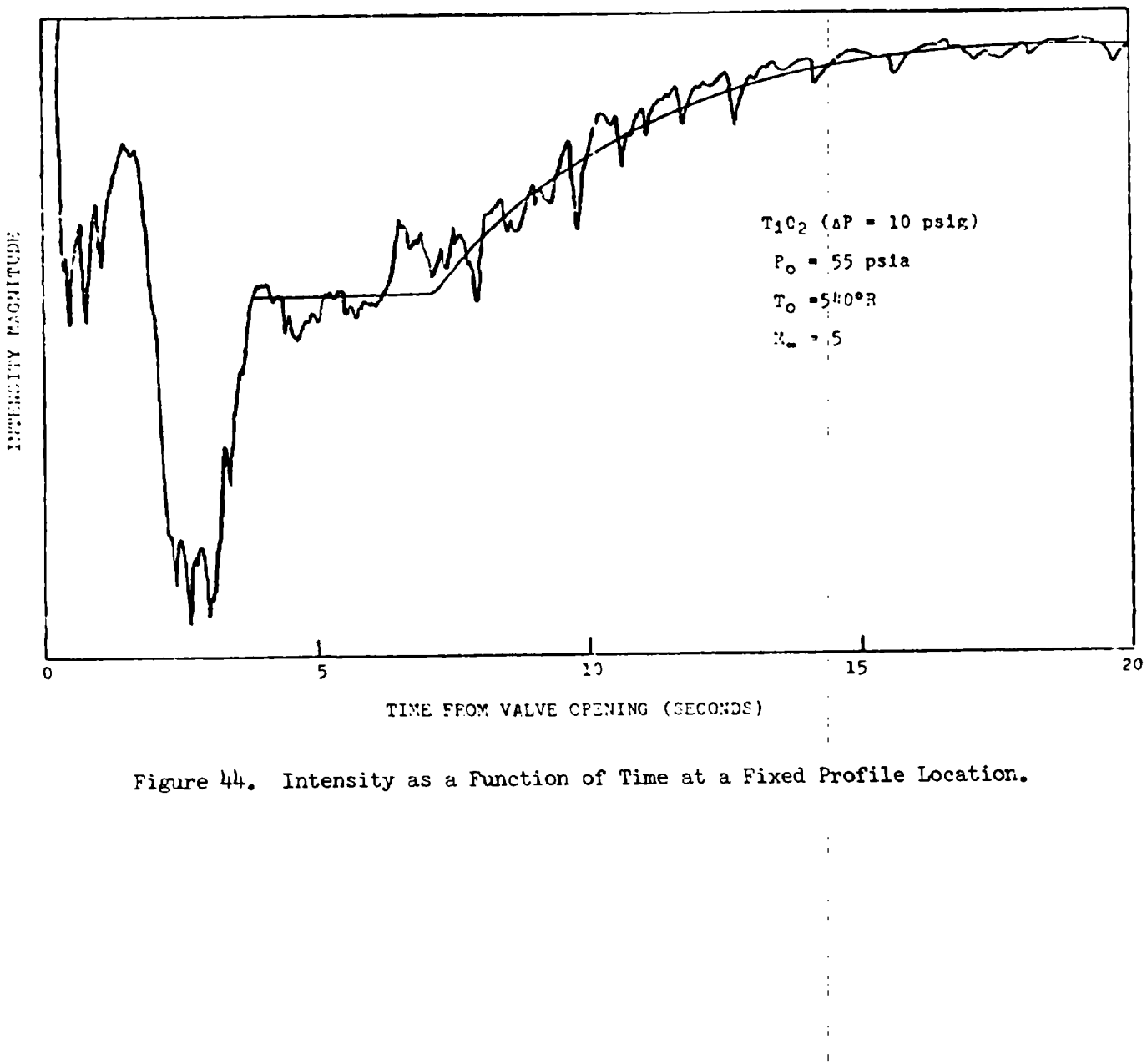

Figure 44. Intensity as a Function of Time at a Fixed Profile Location.

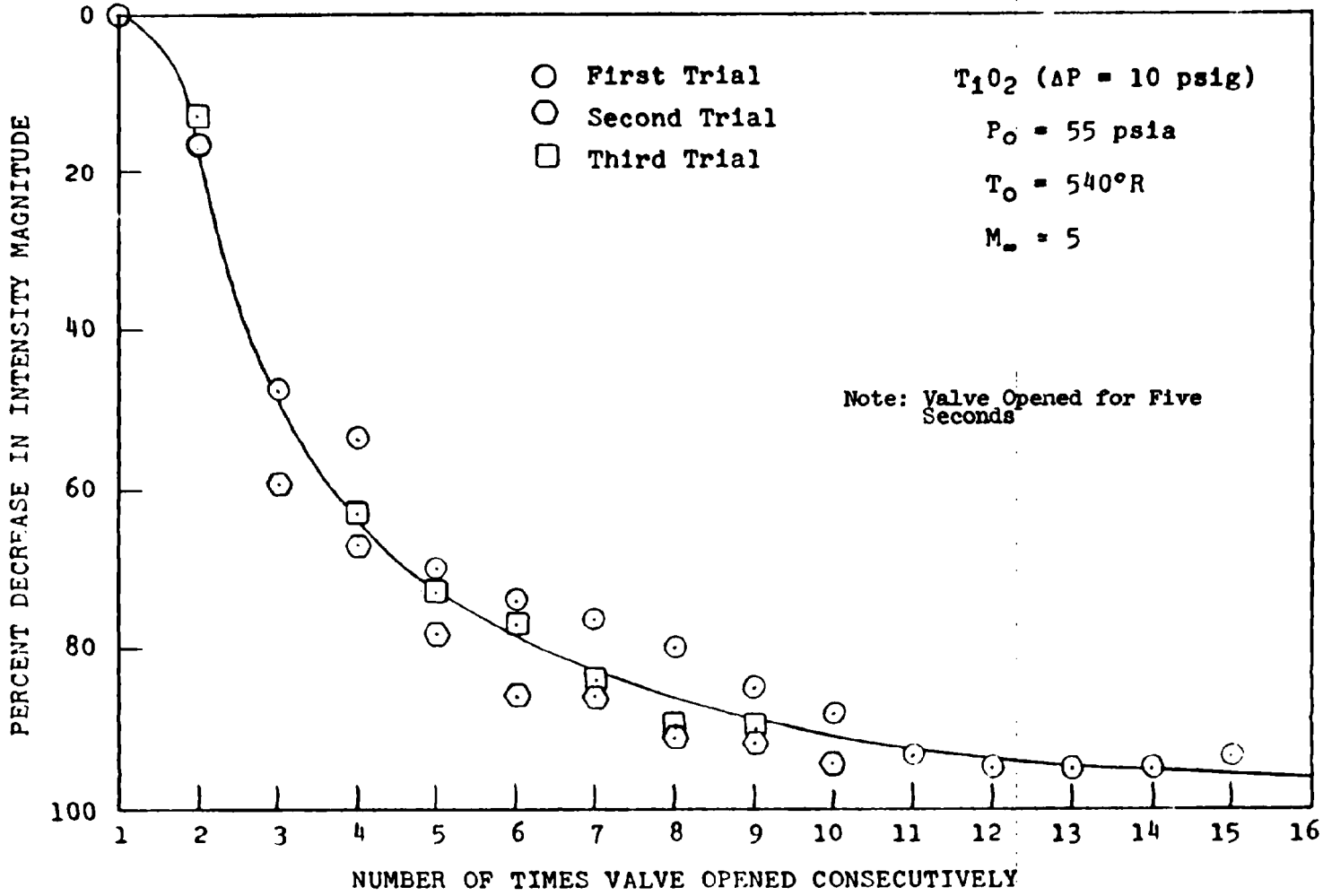

Figure 45. Relationship Between Valve Openings and Dust Introduced into Tunnel.

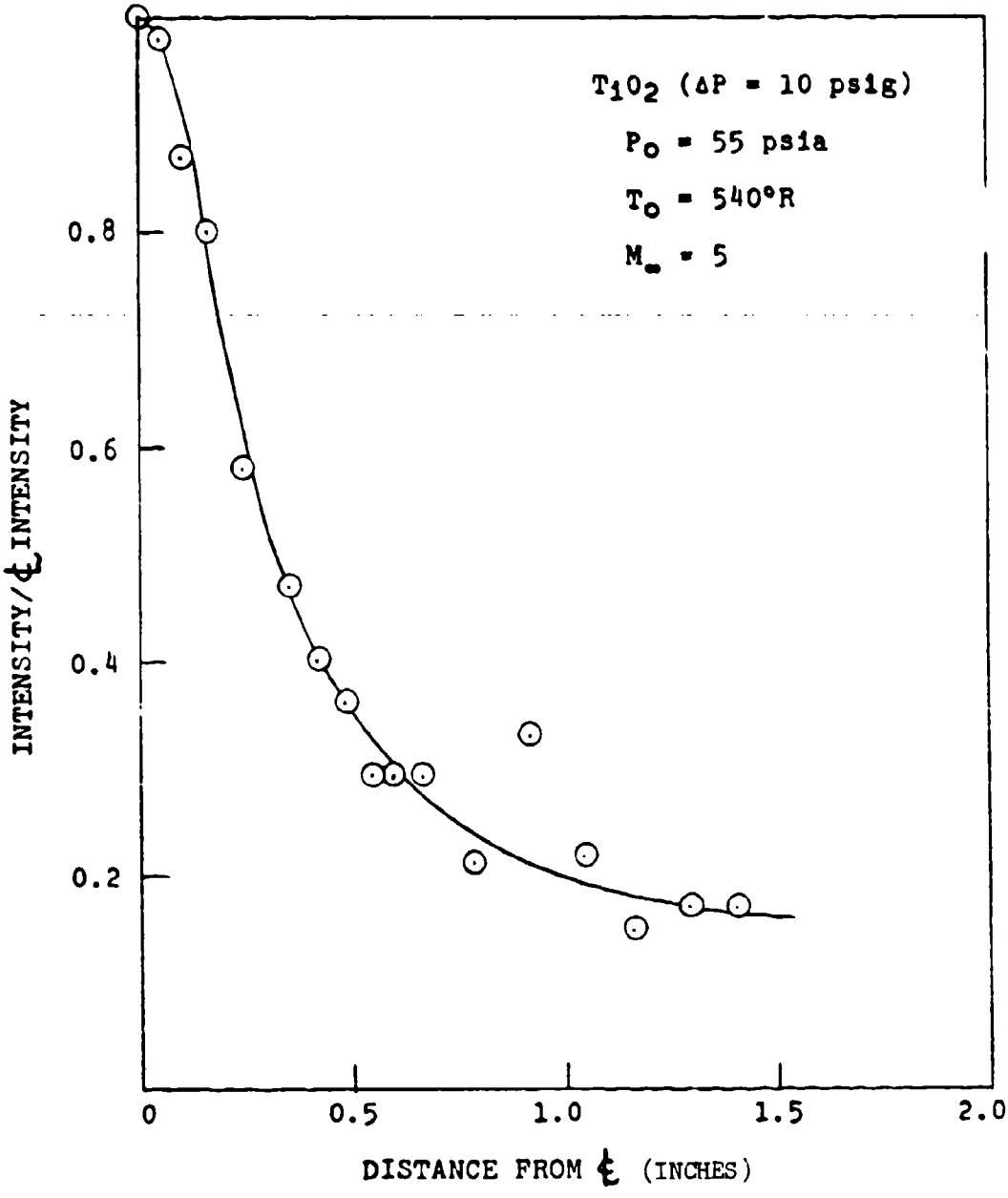

Figure 46. Nondimensional Intensity Profile as Function of Distance from $\mathcal{L}$ of Tunnel.

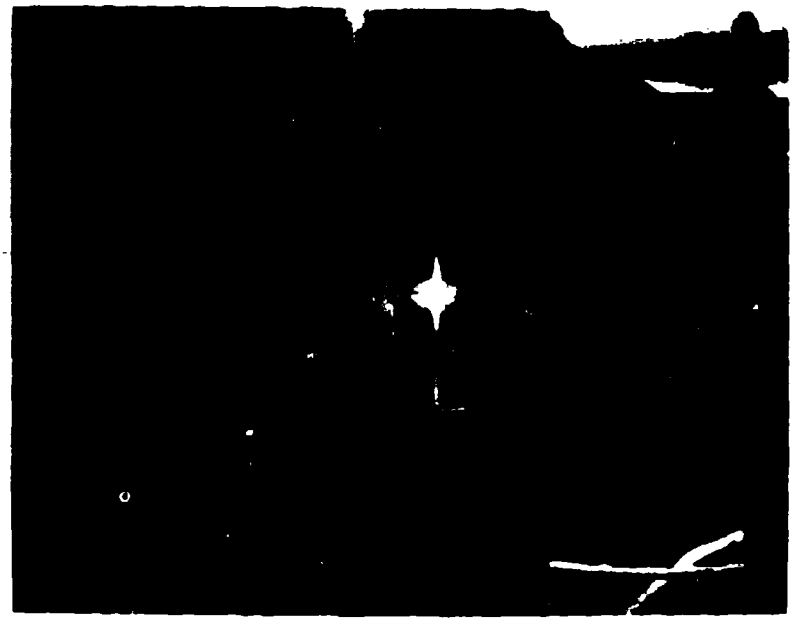

Figure 47. Profile of Titanium Dioxide Particles Due to Scattered Light - No Model Inserted.

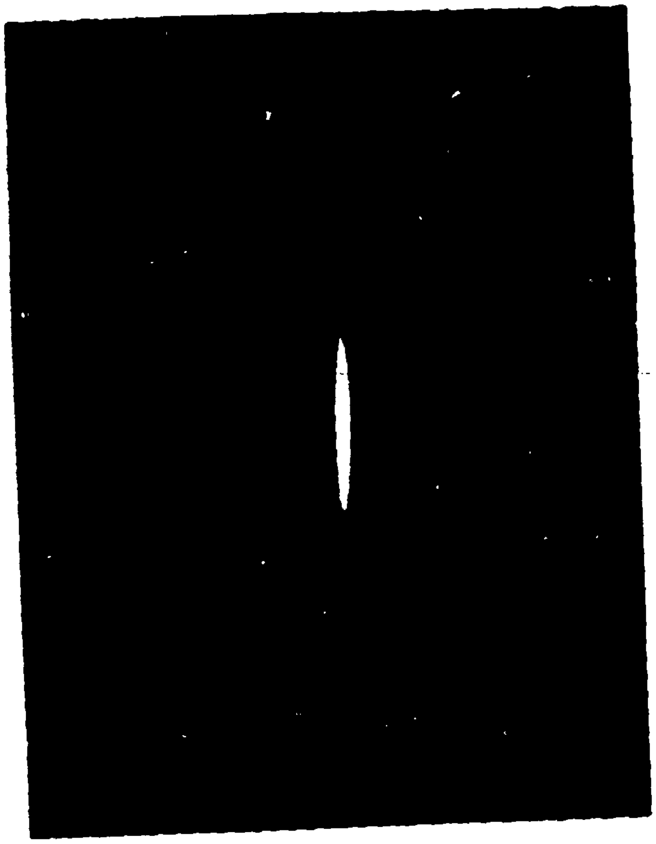

Figure [illegible]. Profile of Titanium Dioxide Particles Due to Scattered Light - No Towel Inserted.

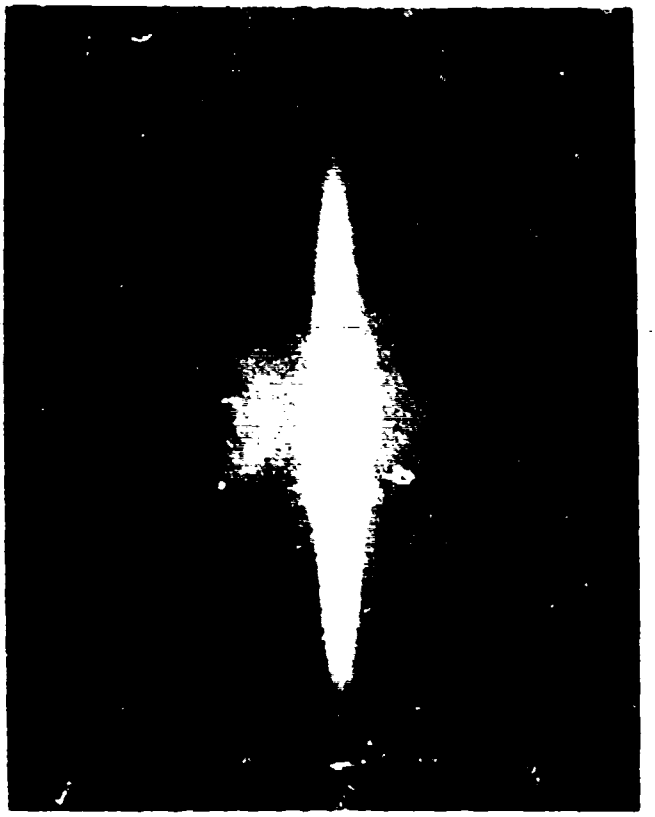

Figure 49. Profile of Titanium Dioxide Particles Due to Scattered Light - No Model Inserted.

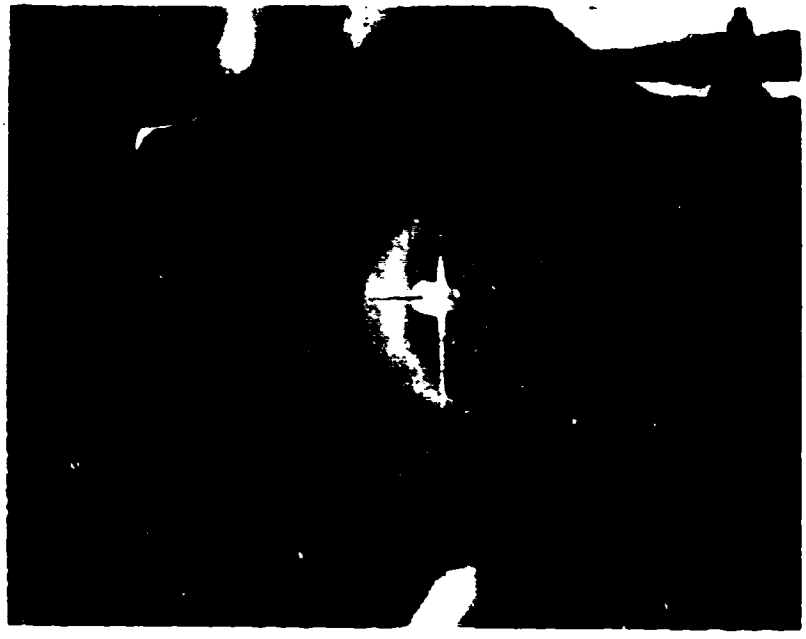

Figure [illegible]. Profile of Titanium Dioxide Particles Due to Scattered Light - 3° Total Angle Wedge at 0° Angle of Attack.

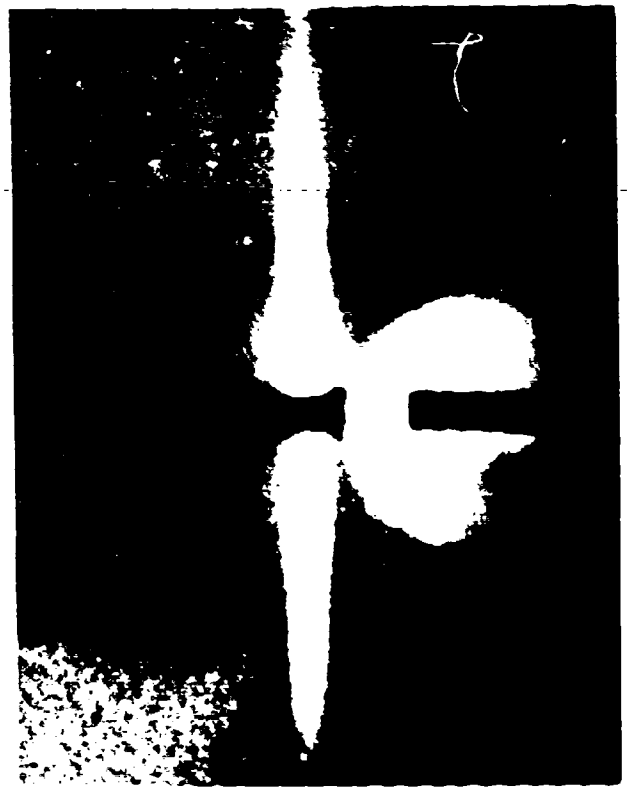

Figure 51. Profile of Titanium Dioxide Particles Due to Scattered Light - 5° Total Angle Wedge at 0° Angle of Attack.

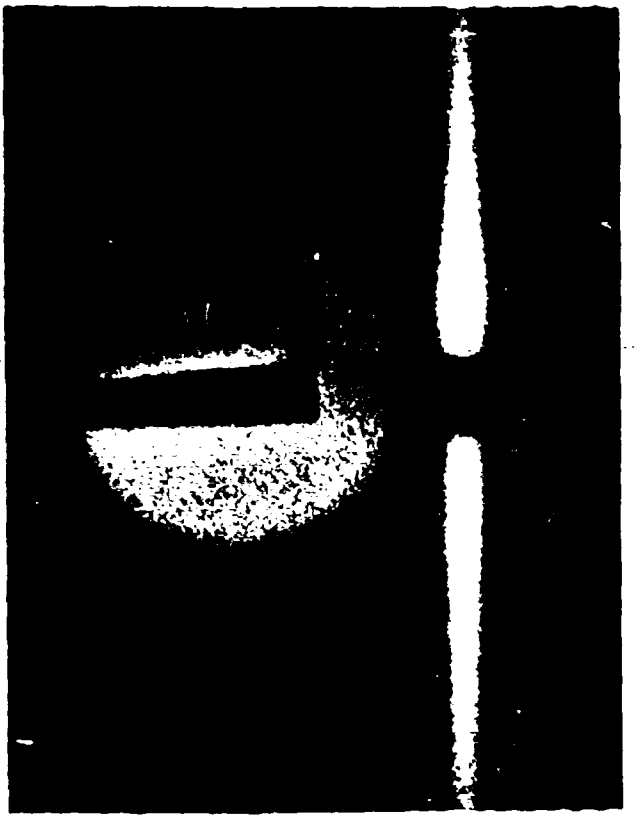

Figure 28. Profile of Titanium Dioxide Particles due to Scattered Light - ° Total Angle Wedge at 2.5° Angle of Attack.

Figure 33. Profile of Titanium Dioxide Particles due to Scattered Light - 5° Total Angle Wedge at 7.5° Angle of Attack.

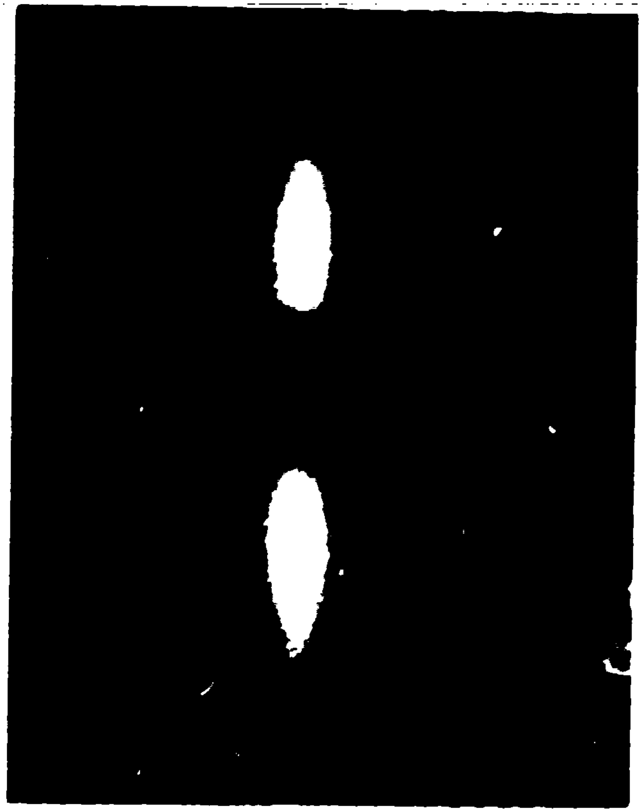

Figure [illegible]. Profile of [illegible] Particles [illegible] to [illegible] – [illegible]° Total Angle Range [illegible] Angle of Attack.

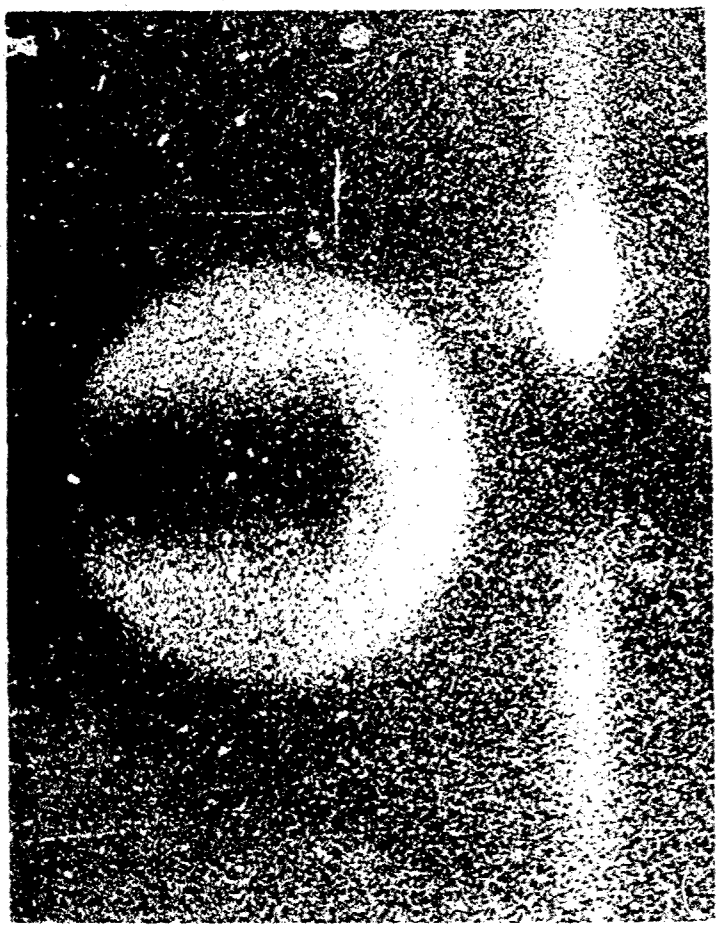

Figure 55. Profile of Titanium Dioxide Particles Due to Scattered Light - 15° Total Angle Wedge at 10° Angle of Attack.

SECTION IV

SUMMARY AND CONCLUSIONS

The experimental and theoretical results of this study have provided new information regarding the behavior of solid particles in high speed flow systems. A new drag coefficient correlation which allows greater accuracy in the prediction of particle trajectories over a wide range of slip Mach number and slip Reynolds number was formulated. A variety of basic two-phase flow situations were investigated, i.e., uniform flow, Prandtl-Meyer expansion, and oblique shock, by varying the initial particle velocity and particle radius. In addition, the effects of different gases and different particles on the two-phase flow characteristics were investigated and significant differences were noted. The exploratory experimental studies conducted in this investigation substantiate that a test facility suitable for the study of particle trajectories has been developed and that accurate particle concentration profiles can be obtained with the laser scattering technique.

REFERENCES

1. Johnson, E. G., and von Ohain, J. P. Hans, "Generation of Ultra High Total Enthalpy Gases Through Multi-Component Flow Techniques," AIAA Paper No. 72-167 (January 1972). Available as NTIS No. N72-26247.

2. Rudinger, G., "Dynamics of Gas Particles Mixtures With Finite Particle Volume," AIAA 2nd Aerospace Sciences Meeting (January 1965).

3. Hultberg, J. A., and Soo, S. L., "Flow of a Gas Solid Suspension Through a Nozzle," AIAA 2nd Aerospace Sciences Meeting (January 1965).

4. Chu, T. T., and Chow, J. C. F., "On a Microscopic Theory of a Two-Phase Fluid," AIAA 2nd Aerospace Sciences Meeting (January 1965).

5. Fulmer, R. D., and Wirtz, D. P., "Measurement of Individual Particle Velocities in a Simulated Rocket Exhaust," AIAA 2nd Aerospace Sciences Meeting (January 1965).

6. Kliegel, J. R., "Gas Particle Nozzle Flows," 9th Symposium on Combustion, Academic Press, New York (1963).

7. Hsu, T. T., "Review of Critical Flow Rate, Propagation of Pressure Pulse, and Sonic Velocity in Two-Phase Media," NASA TN D-6614 (June 1972).

8. Simmons, F. S., and Spadaro, P. G., "Thermal Lag of Solid Carbon in Rocket Nozzle Flow," Paper No. 60-2, Rocketdyne Division, North American Aviation (April 1960).

9. Meyer, R. E., "Focusing Effects in Two-Dimensional, Supersonic Flow," Soc. Ind. Appl. Soc., 242A, 21 (December, 1949).

10. Kliegel, J. R., "Gas-Particle Nozzle Flows," Ninth Symposium on Combustion, Academic Press, New York (1963).

11. Hoglund, R. F., "Recent Advances in Gas-Particle Nozzle Flows," ARS J., 32, 662-671 (1962).

12. Carlson, D. J., and Hoglund, R. F., "Particle Drag and Heat Transfer in Rocket Nozzles," AIAA J., 2, 1980-1984 (1964).

13. Bartz, D. R., "A Simple Equation for Rapid Estimation of Rocket Nozzle Convective Heat Transfer Coefficients," Jet Propulsion, 27, 49-51 (1957).

14. Adler, B. K., and Anderson, R. B., "Transport Properties of Polar and Polyatomic Gas Mixtures," North American Aviation, Inc., Space and Information Systems Division, SID 67-490 (1967).

15. Bailey, A. B., and Hiatt, J., "Free-Flight Measurements of Sphere Drag at Subsonic, Transonic, Supersonic and Hypersonic Speeds for Continuum, Transition, and Near Free Molecular Flow Conditions," AEDC-TR-70-291 (March 1971).

16. Crowe, C. T., "Drag Coefficient of Particles in a Rocket Nozzle," AIAA J., 5, 1021-1022 (1967).

17. Cuddihy, W. F., Beckwith, I. E., and Schroeder, L. C., "A Solution to the Problem of Communications Blackout of Hypersonic Re-Entry Vehicles," Anti-Missile Research Advisory Council Meeting, Annapolis, Maryland, (October 22-24, 1965).

18. Stoney, W. E., Jr., "Collection of Zero Lift Drag Data on Bodies of Revolution from Free-Flight Investigations," NACA TN 4201, (January 1958).

19. Ferrara, R., Fiocco, G., and Tonna, G., "Evolution of the Fog Droplet Size Distribution Observed by Laser Scattering," Applied Optics, 9, 2517 (November 1970).

20. Daum, F. L., and Farrell, C. A., "Light Scattering Instrumentation for Detecting Air Condensation in a Hypersonic Wind Tunnel," ARL 71-0115 (July 1971). AD 729 718.

21. Lordi, J. A., Mates, R. E., and Moselle, J. R., "Computer Programs for Numerical Solution of Nonequilibrium Expansions of Reacting Gas Mixtures," NASA CR-472 (1968).

22. Edenfield, E. E., and Boudreau, A. H., "A Correlation of Boundary Layer Thickness and Displacement Thickness of Hypersonic Mach Numbers," 26th Semiannual Meeting of Supersonic Tunnel Association (September 1966).

23. Ebesstein, I. J., "Use of Pulsed Laser to Study Smoke Distribution in a Jet," Rev. Sci. Instruments, 38, 1655 (November, 1967).

APPENDIX A

UNIFORM FLOW

This appendix contains the following cases:

α (°)	r_p (μm)	u_p (ft/s)	(r vs z)	(u_p vs z)	(T_p vs z)
45	0.5	100			
45	0.5	1000	x		
45	0.5	2000			
45	5	100	x	x	x
45	5	1000	x		
45	5	2000	x		
45	25	100	x	x	x
45	25	1000	x		
45	25	2000	x		
45	50	100			
45	50	1000	x		
45	50	2000	x		

Note: These numerical calculations were carried out for the following conditions:

MW = Air (29)	P_∞ = 7876.8 psf
α_{p_i} = 45°	T_∞ = 540°R
θ_g = 0°	M_∞ = 5.0
T_{p_i} = 540°R	Titanium Dioxide

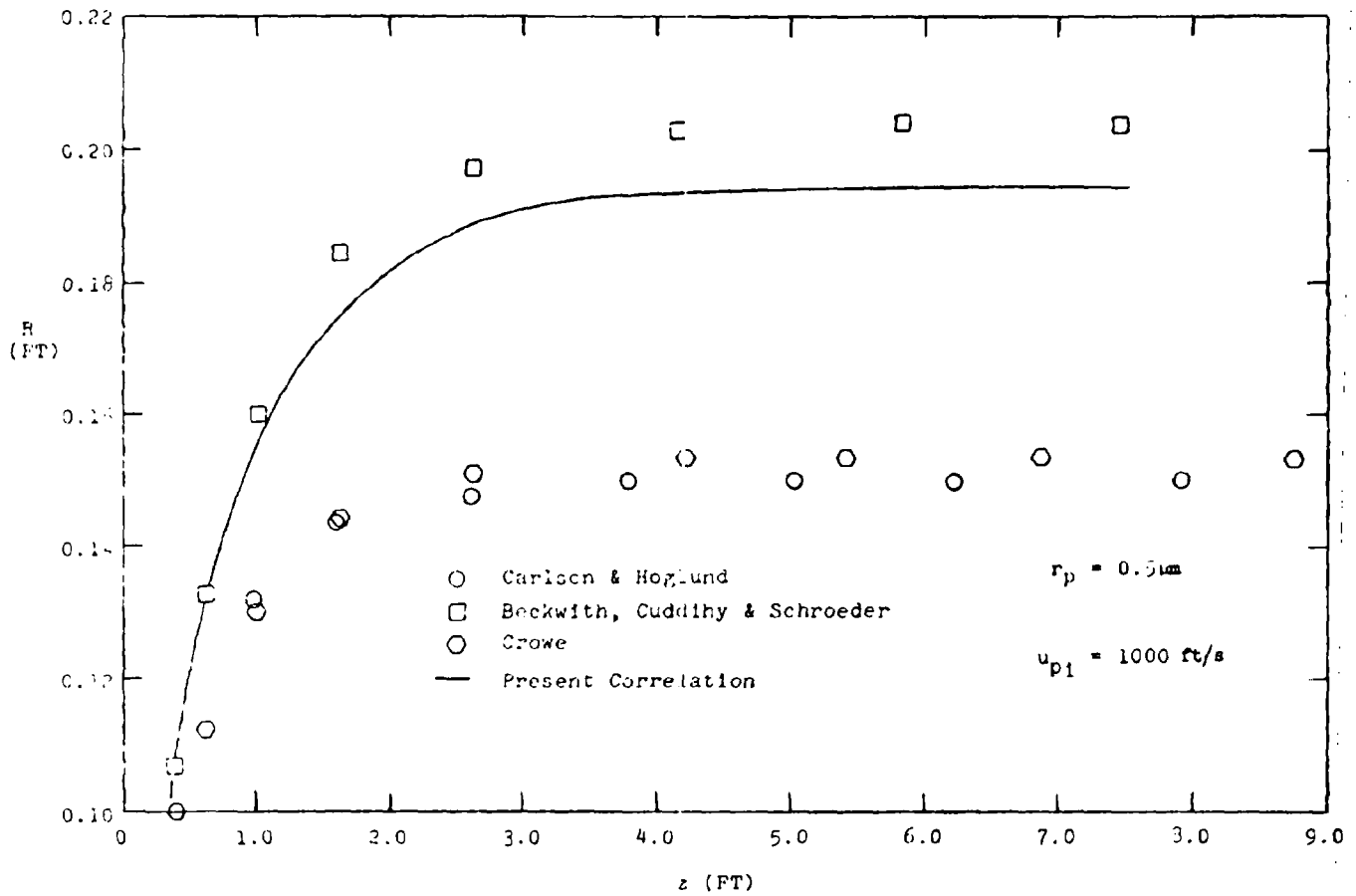
0.22
0.20
0.18
R
(FT)
0.10
0
1.0
2.0
3.0
4.0
5.0
6.0
7.0
8.0
9.0
z (FT)
Carlson & Hoglund
Beckwith, Cuddihy & Schroeder
Crowe
Present Correlation
r_p = 0.5μm
u_{p1} = 1000 ft/s

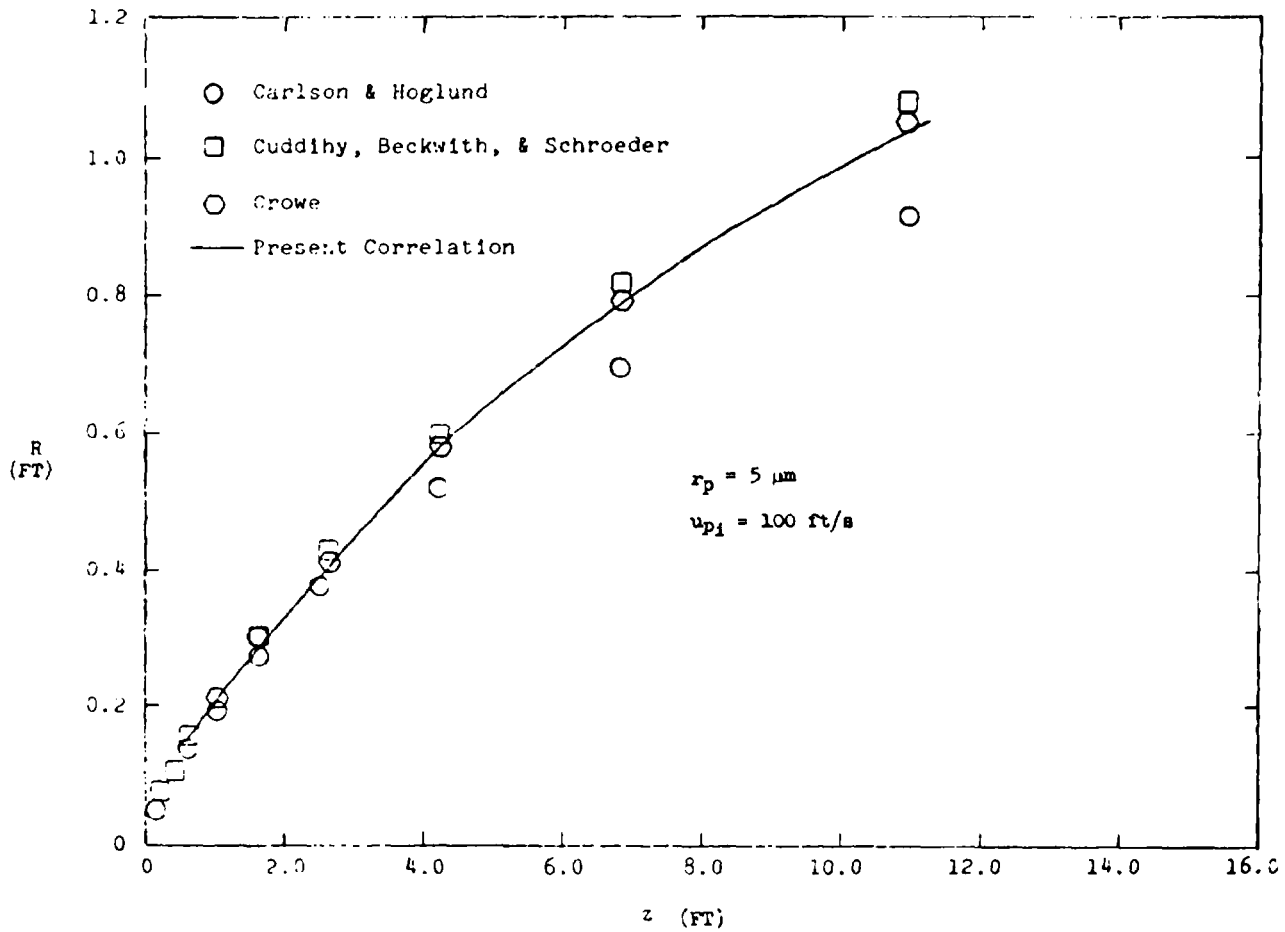
Carlson & Hoglund
Cuddihy, Beckwith, & Schroeder
Crowe
Present Correlation
r_p = 5 μm
u_{p_i} = 100 ft/s
R (FT)
z (FT)
0
0.2
0.4
0.6
0.8
1.0
1.2
2.0
4.0
6.0
8.0
10.0
12.0
14.0
16.0

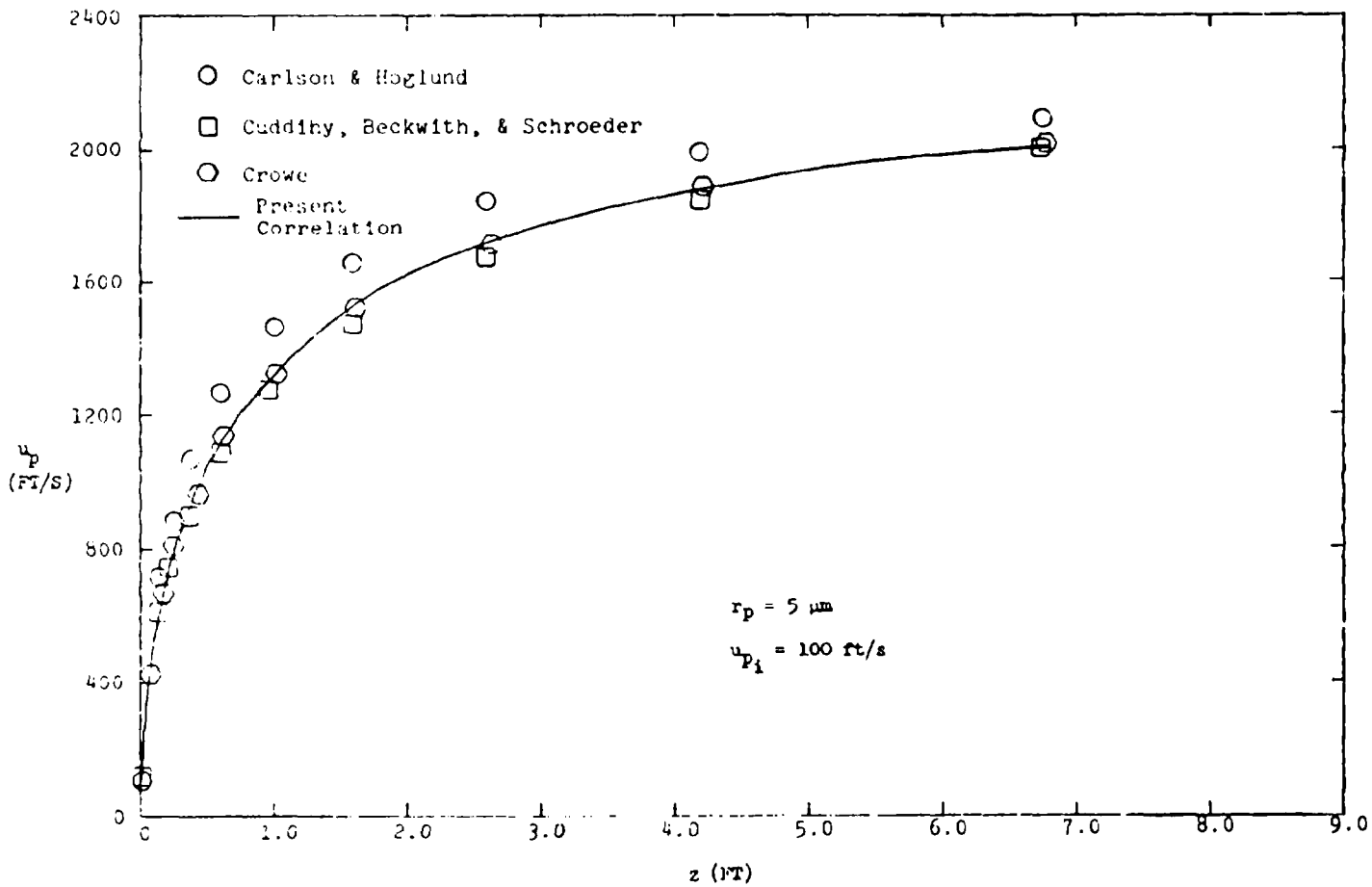
2400
2000
1600
1200
800
400
0
u_p (FT/S)
Carlson & Hoglund
Cuddihy, Beckwith, & Schroeder
Crowe
Present Correlation
r_p = 5 μm
u_{p_i} = 100 ft/s
0
1.0
2.0
3.0
4.0
5.0
6.0
7.0
8.0
9.0
z (FT)

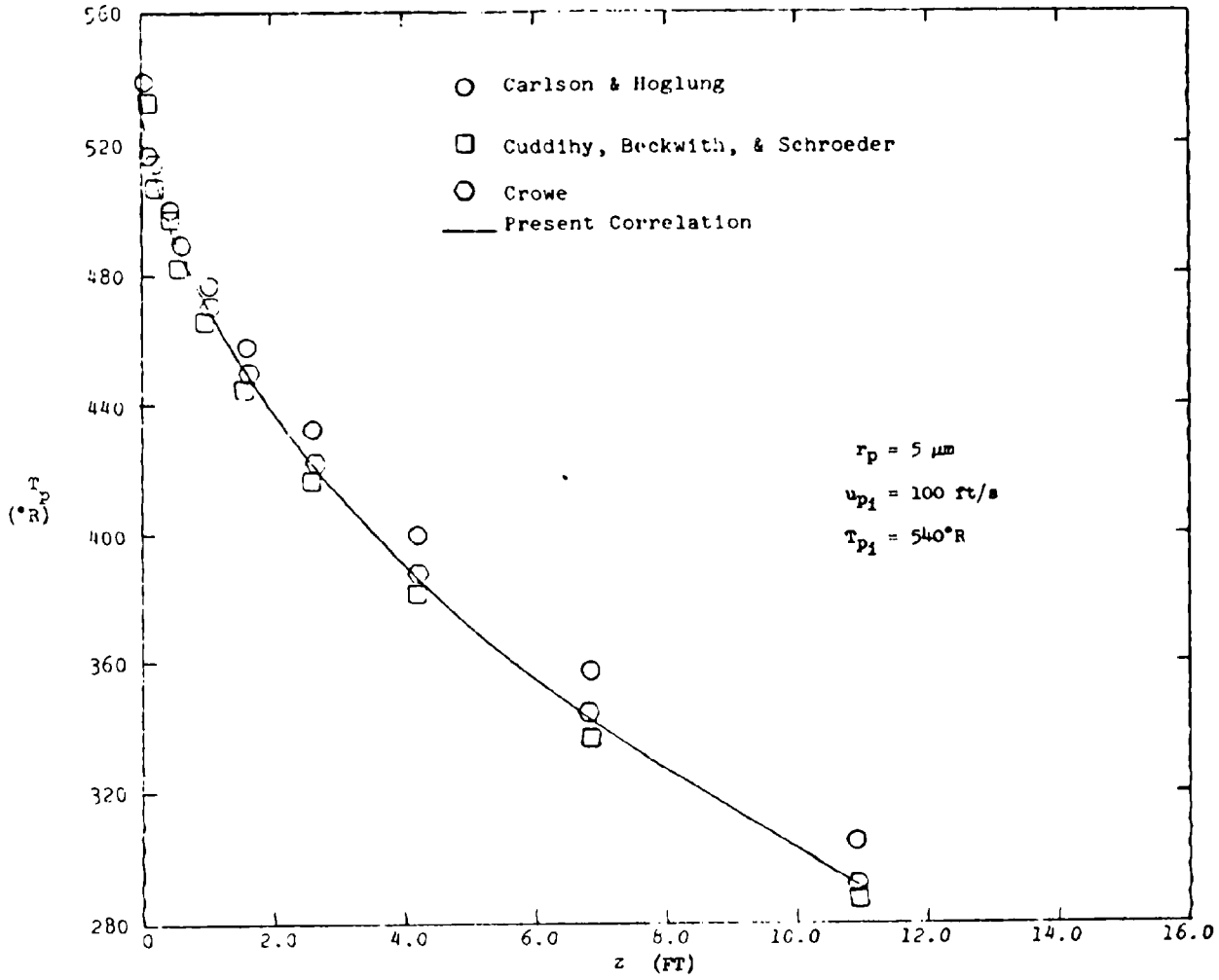
560
520
480
440
400
360
320
280
T_p (°R)
0
2.0
4.0
6.0
8.0
10.0
12.0
14.0
16.0
z (FT)
Carlson & Hoglung
Cuddihy, Beckwith, & Schroeder
Crowe
Present Correlation
r_p = 5 μm
u_{p_i} = 100 ft/s
T_{p_i} = 540°R

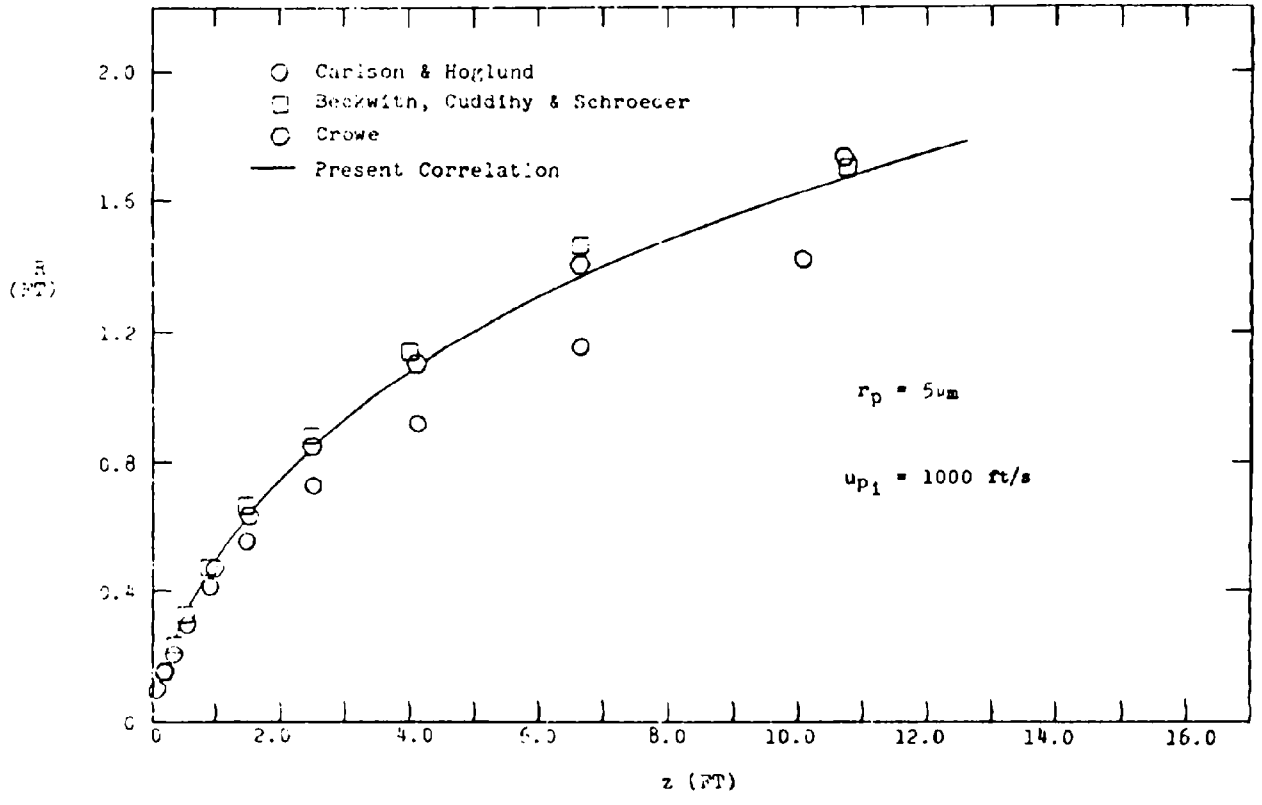
Carlson & Hoglund
Boswith, Cuddihy & Schroeder
Crowe
Present Correlation
r_p = 5μm
u_{p_1} = 1000 ft/s
2.0
1.6
1.2
0.8
0.4
0
0
2.0
4.0
6.0
8.0
10.0
12.0
14.0
16.0
z (FT)

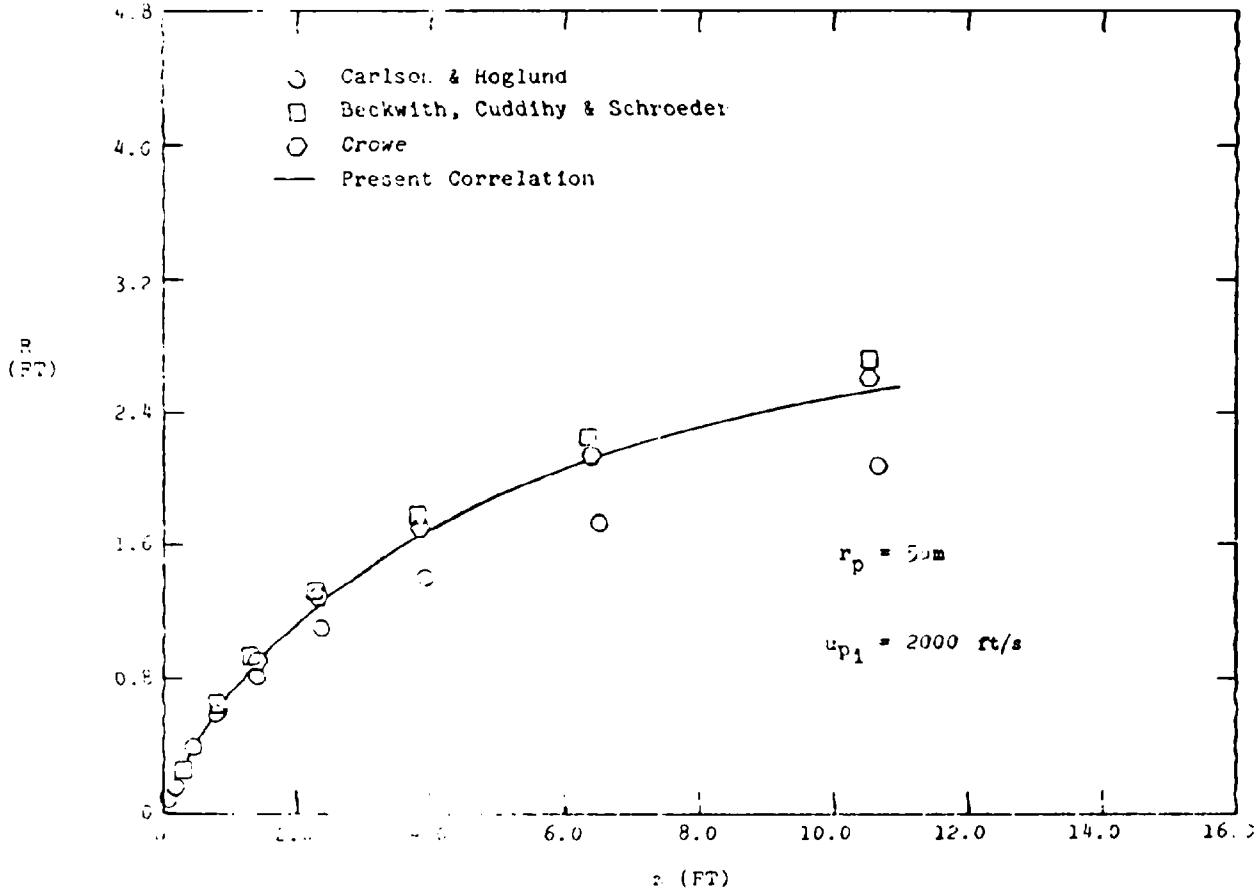
Carlson & Hoglund
Beckwith, Cuddihy & Schroeder
Crowe
Present Correlation
r_p = 5μm
u_{p_i} = 2000 ft/s
4.8
4.0
3.2
2.4
1.6
0.8
0
6.0
8.0
10.0
12.0
14.0
(FT)

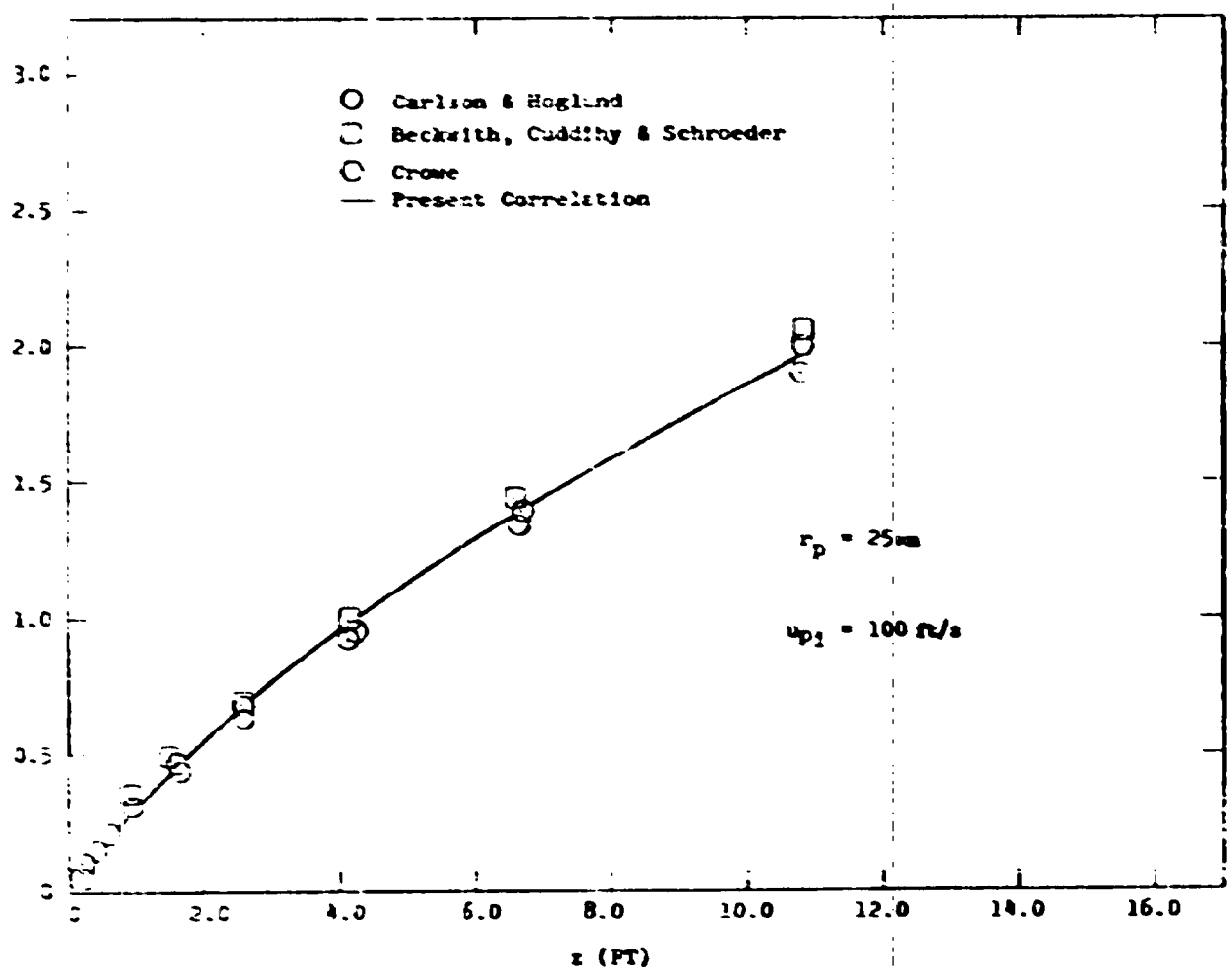
Carlson & Hoglund
Beckwith, Cuddihy & Schroeder
Crowe
Present Correlation
r_p = 25μm
u_{p_1} = 100 ft/s
3.0
2.5
2.0
1.5
1.0
0.5
0
2.0
4.0
6.0
8.0
10.0
12.0
14.0
16.0
x (FT)

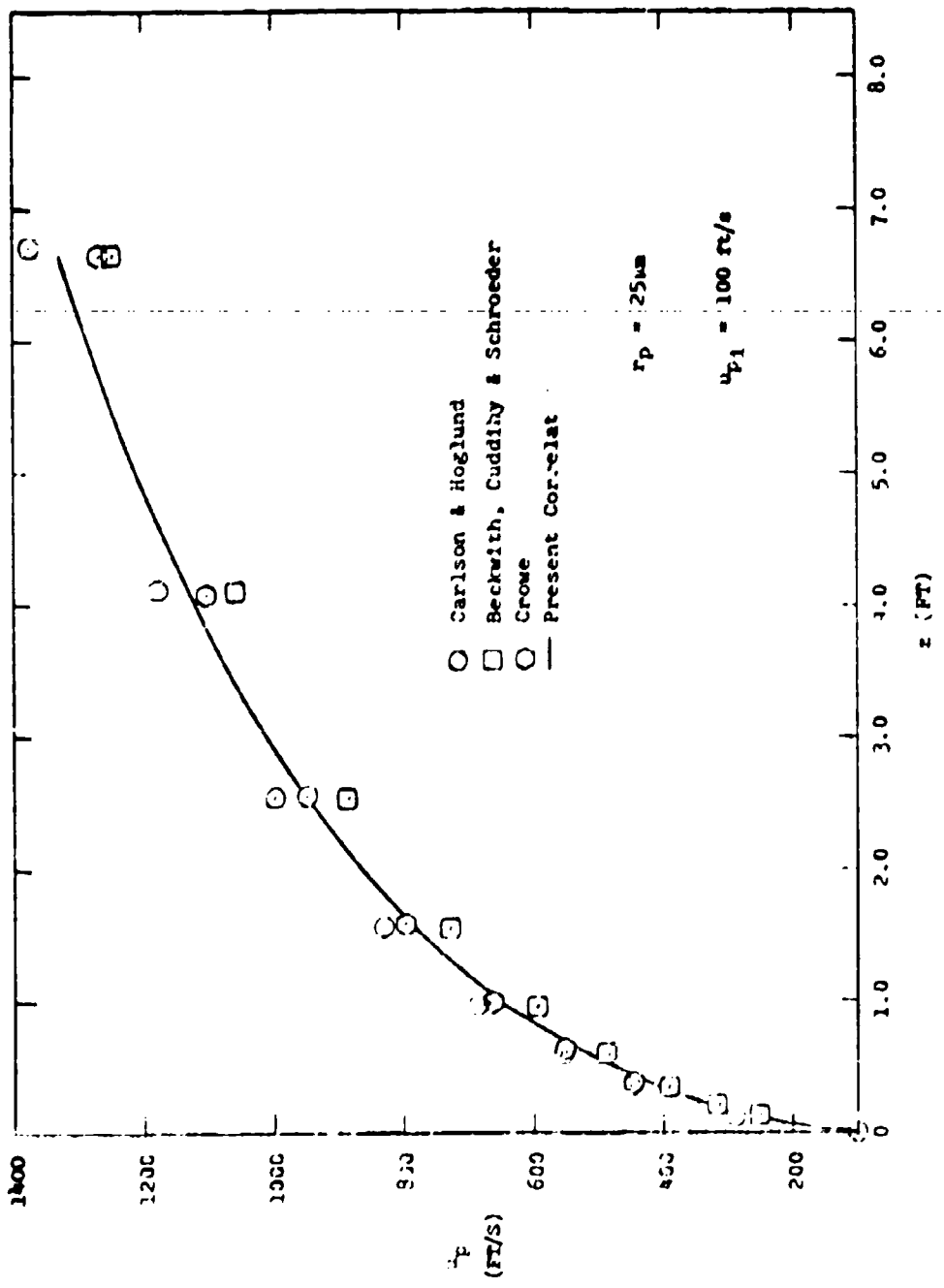
Carlson & Hoglund
Beckwith, Cuddihy & Schroeder
Crowe
Present Correlat
r_p = 25μm
u_{p1} = 100 ft/s
z (FT)
(FT/S)
1400
1200
1000
800
600
400
200
0
1.0
2.0
3.0
4.0
5.0
6.0
7.0
8.0

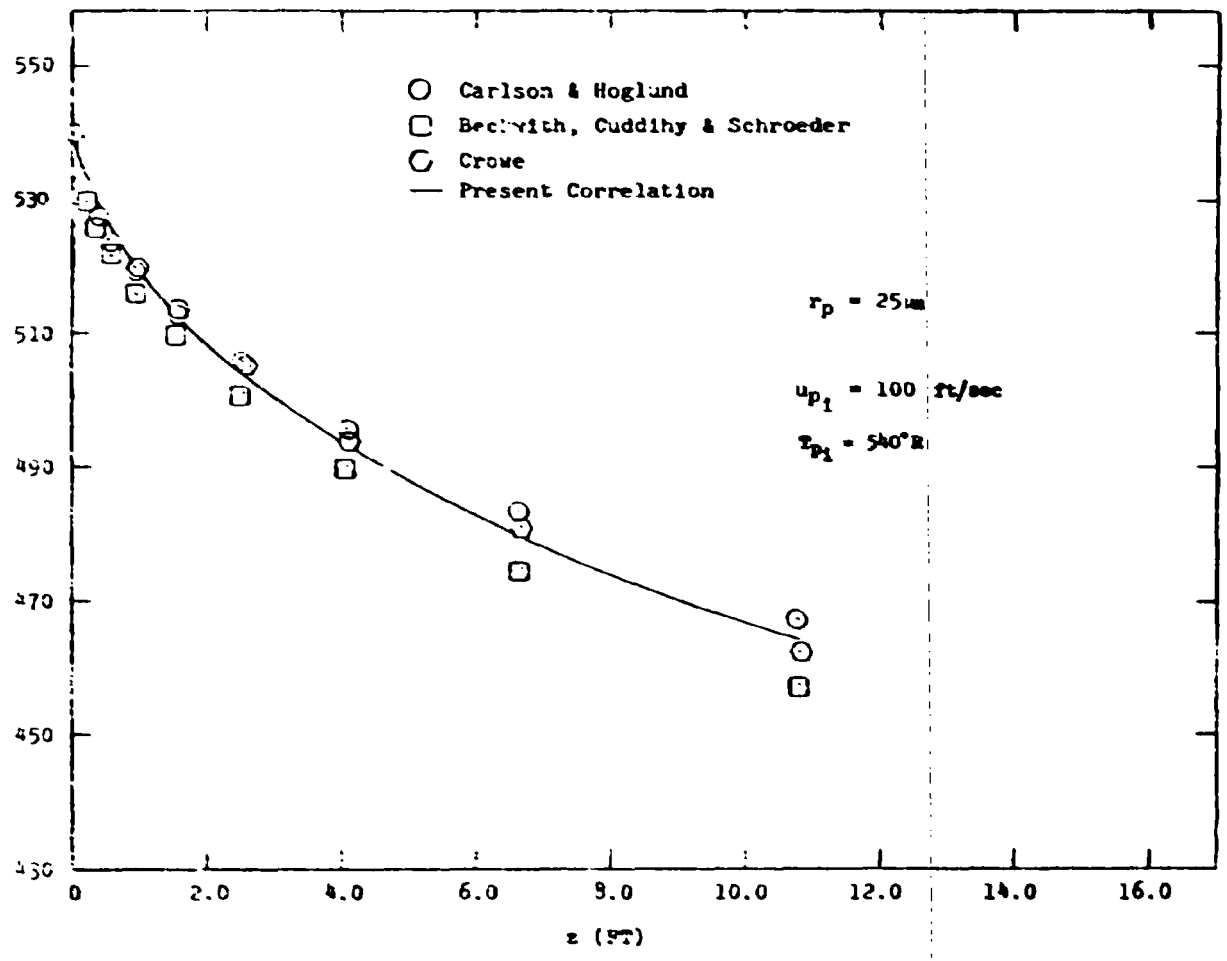
Carlson & Hoglund
Beckwith, Cuddihy & Schroeder
Crowe
Present Correlation
r_p = 25μm
u_{p_i} = 100 ft/sec
T_{p_i} = 540°R
550
530
510
490
470
450
430
0
2.0
4.0
6.0
8.0
10.0
12.0
14.0
16.0
z (ft)

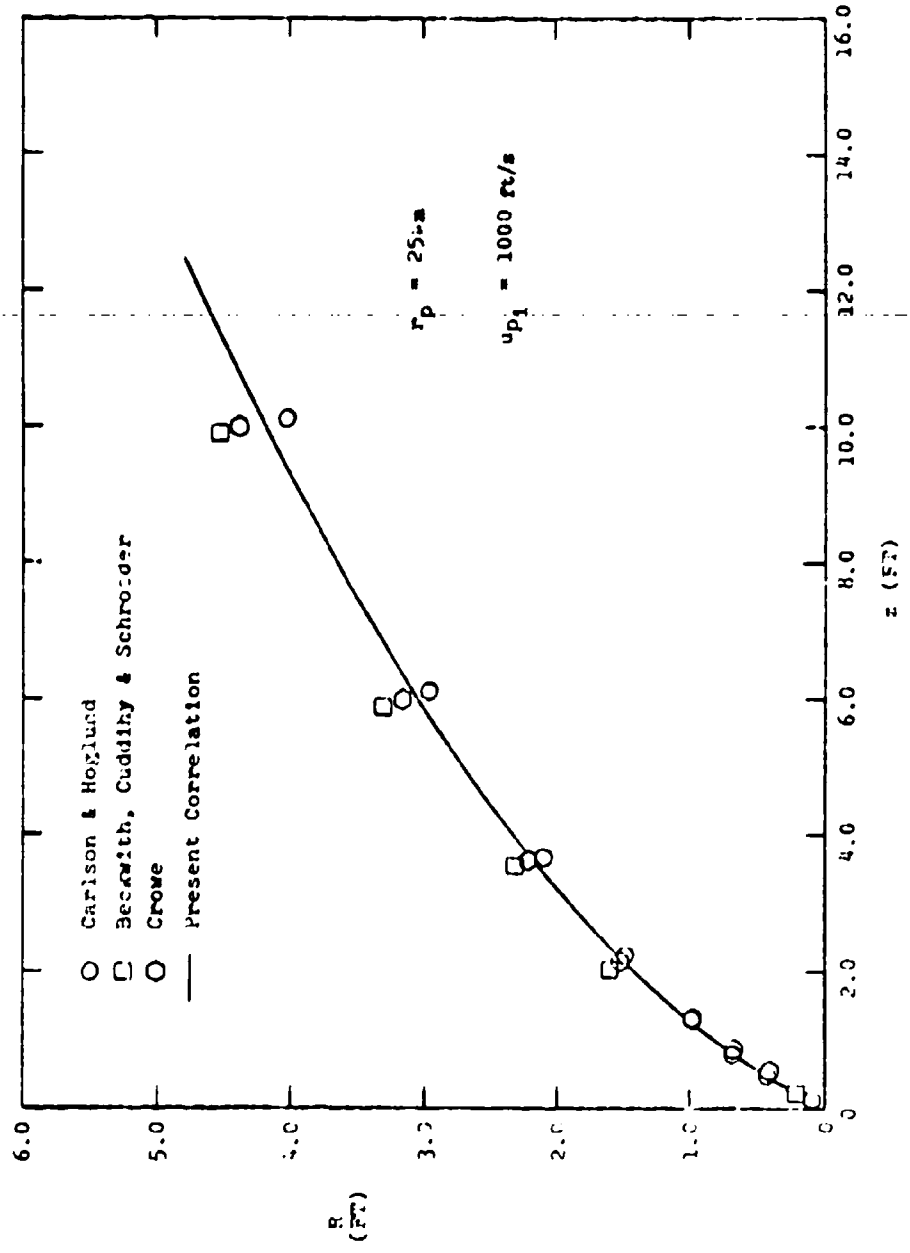
Carlson & Hoglund
Beckwith, Cuddihy & Schroder
Crowe
Present Correlation
r_p = 25μm
u_{p_1} = 1000 ft/s
R (FT)
z (FT)
6.0
5.0
2.0
4.0
6.0
8.0
10.0
12.0
14.0
16.0

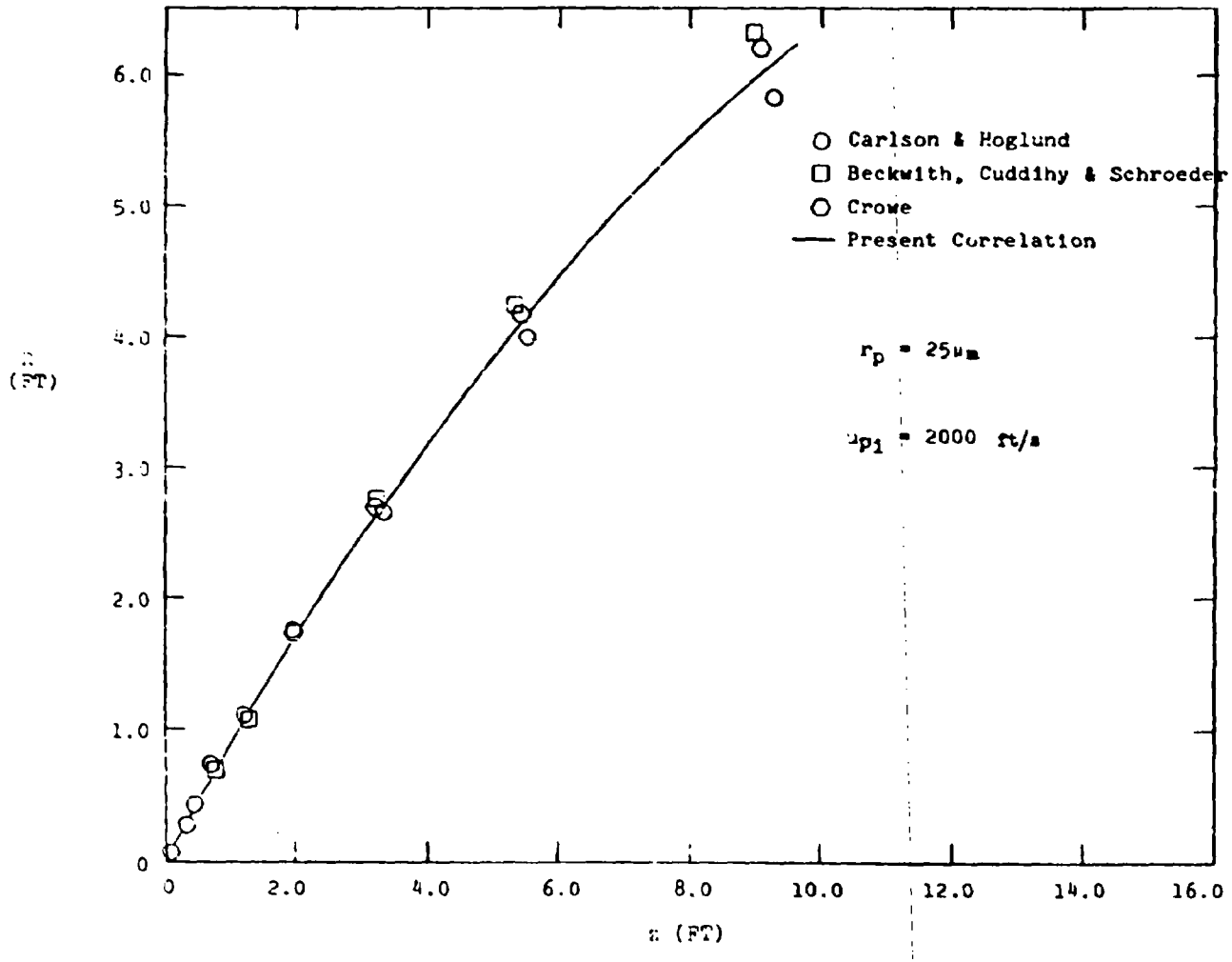
6.0
5.0
4.0
3.0
2.0
1.0
0
0
2.0
4.0
6.0
8.0
10.0
12.0
14.0
16.0
z (FT)
(FT)
Carlson & Hoglund
Beckwith, Cuddihy & Schroeder
Crowe
Present Correlation
r_p = 25μm
v_{p_1} = 2000 ft/s

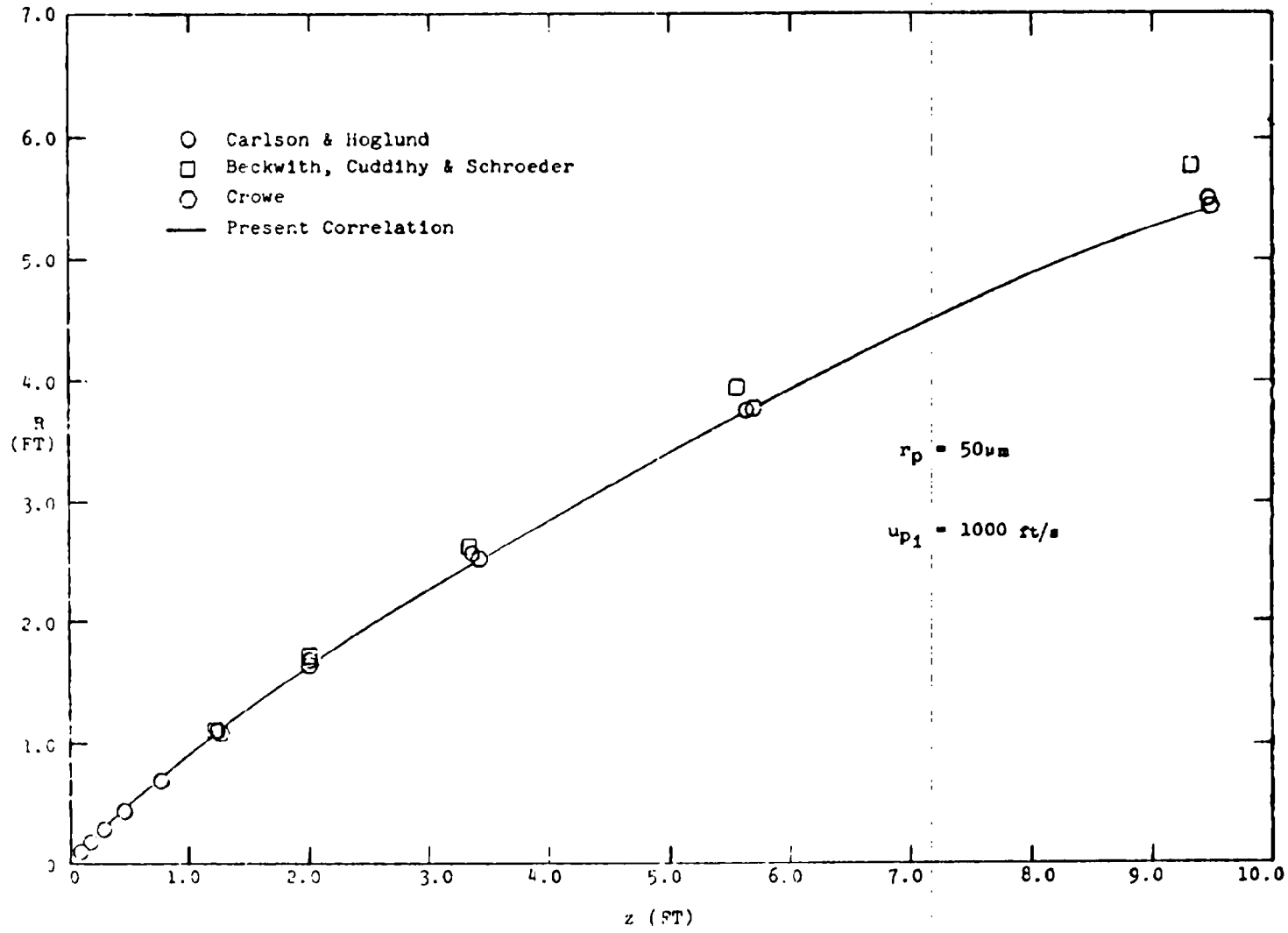
Carlson & Hoglund
Beckwith, Cuddihy & Schroeder
Crowe
Present Correlation
r_p = 50μm
u_{p_1} = 1000 ft/s
R (FT)
z (FT)
0
1.0
2.0
3.0
4.0
5.0
6.0
7.0
8.0
9.0
10.0

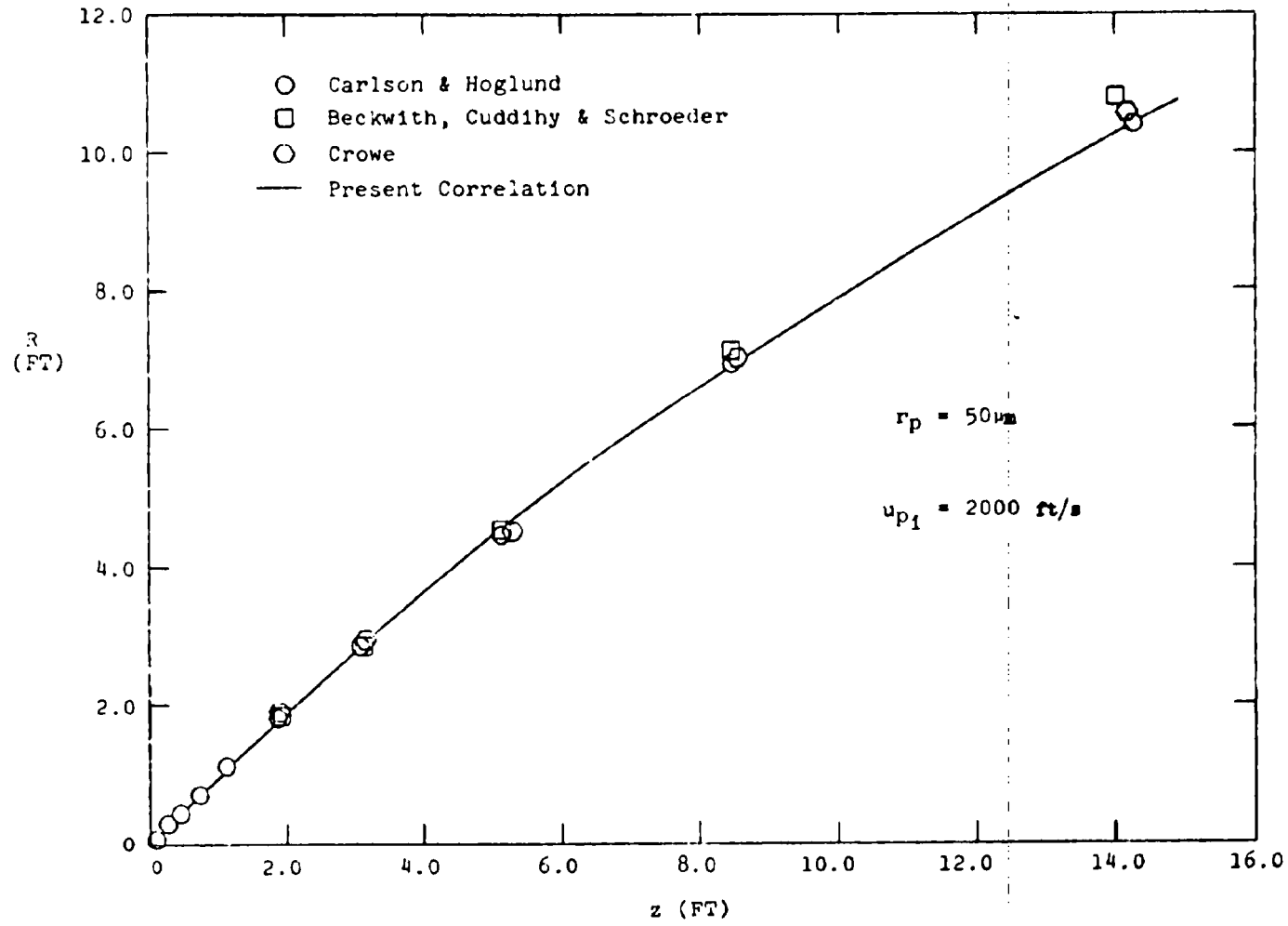
12.0
10.0
8.0
6.0
4.0
2.0
0
R
(FT)
Carlson & Hoglund
Beckwith, Cuddihy & Schroeder
Crowe
Present Correlation
r_p = 50μm
u_{p_i} = 2000 ft/s
0
2.0
4.0
6.0
8.0
10.0
12.0
14.0
16.0
z (FT)

APPENDIX B

PRANDTL-MEYER EXPANSION FAN

This appendix contains the following cases:

α (°)	r_p (μm)	u_p (ft/s)	(r vs z)	(u_p vs z)	(T_p vs z)
30	0.5	100			
30	0.5	1000	x		
30	0.5	2000			
30	5	100	x	x	x
30	5	1000	x		
30	5	2000	x		
30	50	100			
30	50	1000	x		
30	50	2000	x		

Note: These numerical calculations were carried out for the following conditions:

MW = Air (29)	P_∞ = 7876.8 psf
α_{p_i} = 0°	T_∞ = 540°R
θ_w = -30°	M_∞ = 5.0
T_{p_i} = 540°R	Titanium Dioxide

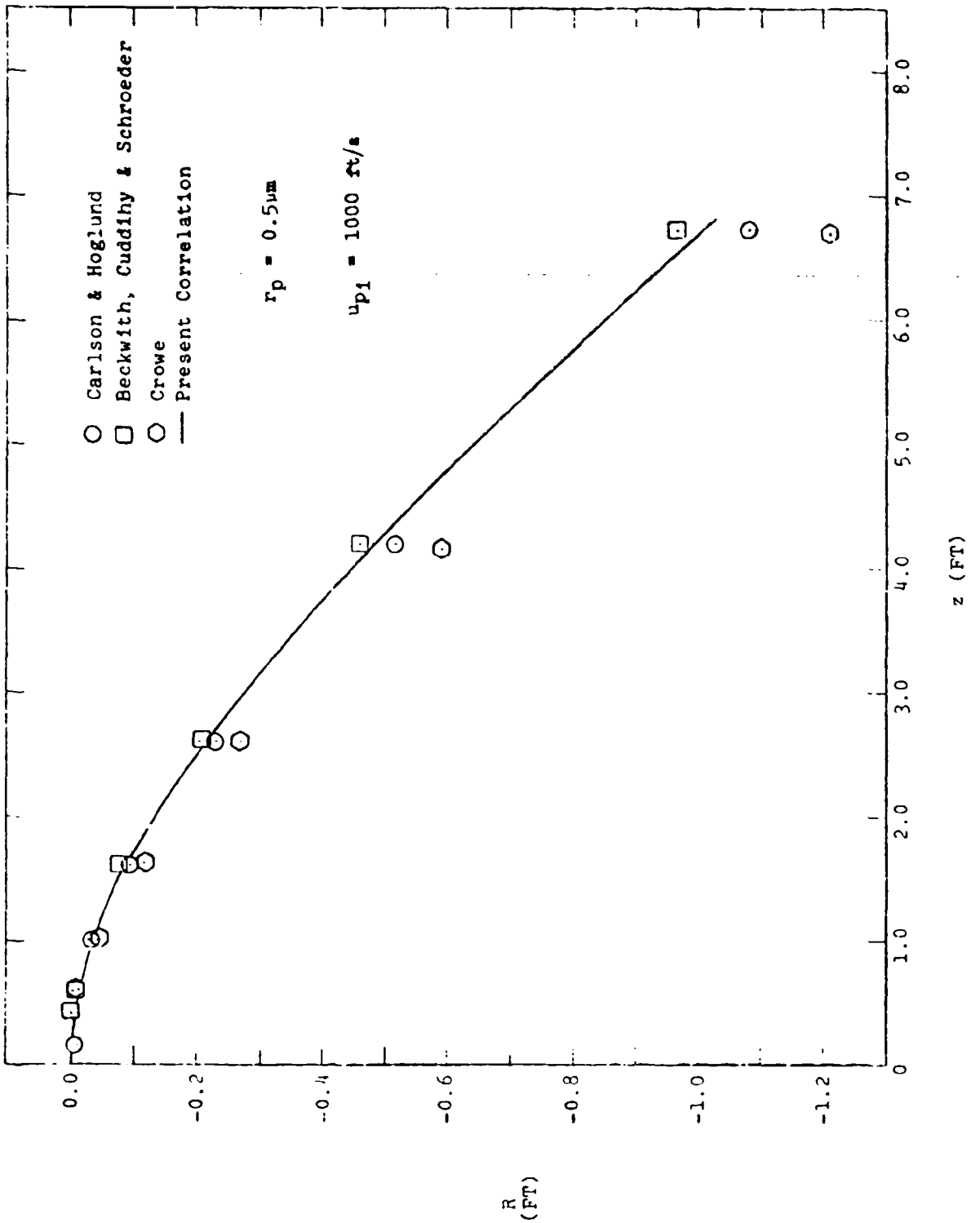
Carlson & Hoglund
Beckwith, Cuddihy & Schroeder
Crowe
Present Correlation
r_p = 0.5μm
u_{p1} = 1000 ft/s
R (FT)
z (FT)
0.0
-0.2
-0.4
-0.6
-0.8
-1.0
-1.2
0
1.0
2.0
3.0
4.0
5.0
6.0
7.0
8.0

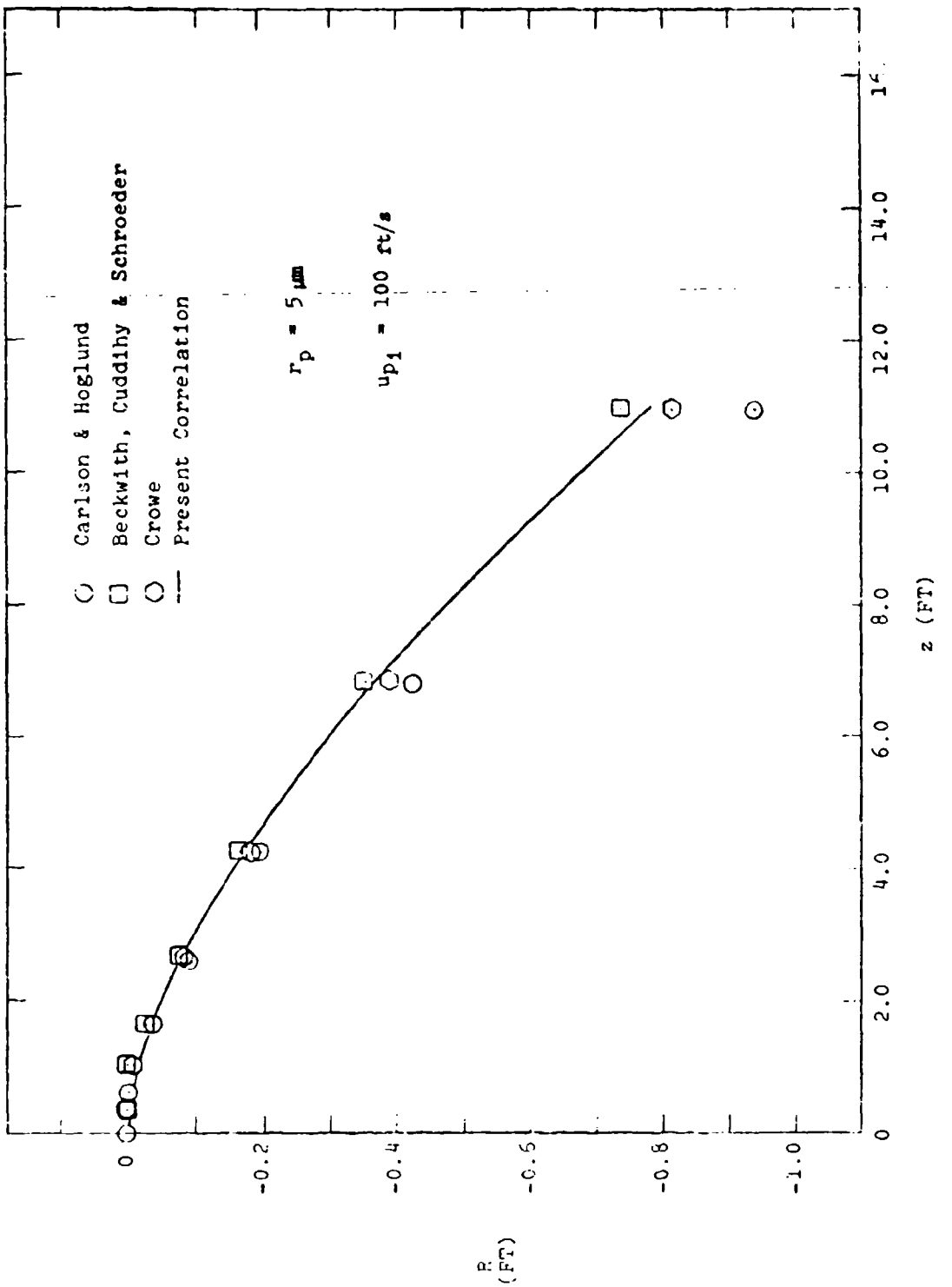
Carlson & Hoglund
Beckwith, Cuddihy & Schroeder
Crowe
Present Correlation
r_p = 5 μm
u_{p_1} = 100 ft/s
0
-0.2
-0.4
-0.6
-0.8
-1.0
R (FT)
0
2.0
4.0
6.0
8.0
10.0
12.0
14.0
z (FT)

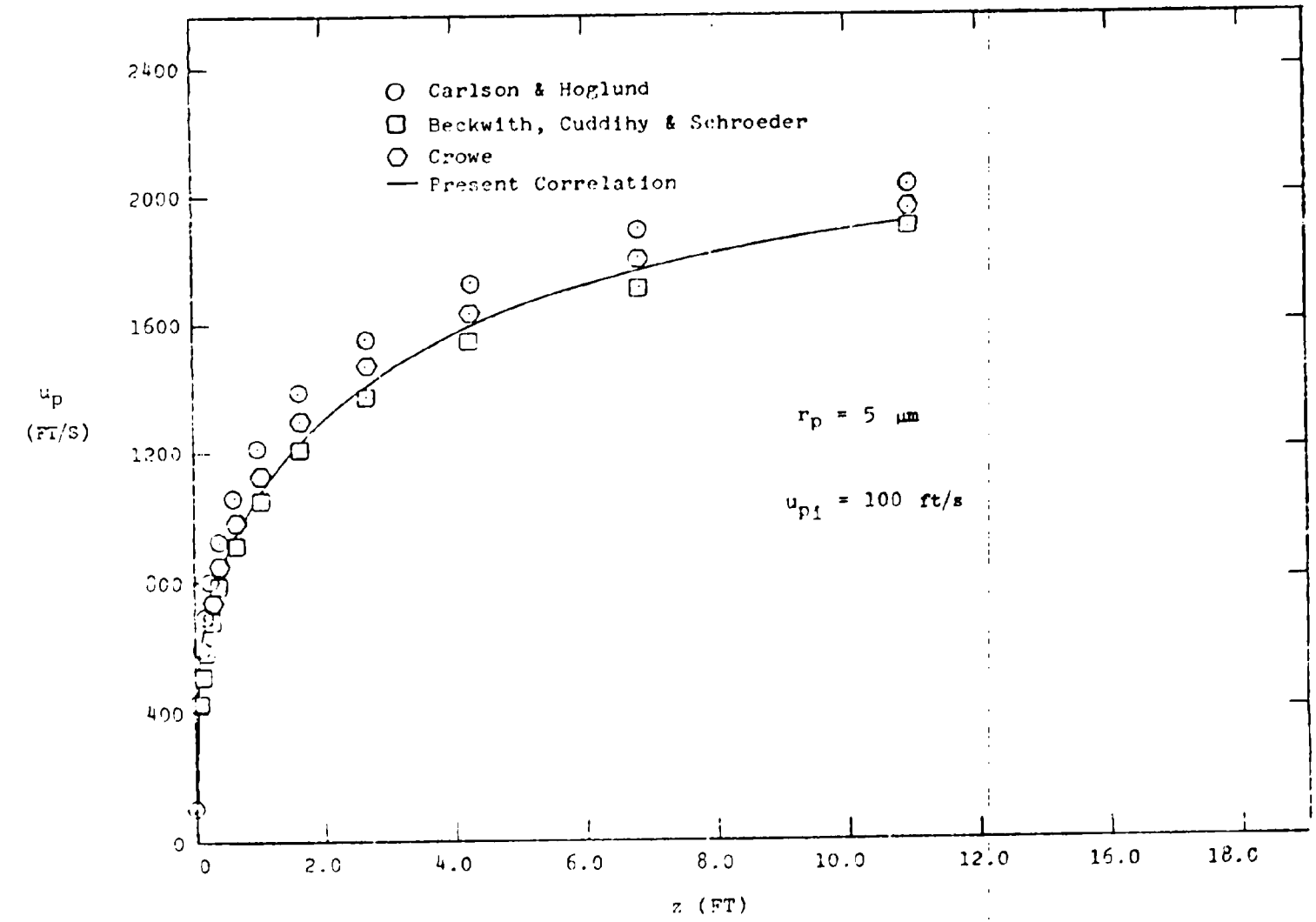
Carlson & Hoglund
Beckwith, Cuddihy & Schroeder
Crowe
Present Correlation
r_p = 5 μm
u_{p_1} = 100 ft/s
u_p (FT/S)
z (FT)
0
400
800
1200
1600
2000
2400
2.0
4.0
6.0
8.0
10.0
12.0
16.0
18.0

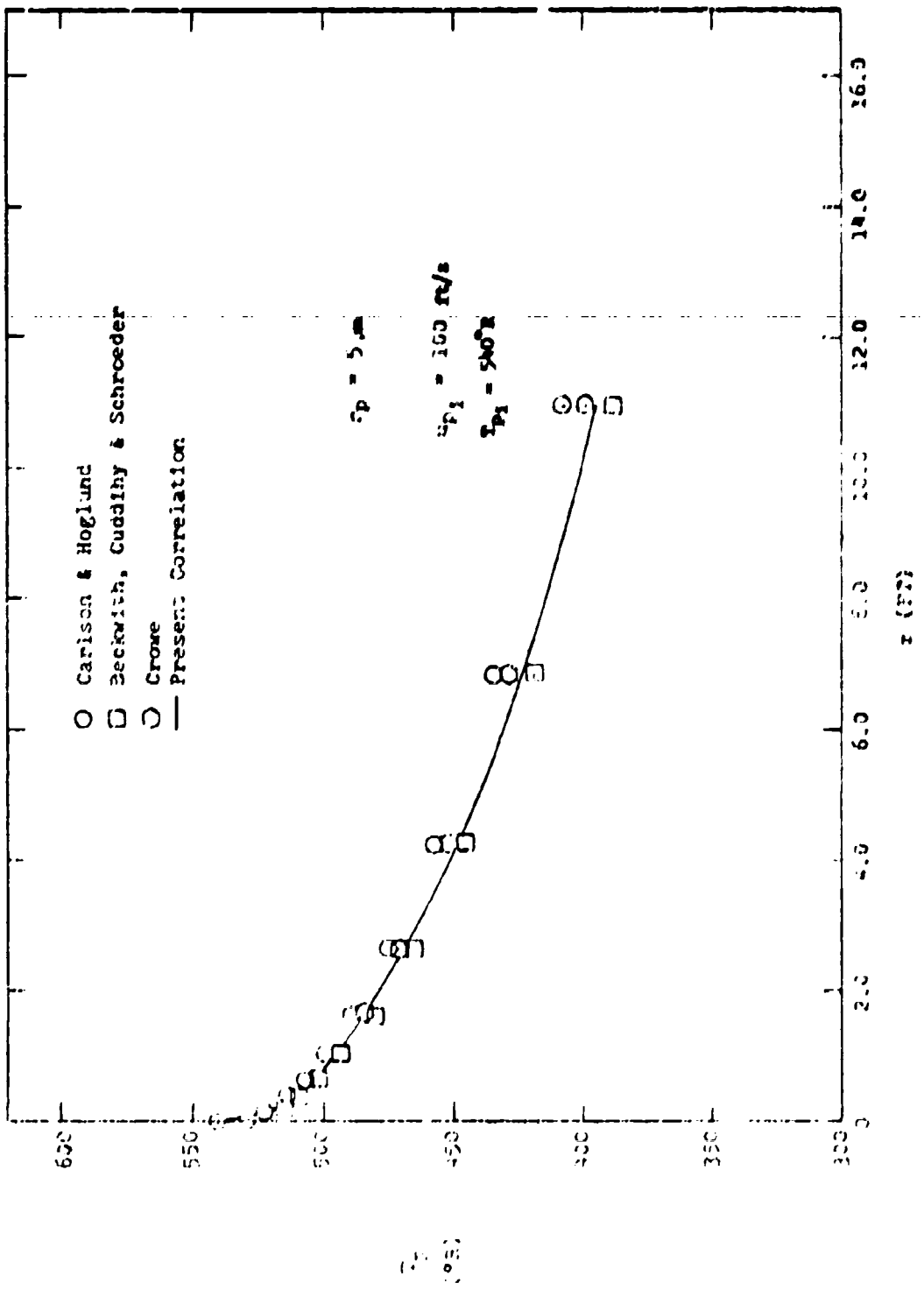
Carlson & Hoglund
Beckwith, Cuddihy & Schroeder
Crowe
Present Correlation
d_p = 5 μm
u_{p_1} = 150 ft/s
T_{p_1} = 540°R
x (ft)

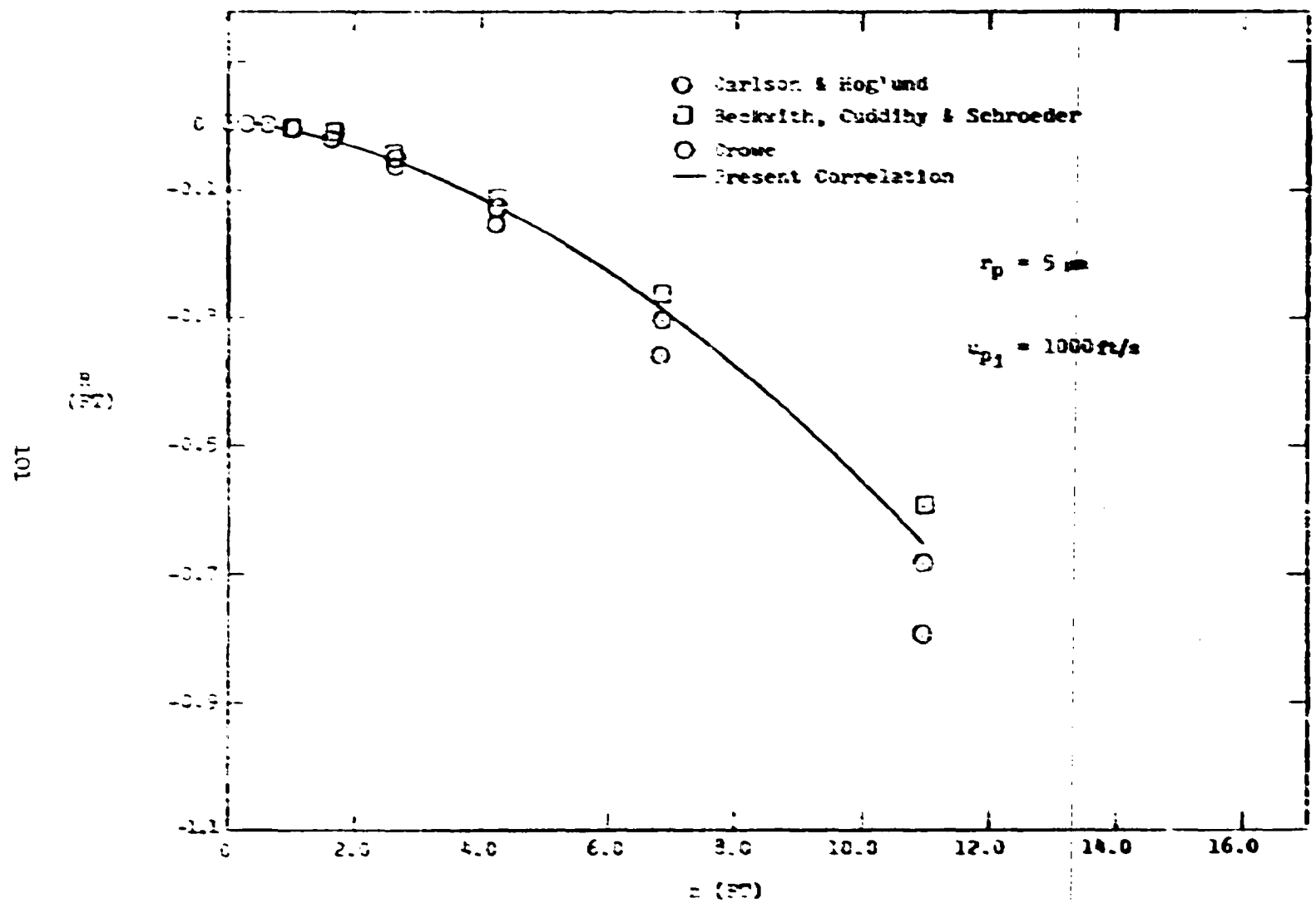
Carlson & Hog'lund
Beckwith, Cuddihy & Schroeder
Crowe
Present Correlation
r_p = 5 μm
v_{p_1} = 1000 ft/s
0
-0.2
-0.4
-0.6
-0.8
-1.0
0
2.0
4.0
6.0
8.0
10.0
12.0
14.0
16.0

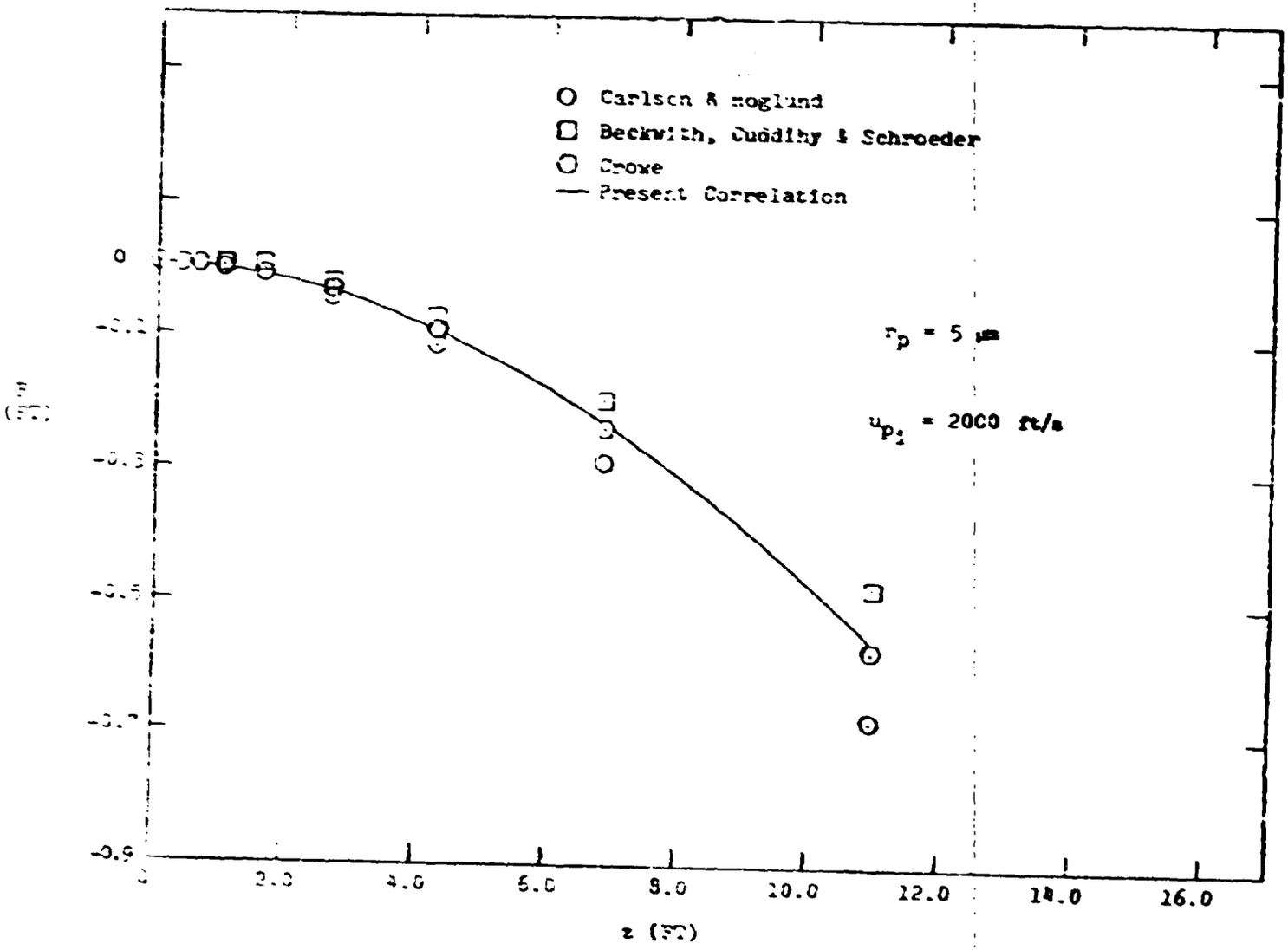
Carlson & Hoglund
Beckwith, Cuddihy & Schroeder
Crowe
Present Correlation
r_p = 5 μm
v_{p_i} = 2000 ft/s
0
-0.3
-0.6
-0.9
2.0
4.0
6.0
8.0
10.0
12.0
14.0
16.0
z (FT)

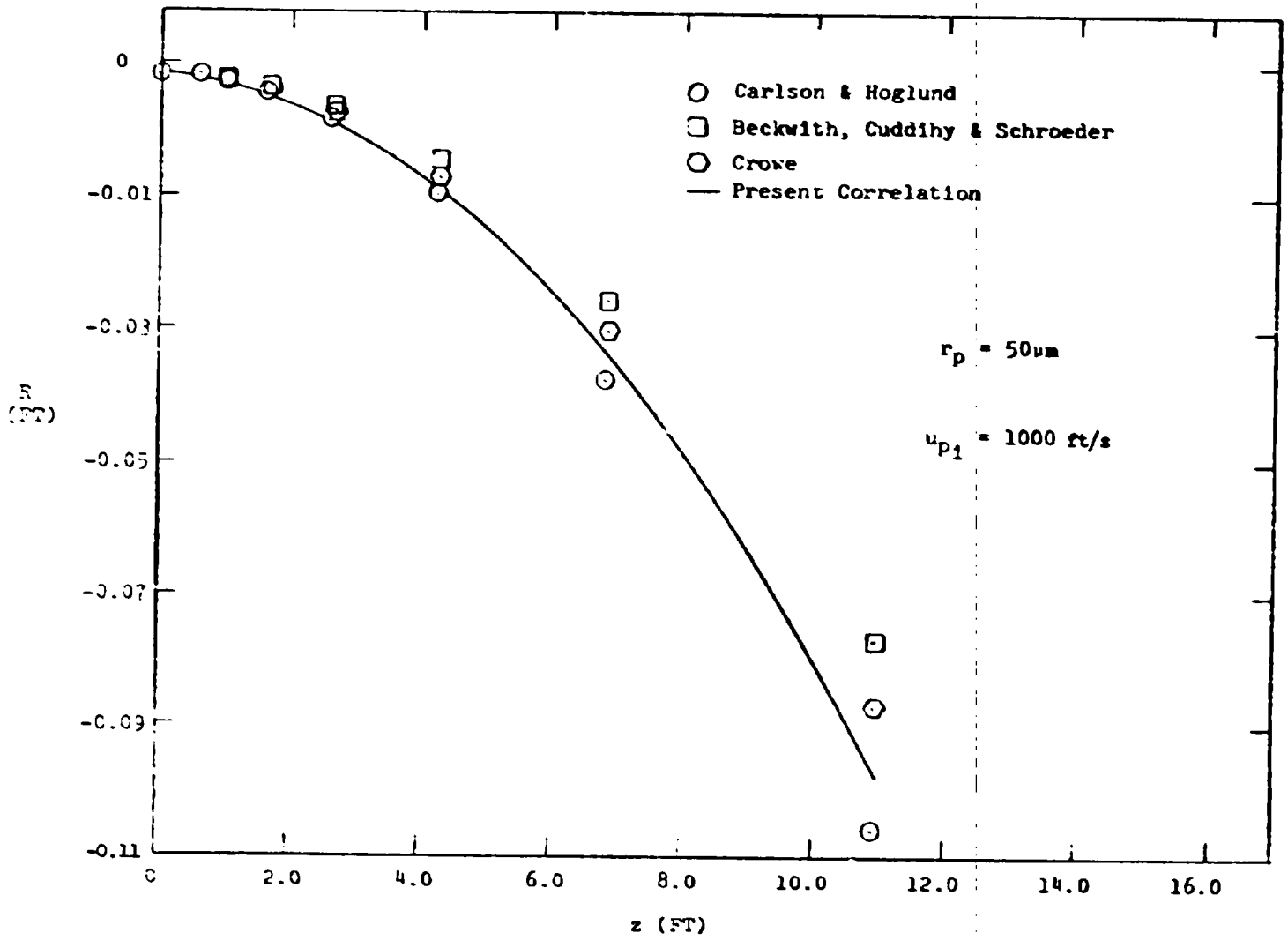
0
-0.01
-0.03
-0.05
-0.07
-0.09
-0.11
0
2.0
4.0
6.0
8.0
10.0
12.0
14.0
16.0
z (FT)
Carlson & Hoglund
Beckwith, Cuddihy & Schroeder
Crowe
Present Correlation
r_p = 50μm
u_{p_1} = 1000 ft/s

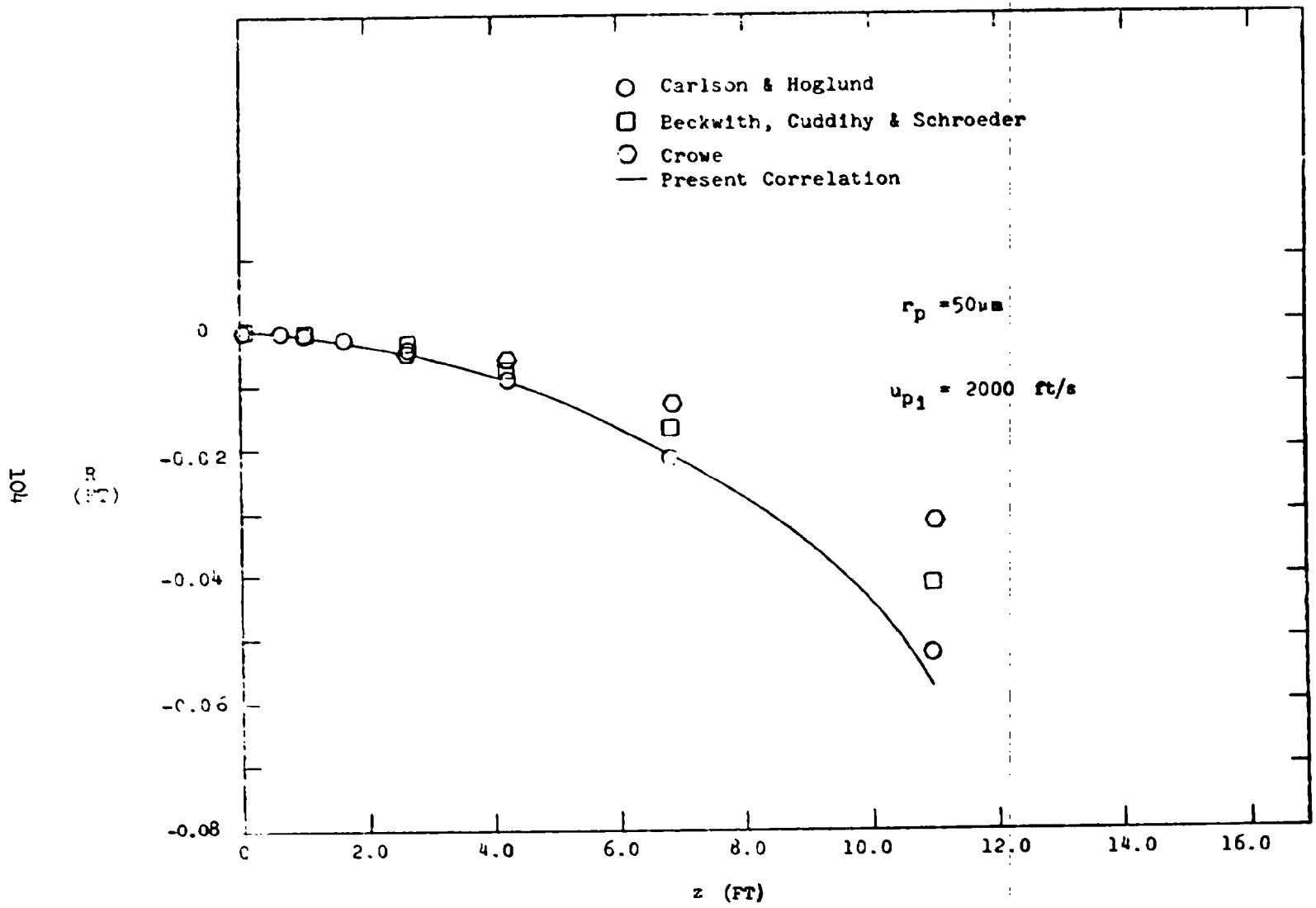
Carlson & Hoglund
Beckwith, Cuddihy & Schroeder
Crowe
Present Correlation
r_p =50um
u_{p_1} = 2000 ft/s
0
-0.02
-0.04
-0.06
-0.08
0
2.0
4.0
6.0
8.0
10.0
12.0
14.0
16.0
z (FT)
10^4 $\frac{R}{(\quad)}$

APPENDIX C

TWO-DIMENSIONAL WEDGE/OBLIQUE SHOCK

This appendix contains the following cases:

α (°)	r_p (um)	u_p (ft/s)	(r vs z)	(u_p vs z)	(T_p vs z)
30	5	100			
30	5	1000	x		
30	5	2000	x	x	x
30	50	100	x	x	
30	50	1000	x		
30	50	2000	x		

Note: These numerical calculations were carried out for the following conditions:

MW = Air (29)	P_∞ = 7876.8 psf
α_{p_i} = 0°	T_∞ = 540°R
θ_w = 30°	M_∞ = 5.0
T_{p_i} = 540°R	Titanium Dioxide

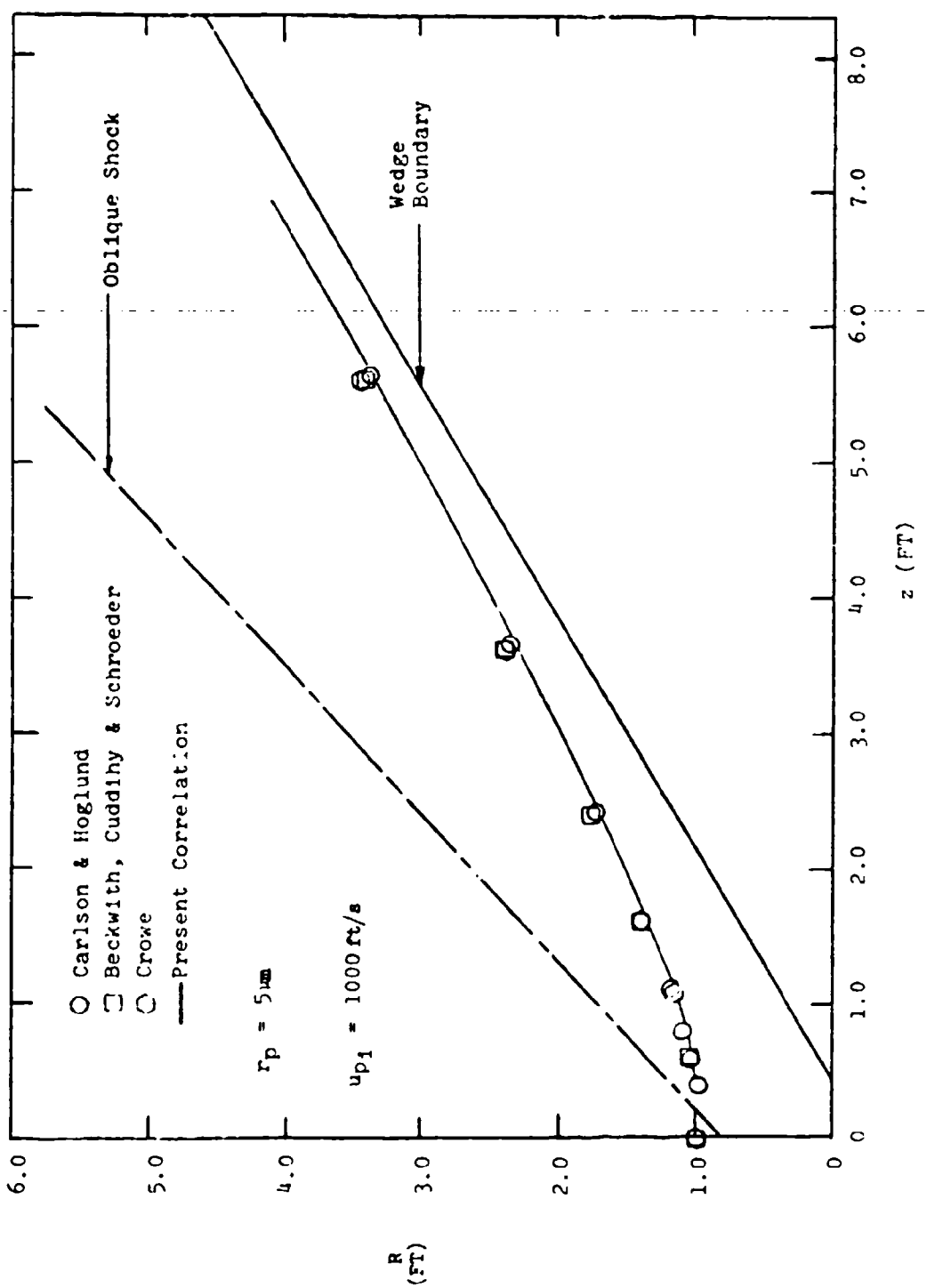
Oblique Shock
Wedge Boundary
Carlson & Hoglund
Beckwith, Cuddihy & Schroeder
Crowe
Present Correlation
r_p = 5μm
u_{p_1} = 1000 ft/s
R (FT)
z (FT)
6.0
5.0
4.0
3.0
2.0
1.0
0
1.0
2.0
3.0
4.0
5.0
6.0
7.0
8.0

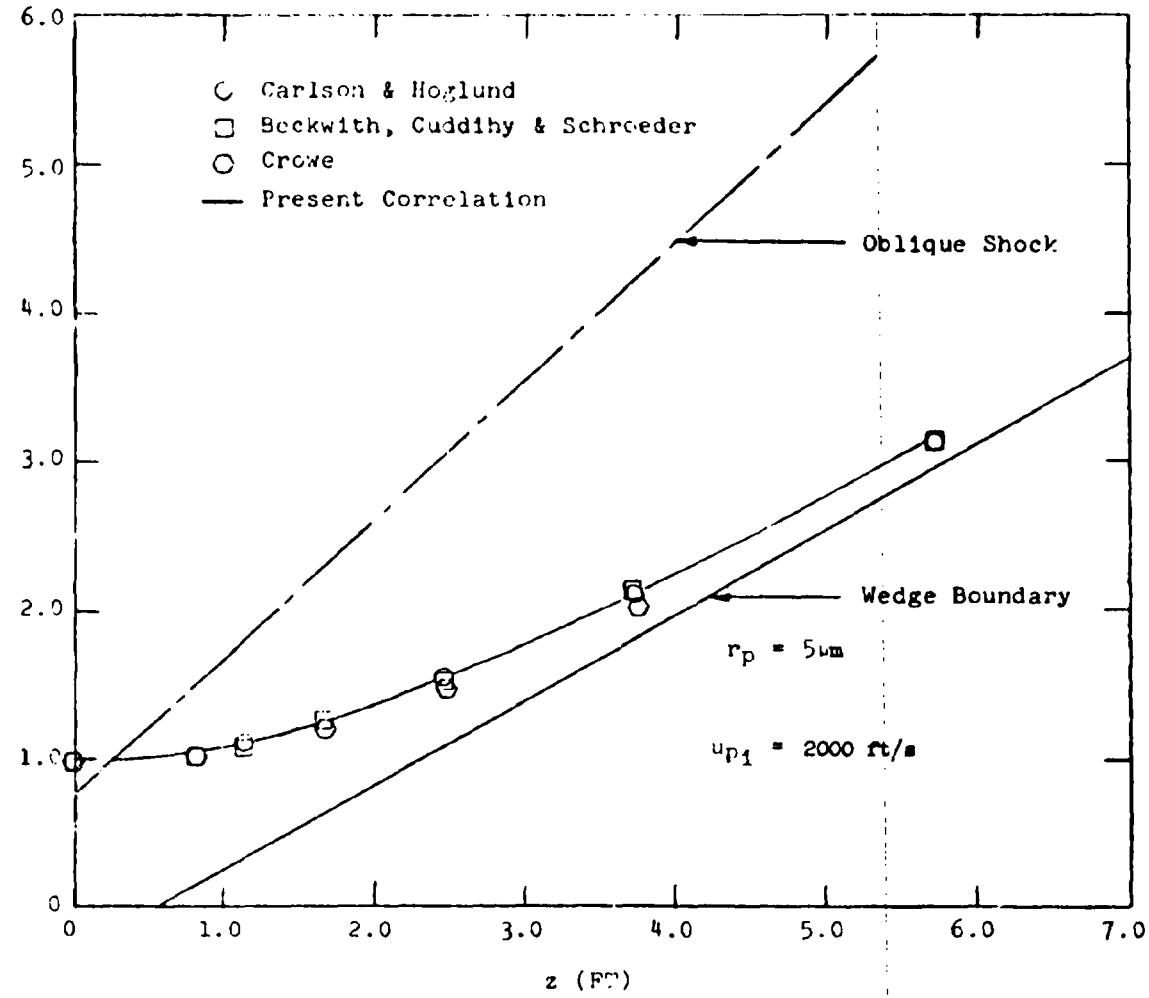
6.0
5.0
4.0
3.0
2.0
1.0
0
0
1.0
2.0
3.0
4.0
5.0
6.0
7.0
z (FT)
R (FT)
Carlson & Hoglund
Beckwith, Cuddihy & Schroeder
Crowe
Present Correlation
Oblique Shock
Wedge Boundary
r_p = 5μm
u_{p_1} = 2000 ft/s

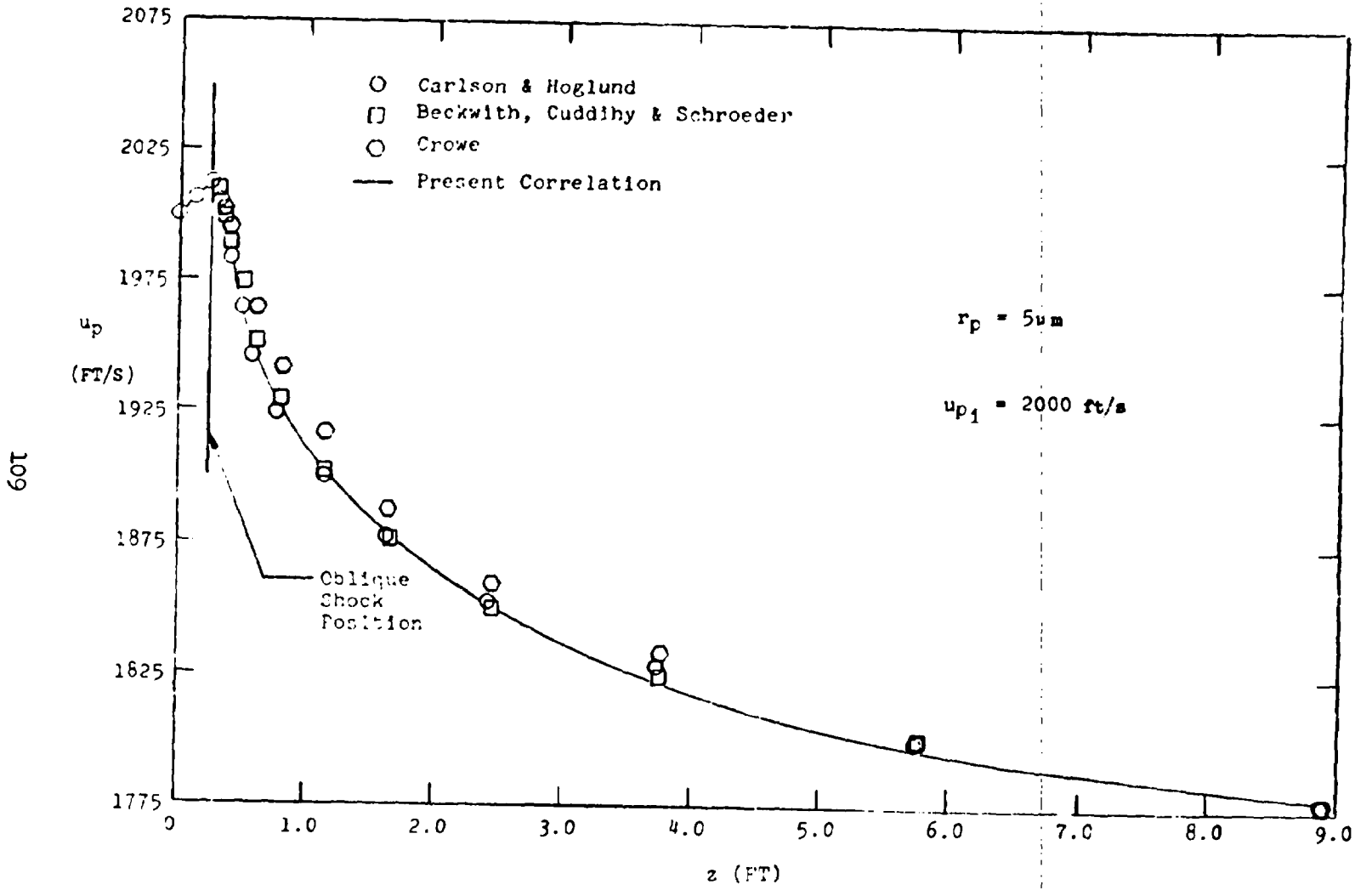
Carlson & Hoglund
Beckwith, Cuddihy & Schroeder
Crowe
Present Correlation
r_p = 5μm
u_{p_1} = 2000 ft/s
Oblique Shock Position
u_p (FT/S)
z (FT)
2075
2025
1975
1925
1875
1825
1775
0
1.0
2.0
3.0
4.0
5.0
6.0
7.0
8.0
9.0

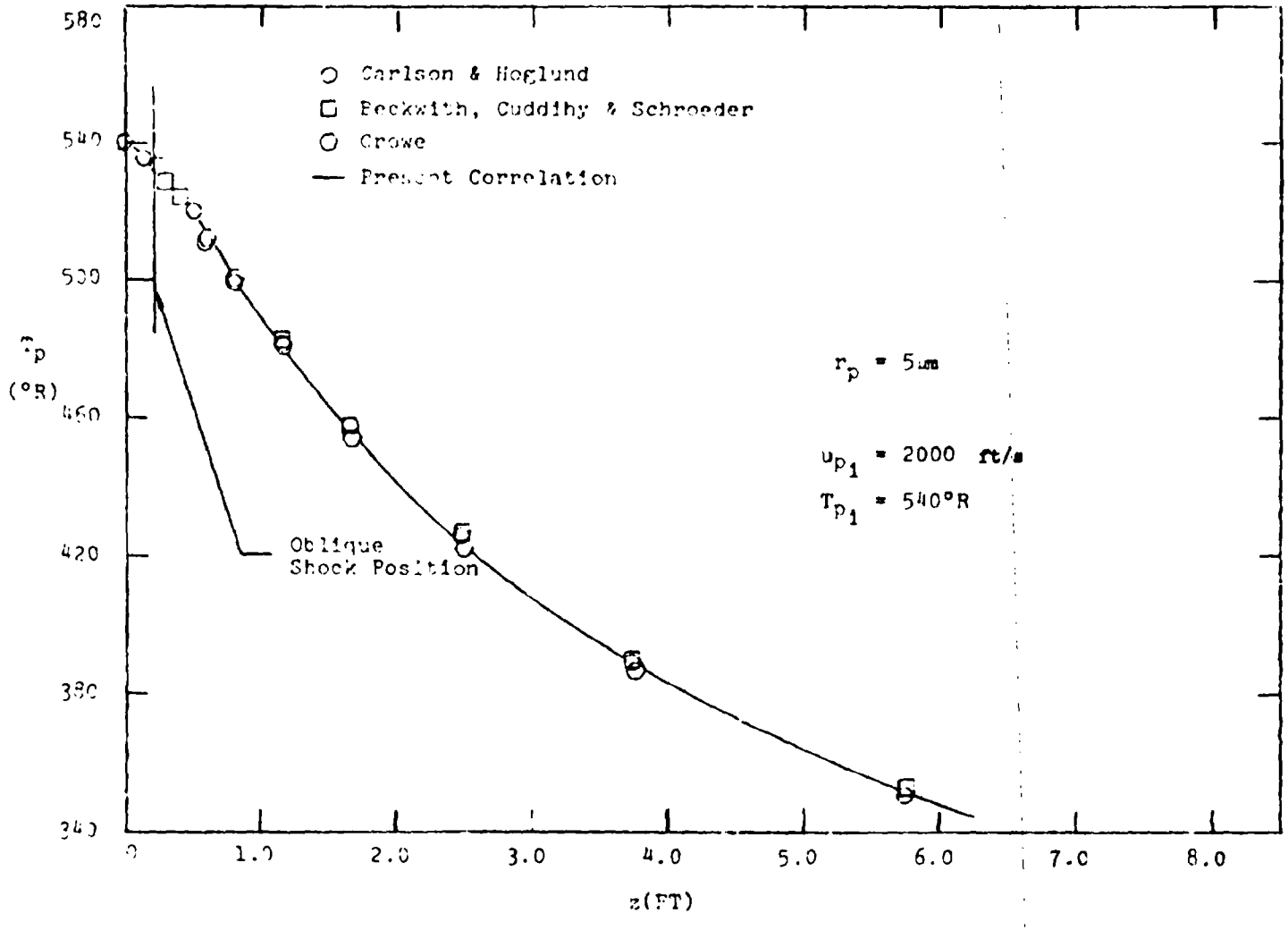
580
540
500
460
420
380
340
T_p
(°R)
Carlson & Hoglund
Beckwith, Cuddihy & Schroeder
Crowe
Present Correlation
r_p = 5μm
u_{p_1} = 2000 ft/s
T_{p_1} = 540°R
Oblique
Shock Position
0
1.0
2.0
3.0
4.0
5.0
6.0
7.0
8.0
z(FT)

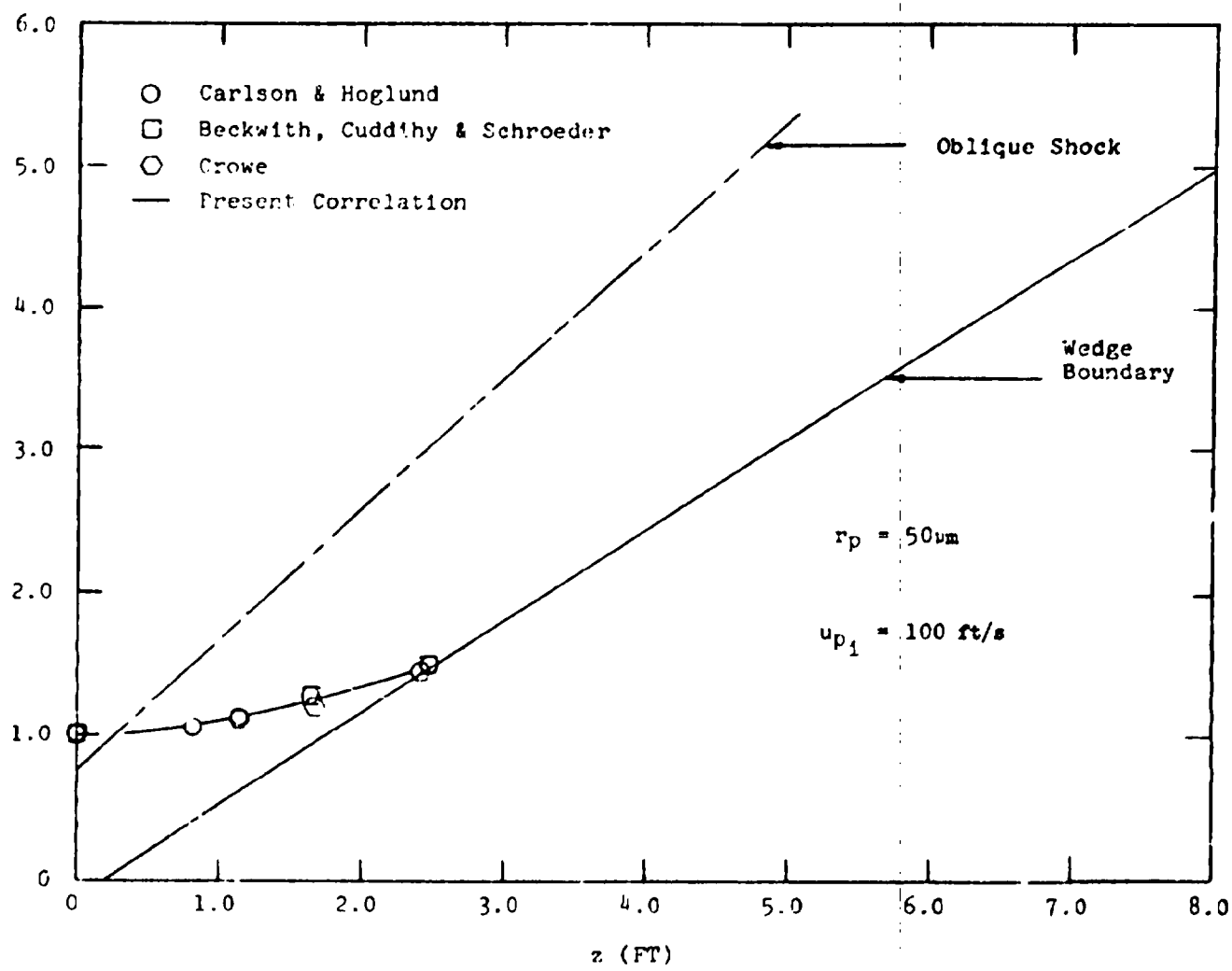
6.0
5.0
4.0
3.0
2.0
1.0
0
R (FT)
Carlson & Hoglund
Beckwith, Cuddihy & Schroeder
Crowe
Present Correlation
Oblique Shock
Wedge Boundary
r_p = 50μm
u_{p_i} = 100 ft/s
0
1.0
2.0
3.0
4.0
5.0
6.0
7.0
8.0
z (FT)

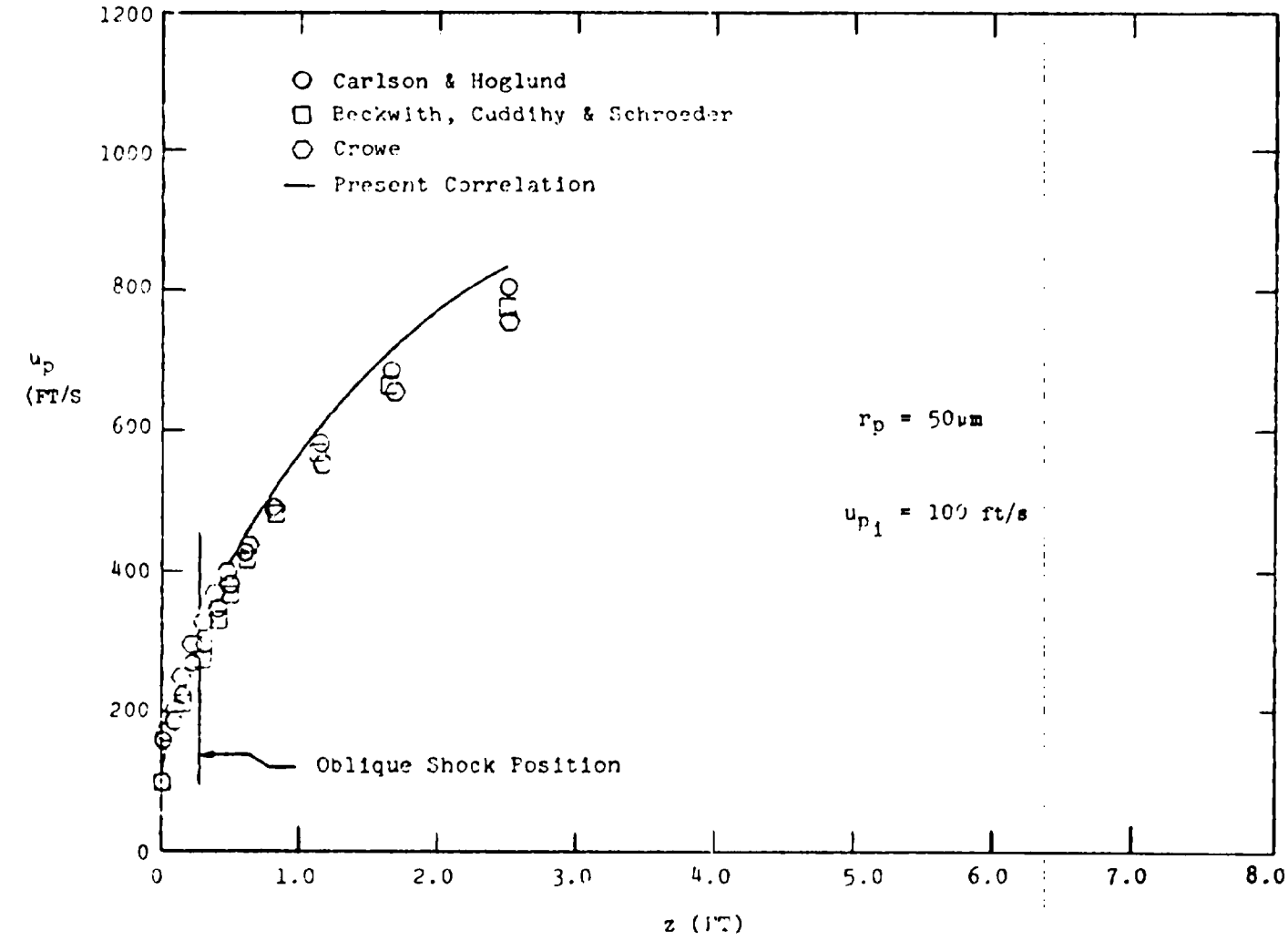
Carlson & Hoglund
Beckwith, Cuddihy & Schroeder
Crowe
Present Correlation
r_p = 50μm
u_{p_1} = 100 ft/s
Oblique Shock Position
u_p (FT/S
z (FT)
0
200
400
600
800
1000
1200
1.0
2.0
3.0
4.0
5.0
6.0
7.0
8.0

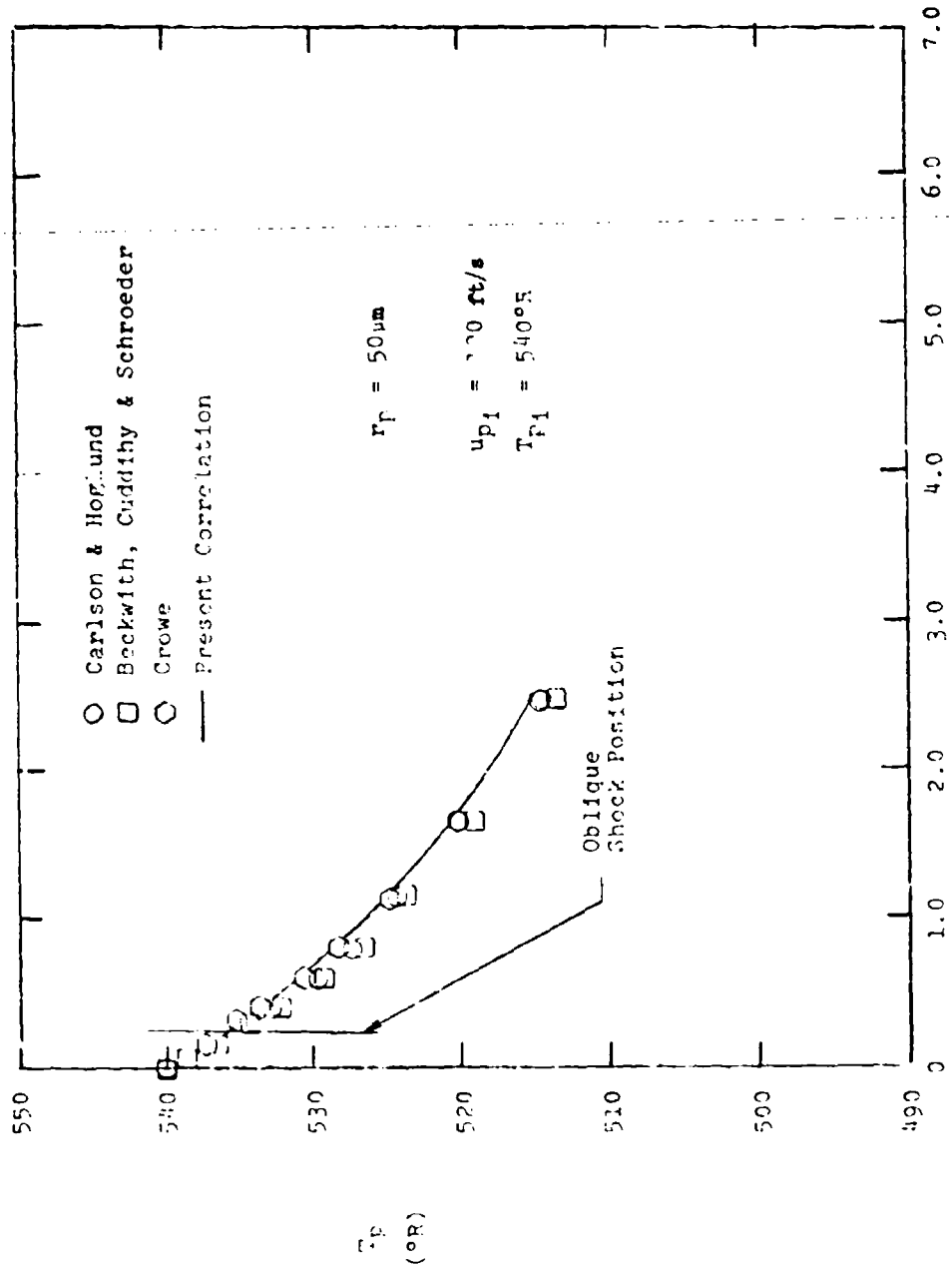
Carlson & Horsund
Beckwith, Cuddihy & Schroeder
Crowe
Present Correlation
r_f = 50μm
u_{p_1} = 700 ft/s
T_{p_1} = 540°R
Oblique Shock Position
T_p (°R)
z (FT)
550
540
530
520
510
500
490
0
1.0
2.0
3.0
4.0
5.0
6.0
7.0

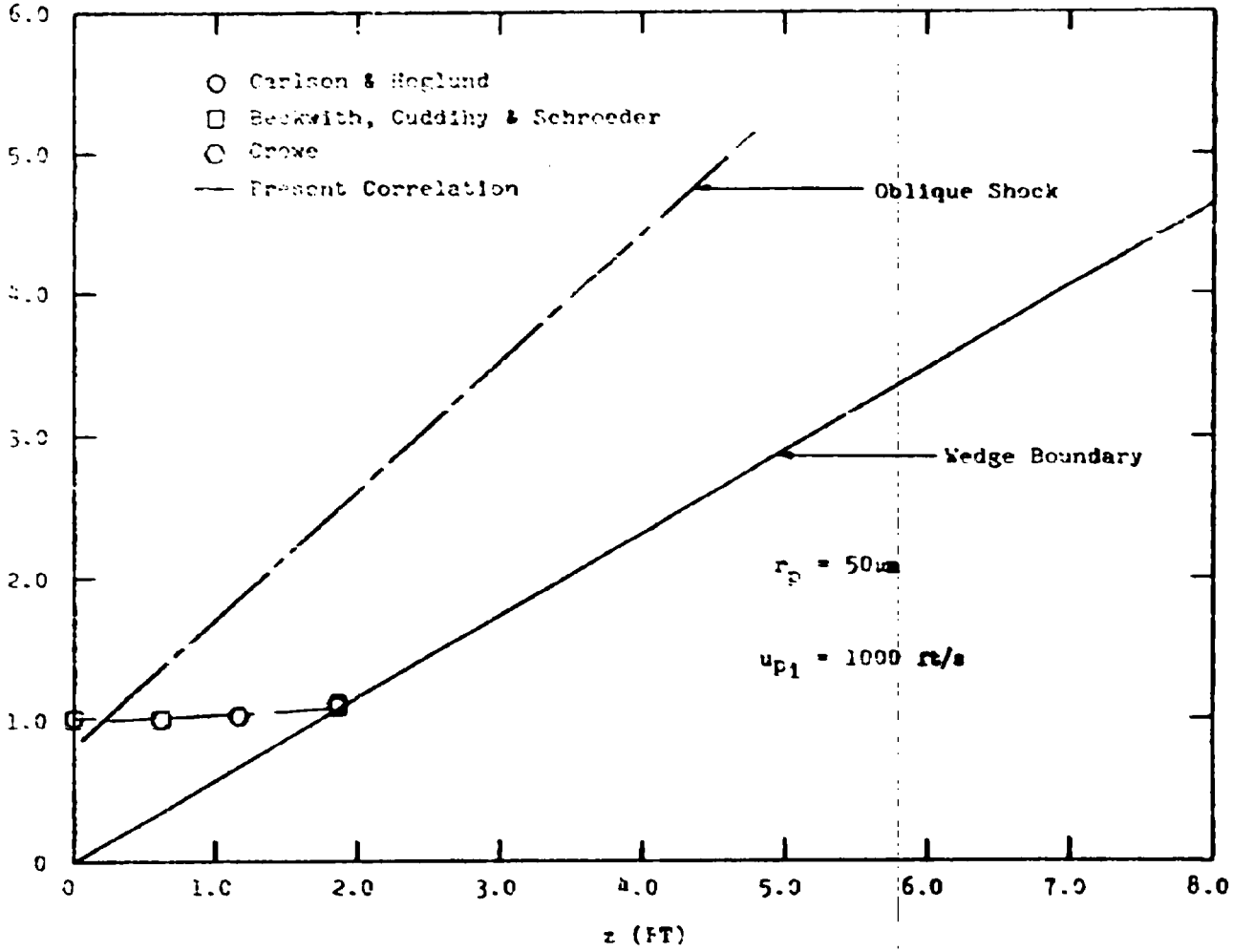
Carlson & Hoglund
Beckwith, Cuddihy & Schroeder
Crowe
Present Correlation
Oblique Shock
Wedge Boundary
r_p = 50μ
u_{p_1} = 1000 ft/s
R (FT)
z (FT)
0
1.0
2.0
3.0
4.0
5.0
6.0
7.0
8.0

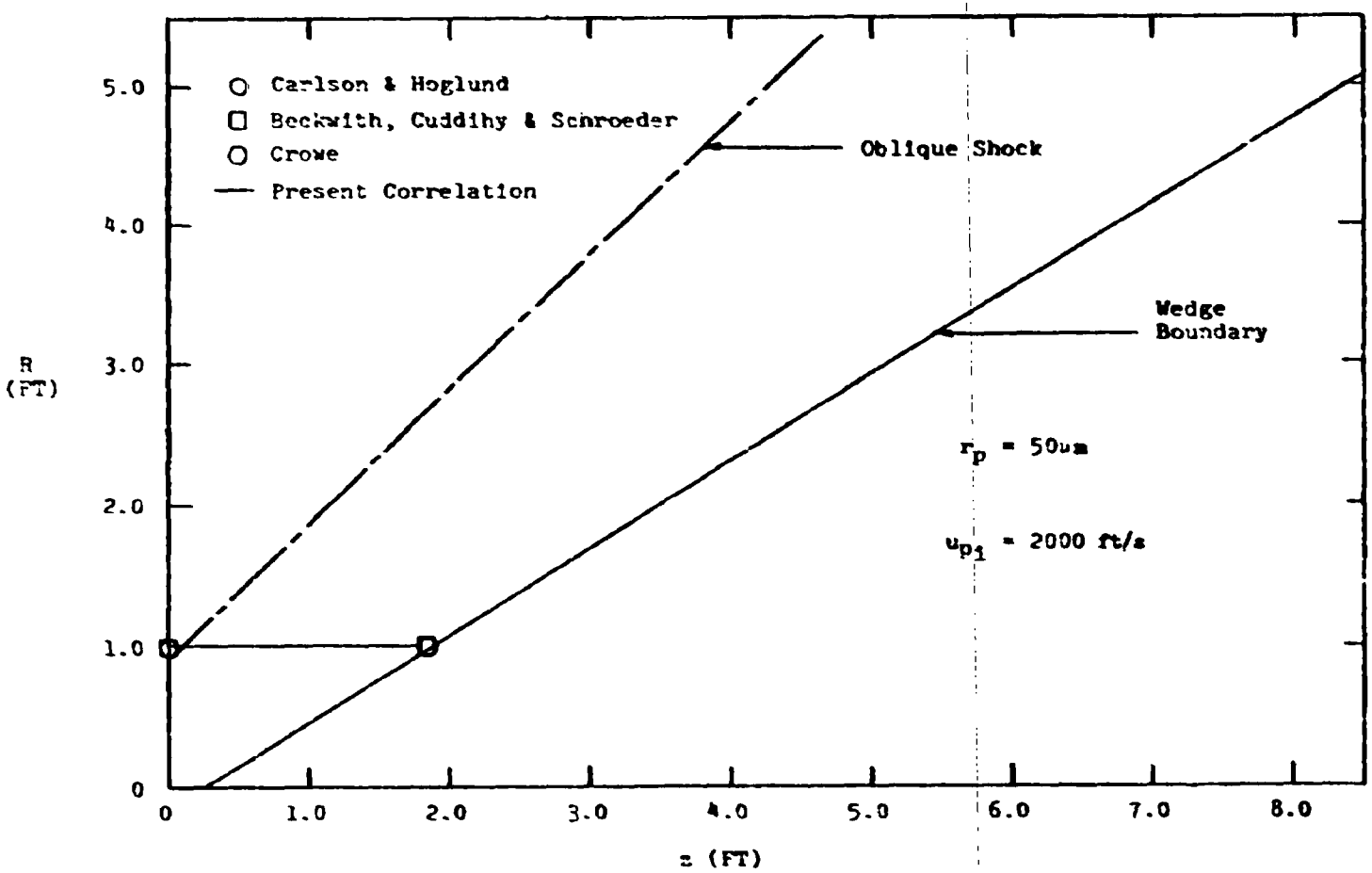
Carlson & Hoglund
Beckwith, Cuddihy & Schroeder
Crowe
Present Correlation
Oblique Shock
Wedge Boundary
r_p = 50um
u_{p_1} = 2000 ft/s
R (FT)
z (FT)
0
1.0
2.0
3.0
4.0
5.0
6.0
7.0
8.0

LIST OF SYMBOLS

A	Defined by Eqs. (16) and (17), area
C	Specific heat
C_D	Drag coefficient based on cross-sectional area
C_p	Specific heat at constant pressure
d	Diameter
N	Concentration
n	Defined by Eqs. (16) and (17)
q	Distance in the relative flow direction
Re_2	Reynolds number based on slip condition behind a normal shock, $Re_2 = \frac{\rho_{g2} \lvert u_{g2} - u_p \rvert d_p}{\mu_{g2}}$
r, R	Radius
T	Temperature
u	Velocity
z	Axial distance
α	Particle flow angle measured from the horizontal
β	Angle from the horizontal of the relative velocity vector
γ	Ratio of specific heats
ϵ	Particle emissivity
θ	Angle measured from the horizontal
μ	Viscosity
ρ	Density
σ	Stefan-Boltzmann constant

Subscripts

c	Continuum
FM	Free molecule
g	Gas
inc	Incompressible
p	Particle
rel	Relative between particle and gas
T	Total
w	Wall
2	After normal shock